Theses and Dissertations

8-9-2014

TUNABLE GRAPHENE CHEM-FET AND GRAPHENE/SI HETEROJUNCTION CHEMI-DIODE SENSORS

Amol Kumar Singh
University of South Carolina - Columbia

Follow this and additional works at: http://scholarcommons.sc.edu/etd

TUNABLE GRAPHENE CHEM-FET AND GRAPHENE/SI HETEROJUNCTION
CHEMI-DIODE SENSORS

by

Amol Kumar Singh

Bachelor of Technology
Indian Institute of Technology Kanpur, 2001

Master of Technology
Indian Institute of Technology Kanpur, 2005

Master of Science
University of Notre Dame, 2008

_____

Submitted in Partial Fulfillment of the Requirements

For the Degree of Doctor of Philosophy in

Electrical Engineering

College of Engineering and Computing

University of South Carolina

2014

Accepted by:

Goutam Koley, Major Professor

Tangali S. Sudarshan, Committee Member

MVS Chandrashekhar, Committee Member

Thomas Vogt, Committee Member

Lacy Ford, Vice Provost and Dean of Graduate Studies

Webb for using his processing facility and SEM and Prof. Williams for Raman spectroscopy.

I would also like to express my gratitude to my colleagues at NESL, who were always helpful to me throughout my graduate study and research and also for comraderies and jovial environment at NESL. Particularly, I thank Ahsan for helping me out with various measurements and processing. Together we solved many problems. I would also like to thank Ehtesham Quddus who helped me build my growth set-up. A big thanks also goes to staff at the department of Electrical Engineering specially Nat and Dave who were always ready to help me out in any situation with a smile.

Last but not the least, I would like to express my gratitude to my family members, who always contribute to my achievement. To my wife, Vandana, who loves me and supports me during our difficult time. To my father and mother, who have always been a source of encouragement and provided guidance to me throughout my life.

ABSTRACT

Graphene, a two-dimensional material with very high charge carrier concentration, has drawn large research interest for sensing chemical species based upon charge exchange. Atomically thin 2-dimensional arrangement of carbon in hexagonal fashion in graphene, where each carbon atom is attached to 3 neighboring carbon atoms, and presence of π^* and π bands imparts it many amazing properties. Some of these properties such as very high mobility, low 1/f and thermal noise, modulation of carrier concentration and Fermi level by electrical, optical, and chemical means, and very high surface to volume ratio make graphene very promising sensing material. In order to exploit these amazing properties for practical applications a reliable synthesis of high quality, large area graphene is needed. Chemical vapor deposition (CVD) based synthesis offers reliable, scalable, and inexpensive method to make low defect, uniform, large area, good quality, thinner graphene with the ability to transfer graphene on any desirable substrate. In this work, high quality single layer graphene has been synthesized by CVD for sensing applications. The growth process was optimized to yield good quality monolayer graphene, which uses CH_4 and H_2 as precursor gases for the growth at 1035 °C, as characterized by Raman spectroscopy.

Widely employed transduction mechanism in graphene chemical sensors or chemiresistor is conductance change due to charge exchange between graphene and

adsorbed molecules. The reported sensitivities have been fairly low and selectivity is difficult to observe without functionalization. This work aims at improving the sensitivity of graphene sensors by three different approaches. In the first approach, the use of a global back-gate in graphene chem-FET devices has shown improvement in sensitivity and imparts selectivity as well. These devices exploit the back-gate induced Fermi level movement of graphene relative to defect level of analytes such as electron accepting NO_2 and electron withdrawing NH_3 molecules. In the second approach, the defect density in graphene has been used to show sensitivity enhancement.

In these two approaches the sensitivity enhancement has the limitation of linear dependence of conductivity change to that of numbers of adsorbed molecules. In the third approach the use a graphene/Si heterostructure based Schottky device or chemi-diode, has been proposed for improving sensitivity many folds. Since graphene work function can be varied electrically or chemically, the Schottky barrier height (SBH) at graphene/Si interface also varies accordingly affecting the carrier transport across the Schottky barrier. These devices take advantage of graphene's atomically thin nature, which enables molecular adsorption on its surface to directly alter graphene/Si SBH, thus affecting the junction current exponentially when operated in reverse bias and resulting in very high sensitivity. The sensing mechanism based on SBH change has also been confirmed by capacitance-voltage measurements. By operating the devices in reverse bias, the work function of graphene, and hence SBH of the chemi-diode, can be controlled by the bias magnitude, leading to a wide tunability of the molecular detection sensitivity towards NO_2 and NH_3 with very low power consumption. Optimized sensor design to detect particular analyte is also possible by careful selection of graphene/Si SBH. The use of Pd and Pt

nano-particles on top of graphene as a functionalization layer serves to increase the capability of these chemi-diodes in sensing analytes such as H_2 which have very weak interaction with graphene. Therefore CVD graphene based sensors have been found to be very promising for practical applications in chemical sensing in ambient conditions which shows much improved sensitivity, and even selectivity towards hazardous gases.

TABLE OF CONTENTS

LIST OF TABLES

LIST OF FIGURES

CHAPTER 1

INTRODUCTION

Carbon is considered as the fundamental building blocks of all life forms on earth. It is chemically very versatile and forms larger variety of compounds. Each atoms of carbon can bond with 4 different atoms or molecules. When the carbon atoms link amongst themselves in tetrahedral fashion utilizing sp^3 bonding, they form diamond the hardest naturally occurring material with insulating properties, however when they bond with 3 carbon atoms only, in a honeycomb fashion, graphite is formed. It is three dimensional
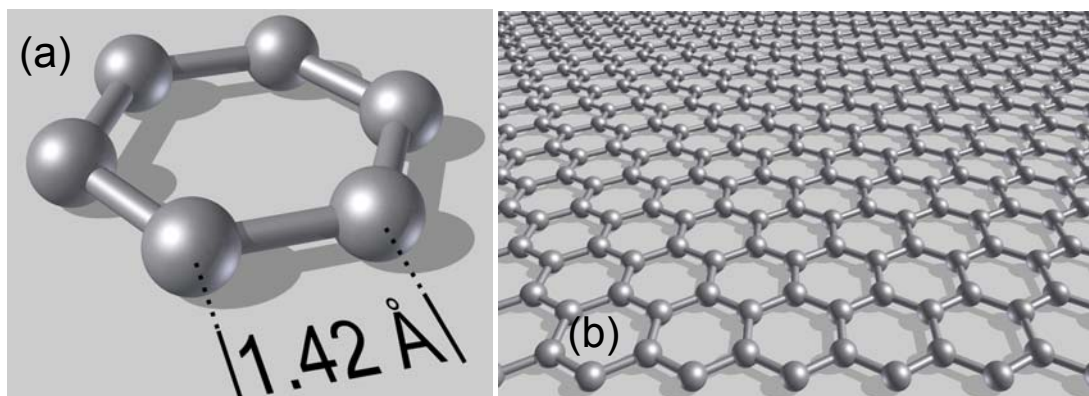
Figure 1.1 (a) Schematic representation of single planner hexagon consisting of 6 C atoms connected to each other by sp^2 bonding with C-C bond length of 1.42 Å. (b) Periodic repetition of hexagonal unit resulting in 2-dimensional honeycomb structure of graphene.

allotrope of carbon with sp^2 hybridization of carbon to carbon bond. Graphite is rich in electrons and conducts along its layers. Graphite became well known after the invention of pencil in 1564. Around that time the mining and production of high purity and soft graphite

from Cumbria, England was strictly controlled due to its strategic application as refractory lining of canon ball molds. The ability of graphite to write comes from the fact that it made up of individual sheets of carbon which held together by weak Vander wall forces which
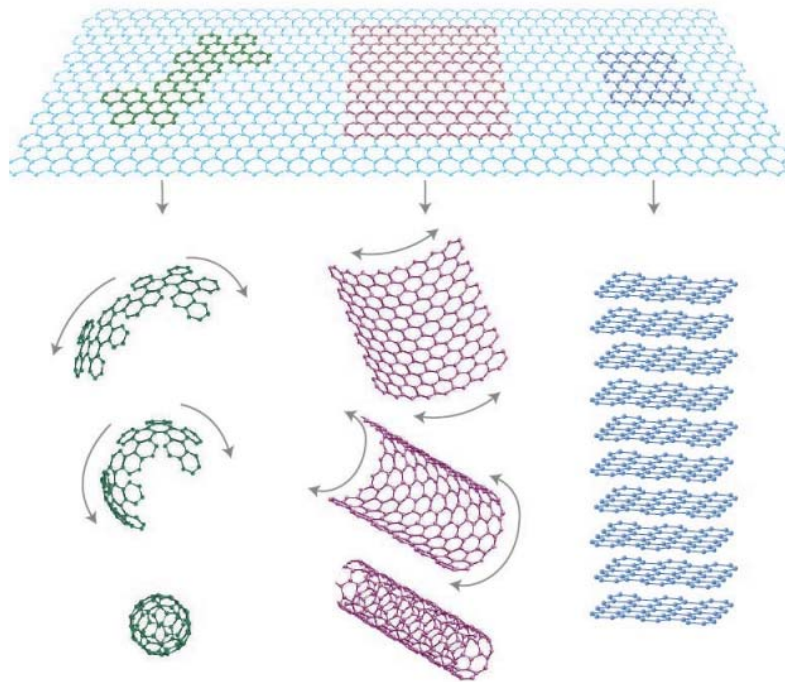
Figure 1.2 Graphene as a building block of various forms of sp^2 carbon materials such as fullerene, carbon nanotube, and graphite [2].

allows layers to slip under shear force and leave a trace of thinner graphite on the surface. This very ability of slipping also make them very good lubricants. Since these sheets could slide upon each other they could be separated as very thin graphitic sheet down to single layer as demonstrated on SiO_2 by and Novoselov and Geim in 2004.[1]

These individual sheets of carbon, which are constituent of graphite, are made up of planner sp^2 bonded carbon atoms arranged in honeycomb fashion consisting of hexagon of carbon, as in benzene. This hexagon is depicted in Figure 1.1(a) with C-C bond length of 1.42 Å. The individual sheet structure as shown in Figure 1.1(b) is referred as graphene.

Graphene as a true two-dimensional (2D) crystal not only possess many amazing properties not seen before in bulk material but also is the basic building blocks of many forms of sp^2 bonded carbon. Figure 1.2 captures this description vividly.[2] It can be wrapped into fullerenes molecules where carbon atoms are arranged in spherical fashion by introduction of pentagons as positive curvature defects. These fullerenes have discrete energy states and can be considered as zero dimensional (0D)[3] graphitic structures. Graphene can be rolled along a given direction and the carbon bonds can be reconnected to generate 1-dimensional (1D) nanostructures called as carbon nanotubes (CNTs)[4] consisting of only hexagons of carbon atoms. The three-dimensional (3D) structure, graphite, formed by stacking graphene sheet attached by week van der Wall forces has already been discussed above.

1.1 Electronic Structure of Graphene

The physical and chemical properties of materials is determined by their crystal structure and electronic structure. Many unique properties of graphene are tightly linked to its 2D crystalline nature and the resulting band structure. In 2D crystalline hexagonal lattice of graphene each carbon atom is C-C bond length (a = 1.42Å) apart from its 3 nearest neighbors in a plane and shares a sp^2 hybridized σ bond with them. The forth orbital, p_z consisting of single electron, is in z direction which is perpendicular to the graphene plane, and is responsible for conductivity in graphene. These p_z electrons from each carbon atom hybridize to form π and π* bands which give rise to many peculiar electronic properties of graphene.[5, 6].

3

The unit cell and corresponding reciprocal lattice of graphene is shown in Figure 1.3[5]. The unit cell consists of two interpenetrating triangular lattice shown by A and B
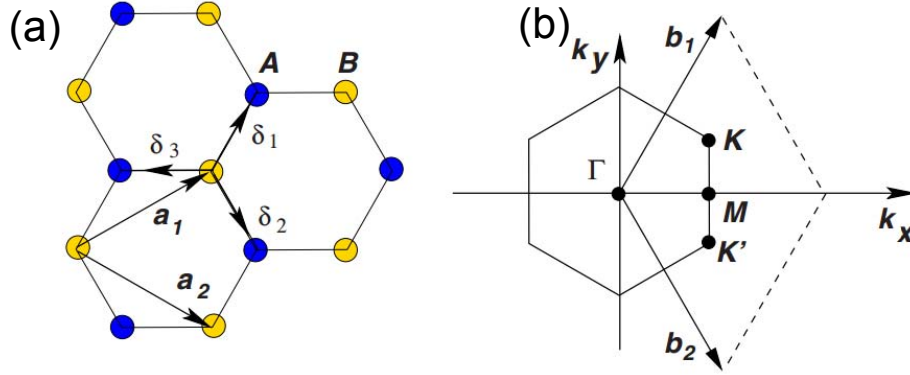
Figure 1.3 Hexagonal lattice of graphene and Brillouin zone. (a) The 2D lattice of graphene consisting of two triangular lattices (shown as A & B) interpenetrating each other. **a1** and **a2** are unit lattice vectors. (b) The Brillouin zone of graphene showing K & K' as location of Dirac cones [5].

type atoms. The basis of unit cell consists of two atoms. The lattice vectors, and reciprocal lattice vectors are given by Equation 1.1 and 1.2.

$$\boldsymbol{a_1} = \frac{a}{2}\left(3, \sqrt{3}\right), \ \ \boldsymbol{a_2} = \frac{a}{2}\left(3, -\sqrt{3}\right) \qquad (1.1)$$

$$\boldsymbol{b_1} = \frac{2\pi}{3a}\left(1, \sqrt{3}\right), \ \ \boldsymbol{b_2} = \frac{2\pi}{3a}\left(1, -\sqrt{3}\right) \qquad (1.2)$$

From this lattice structure the energy band structure of graphene can be determine by invoking tight binding model or linear combination of atomic orbitals (LCAO) following the original work of Wallace in 1947.[7]

In order to obtain dispersion relationship or band structure we need to consider the interaction of carbon atoms to nearest and next nearest neighboring carbon atoms. As seen

from Figure 1.3(a) each carbon atom has 3 nearest and 6 next nearest neighbors. The hopping of p_z electron is possible to nearest site (from A to B) or next nearest site (A to A). The interaction energy involved is given by $t \sim 2.9$ eV for A to B hopping and $t' \sim 0.1$ eV for A to A atoms hopping. Solving the Hamiltonian with assumption of only nearest neighbor interaction being important, the dispersion relation is given by the following expression.

$$E(\boldsymbol{k}) = \pm t \sqrt{3 + 2\cos(\sqrt{3}k_y a) + 4\cos\left(\frac{\sqrt{3}}{2}k_y a\right)\cos\left(\frac{3}{2}k_x a\right)} \qquad (1.3)$$

where $\boldsymbol{k}$ is reciprocal lattice vector. The positive term in Equation 1.3 corresponds to conduction band and negative is for valence bans as plotted in Figure 1.4(a)[5] appears linear near low energy points in reciprocal lattice space called as Dirac point. The conduction band and valence band touch each other at these Dirac point at 6 places[8] on the corner of a graphene's Brillouin zone (Figure 1.4(b)) referred as K and K' points with the following position vectors in the reciprocal space.

$$\boldsymbol{K} = \left(\frac{2\pi}{3a}, \frac{2\pi}{3\sqrt{3}a}\right); \boldsymbol{K'} = \left(\frac{2\pi}{3a}, -\frac{2\pi}{3\sqrt{3}a}\right) \quad (1.4)$$

The dispersion relation at K and K' points and within ± 1 eV vicinity of the Dirac point is given by the following linear relationship.

$$E(\boldsymbol{k}) = \pm \hbar v_F |\boldsymbol{k}| = \pm v_F \sqrt{k_x^2 + k_y^2} \quad (1.5)$$

where v_F is Fermi velocity given by

$$v_F = \frac{3at}{2\hbar} \approx 0.9 \times 10^6 \ m/s \qquad (1.6)$$

This linear dispersion relationship at low energy makes charge particles (electrons and holes) move with v_F, as described by Equation 1.6, which is close to relativistic velocity. Therefore electrons and holes close to Dirac point in graphene is called as Dirac fermions.
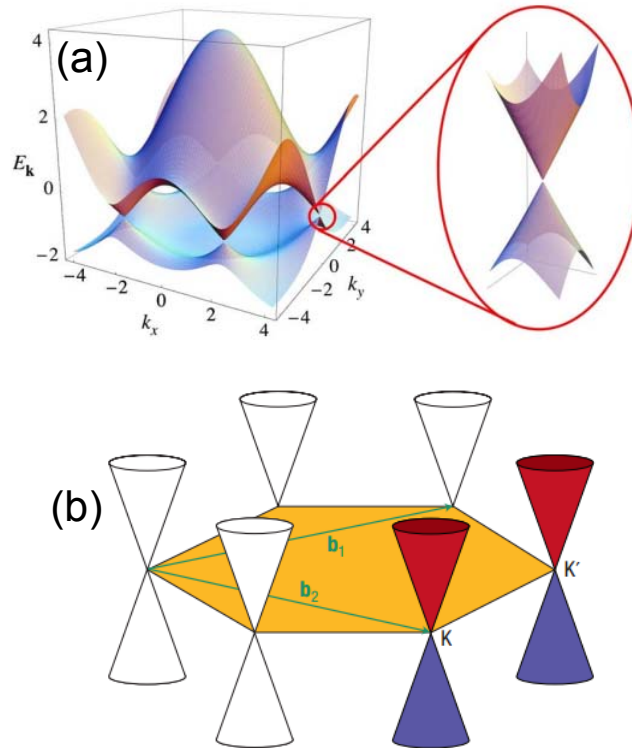
Figure 1.4 (a) Energy bands in monolayer graphene in the units of t = 2.7 eV (the nearest neighbor hopping energy). The upper band is conduction band and lower one is valence band. The blown up diagram shows linear relationship close to Dirac point where conduction band and valance band meet. (b) Low-energy electronic structure of graphene showing 6 Dirac points such points of contact. Two distinct corners of Brillouin zone are shown as K and K' [5,8].

This is in stark contrast with most of the bulk semiconductors which exhibit parabolic dispersion relationship at low energies.

The linear dispersion relationship of graphene is also responsible for properties like vanishing density of states (DOS) at Dirac points. The DOS in graphene is given by[9, 10]

$$DOS = \frac{E}{2\pi\hbar^2 v_F^2} \quad (1.7)$$

The zero band gap state of graphene at Dirac point is called intrinsic state. Therefore the intrinsic graphene refers to a state at which graphene has no charge carriers.

1.2   Electronic Transport and Field Effect Behavior of Graphene

1.2.1   Ambipolar Field Effect in Graphene

Electric field applied perpendicular to graphene plane can induce charge carriers, electrons or holes, also referred as electric field effect. The Fermi level (E_F) can move up in conduction band inducing electrons, and can move down in valance band inducing holes depending upon the direction of the field. This results in ambipolar nature of graphene channel. In absence of externally applied electric field the E_F and DOE should ideally be zero in graphene according to Equation 1.7. However in graphene channel there is always finite charge present due to either thermal generation or induction due to impurities at graphene and substrate interface even in absence of applied electric field. For this reason the threshold voltage beyond which graphene based field effect transistor can turn on or off does not really exist. The minimum to maximum current ratio in graphene based FETs remains in the range to 5-10 and hence render them unsuitable for switching application despite of their high mobility values.

1.2.2   Mobility

The main scattering mechanism in graphene are phonon scattering[11], Coulomb scattering[12], and short range scattering[13] primarily due to defects such vacancies and cracks in graphene. Due to operation of these scattering mechanism in graphene the mobility is strongly dependent upon the quality of graphene and underlying substrates. For

instance at room temperature surface polar phonons and defects are two major scattering mechanism for graphene on SiO_2, whereas at lower temperature phonons become important. The typical mobility values[14] of good quality graphene on SiO_2 ranges from 10000 to 15000 $cm^2V^{-1}s^{-1}$. These mobility numbers are much higher in those reported in convention semiconductors and ever higher than 2D electron gas systems. Removing the substrates or using the one free from trapped charges has been shown to improve the mobility. The reported mobility in suspended graphene has been as high as 200,000 $cm^2V^{-1}s^{-1}$ for charge density below 5×10^9 cm^{-2} at a low temperature of 5K.[15, 16] At room temperature the supported graphene for instance on SiO_2 will have an upper limit of 40000 $cm^2V^{-1}s^{-1}$ on mobility due to scattering by optical phonon of the substrate rather than phonon in the graphene channel.

1.2.3   *Minimum Conductivity*

Due to presence of disorder in graphene in the form of defects, impurities, ripples etc. produces fluctuations in the graphene's electrostatic potential. These fluctuations become significant at the Dirac point where their screening is weak due to low charge density. The fluctuations in charge density has been proposed to be electron-hole puddles which have also been observed in scanning probe methods on graphene/SiO_2 samples.[17] This behavior has been attributed to the experimental observation of minimum conductivity of graphene in the range of $4e^2/h$ even though DOS approaches to zero at Dirac point. The other claim for the observation of minimum conductivity is the presence of impurities concentration in SiO_2.[18]

1.3 Optical Properties

Impressive optical properties of graphene such as high transparency, low reflectance coupled with high carrier mobility and near ballistic transport makes graphene very attractive for transparent electrode application. Monolayer graphene has very high optical absorption considering its atomic layer thickness. The absorbance value of monolayer graphene is about 2.3% for visible light. In multilayer graphene the individual layers do not interact each other optically due to their behavior as 2-dimensional electron gas (2DEG). Therefore the absorbance of multilayer graphene is roughly proportional to number of layers.[19] The absorbance of graphene remains fairly constant in the range of 2-3% from ultraviolet to infrared region of electromagnetic spectrum when compared to other transparent materials.[20] Graphene's reflectance remains very low at 0.1% but it increases to 2% for 10 layers.

1.4 Mechanical Properties

Graphene also has excellent mechanical properties and is a leading contender for nanoelectromechanical systems (NEMS). It is reported to be one of the strongest materials ever tested. Measurements have shown that graphene has a breaking strength 200 times greater than steel, with a tensile modulus (stiffness) of 1 TPa (150,000,000 psi).[21] Using an atomic force microscope (AFM), the spring constant of suspended graphene sheets has been measured. Graphene sheets, held together by van der Waals forces, were suspended over SiO_2 trenches where an AFM tip was used to test its mechanical properties. Its spring constant was in the range 1–5 N/m and the Young's modulus was 0.5 TPa, which differs from that of the bulk graphite. These high values make graphene very strong and rigid.

These intrinsic mechanical properties could lead to usage of graphene for NEMS applications such as pressure sensors and resonators.[16]

1.5 Chemical Sensing Abilities of Graphene

The 2D nature of graphene coupled with delocalized π electrons resulting from sp^2 hybridization in C-C bond makes it highly suitable for sensing applications. The 2D nature makes it essentially a surface (as seen in Figure 1.1), enabling analyte molecules to adsorb very efficiently and produce the maximum change in its physical properties. On the other hand, the presence of delocalized π electrons makes it sensitive to a large variety of analytes that can adsorb on its surface and exchange charge with it or modify its surface properties. The noise characteristics of graphene have also been very impressive in the range of 10^{-9} to 10^{-7} Hz^{-1} when compared with carbon nano tubes.[22] In general graphene shows very low 1/f and thermal noise.[23] These exceptional material properties have led to the demonstration of graphene based sensors that are capable of detecting down to a single analyte molecule.[24]

1.6 Applications and Trends

The combination of various amazing properties of the graphene enables its application in not just gas sensing but in variety of diverse areas such as terahertz devices, high speed transistors, displays, batteries, ultracapacitors, hydrogen storage, solar cells, membrane for separation of gases, magnetic, charge, strain, and biological sensors, composites etc. to name a few. This list has been ever expanding as new applications come to light by choosing, mixing and matching the properties of graphene alone or with combination with other materials. Figure 1.5(a) shows major applications[25] of graphene which have already

been demonstrated utilizing different properties of graphene. Figure 1.5(b) shows a π chart for applications that graphene companies were targeting in 2011.[26] This chart was
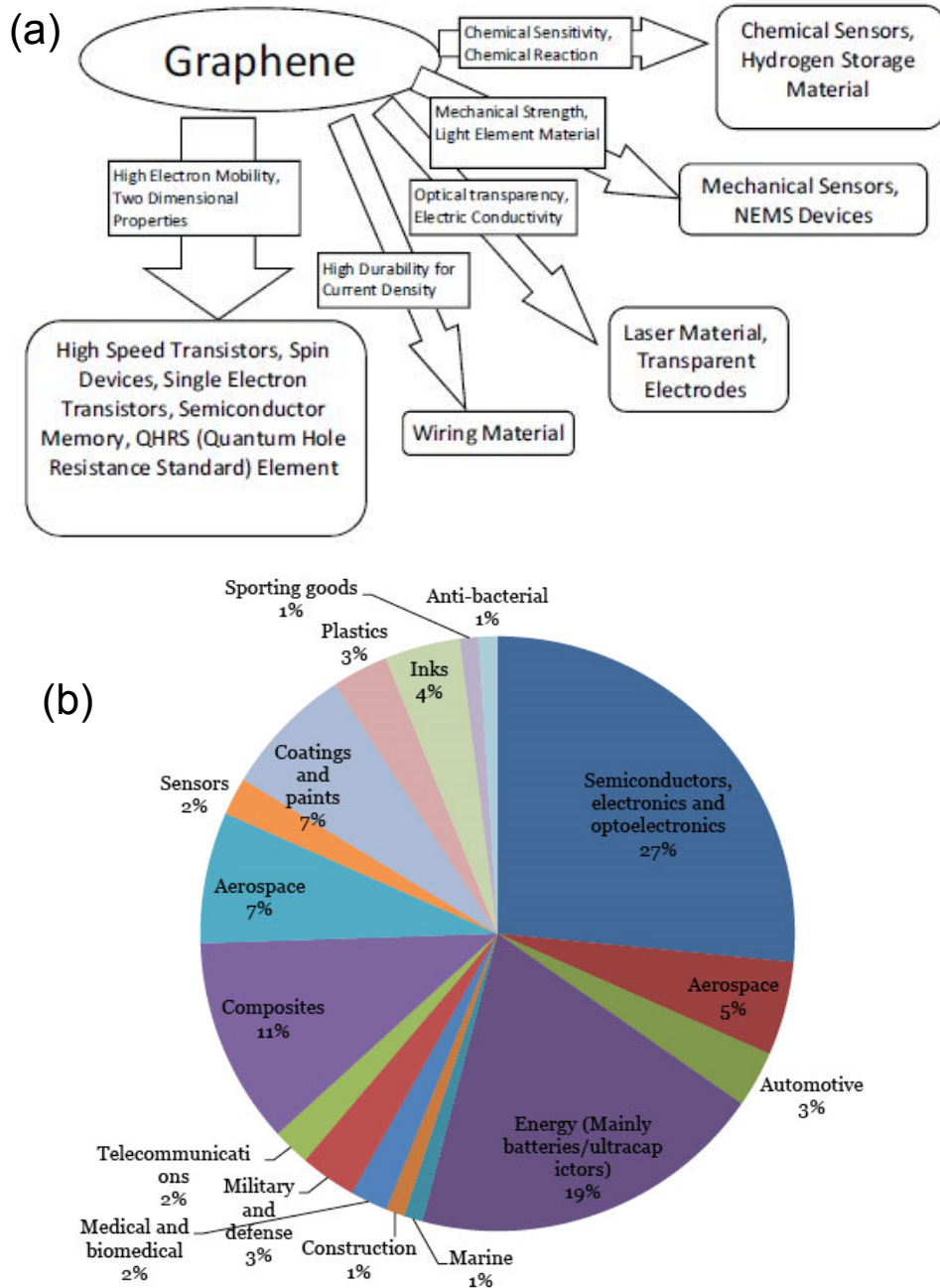
Figure 1.5 (a) Various applications of graphene using different properties of graphene [25]. (b) Future trend of application of graphene by industry as surveyed in year 2011 [26].

prepared after a comprehensive survey of graphene companies and clearly highlights the versatility of graphene.

1.7   Outline of the Dissertation

Despite of being highly promising material for various kind of application such as those shown in Figure 1.5(a) graphene still remains a newer material. It will complete 10 years of its first isolation in 2014. It therefore offers many challenges to be solved like any other new material system such as nitride semiconductors before it could become a commercial success.

One of the major challenge graphene faces is its manufacturability. Growing device quality, large area graphene still remains a challenge for mass production. Two approaches appears promising, namely epitaxial and chemical vapor deposition bases graphene growth. The later growth technique constitute the scope of this thesis and is discussed in chapter 2, which also focuses on Raman spectroscopy as the principle characterization technique of graphene to determine its quality and type and even to determine of the grown material is graphene or not.

The other major challenge graphene offers is careful control of its properties since it is one atom thick therefore its properties are highly affected by its environment and surroundings. Therefore there is a need to understand and develop better fabrication technique which has been explore in chapter 3. Graphene suffers from lack of selectivity in detecting molecules. The lack of bandgap in graphene also results in low turn-off ratio in graphene transistors, which makes it unattractive for use in integrated circuits. However the absence of band gap helps in changing the properties of graphene by use of a global back-gate. Figure 1.6 illustrates this effect for a pristine graphene (obtained by exfoliation)
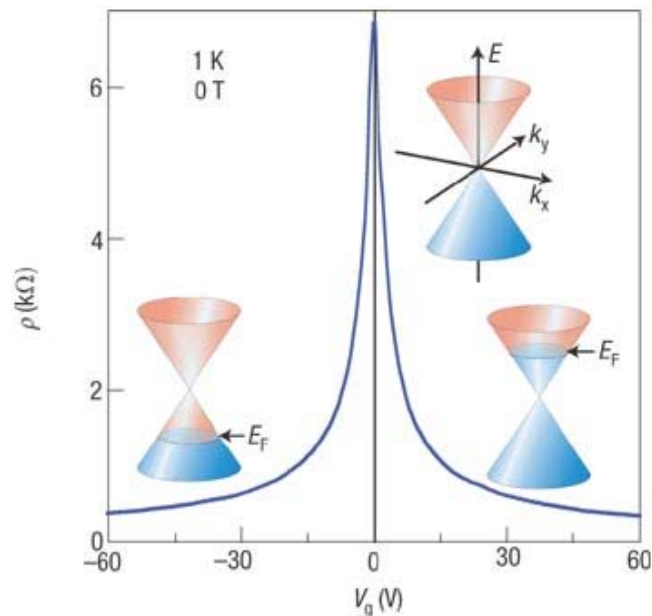
Figure 1.6 Ambipolar response of a single-layer pristine graphene [2]. The Fermi level E_F is located at Dirac point for $V_g = 0V$. At negative V_g the E_F is below Dirac point and for positive V_g, E_F goes above it.

field effect transistor (FET).[2] The Dirac point is the point of maximum resistance at certain gate bias V_g. For pristine graphene Dirac point is observed at $V_g = 0V$ (Figure 1.6). Due to absence of band gap a graphene FET always remains on and the channel carrier type can be changed from n-type to p-type when V_g is changed from positive to negative values and vice-versa. This opens a window of opportunity to impart selectivity and sensitivity to polar molecules which has also been explore in chapter 3.

A good quality low defect graphene based sensing elements typically show a poor response or sensitivity towards chemical analyte and pose as another area of challenge for graphene based chemical sensors to improve the sensitivity numbers. This forms the discussion of chapter 4 where use of a defective graphene shows improvement in sensitivity. However sensitivity has been proposed to improve dramatically by use a graphene based Schottky diode. Preliminary results supports our hypothesis. The extensive

sensing under various test condition such as under optical illumination, dark, different exposure duration, concentration of analytes such as NO_2 and NH_3 going down to ppb level will be proposed as the ongoing activities towards completion of thesis. It will also be proposed to use the functionalization layer such as Pd and Pt layers to extend the sensitivity towards non polar gases such as H_2.

Finally in chapter 5, the contributions to the scientific community and important accomplishments and major findings of the project will be summarized. It will also capture some of the work in progress and possible future directions.

CHAPTER 2

GRAPHENE GROWTH

There are various routes to grow or procure graphene. Each technique comes with their own sets of challenges. Broadly there are four well-recognized methods. These methods include micromechanical cleavage, epitaxial growth, growth by CVD and reducing graphene oxide. Epitaxial and CVD growth methods have evolved to generate large area, good quality graphene. The reduced graphene oxide (RGO) is also capable of large area graphene however the structural quality of graphene remains poor. These growth techniques are surveyed briefly to put CVD based growth in perspective.

2.1 Micromechanical Cleavage and Ultrasonication

In the very beginning, Graphene sheets were obtained by mechanical cleavage or exfoliation of graphite, which consists of loosely bonded parallel layers of graphene.[27] The technique often referred to as a "scotch-tape method," can provide 2D graphene crystals of high structural and electronic quality up to mm size. Though delicate and time-consuming, this is the only technique that can guarantee production of defect free graphene without any contamination. Thus, it is very well suited for basic research and for making proof-of-concept devices, which only requires a small size of graphene with typical dimensions on the order of mm or less. Figure 2.1 shows a representative optical image of monolayer and bilayer exfoliated graphene on 300 nm thick SiO_2 substrate.[28] Instead of exfoliating graphite (typically highly oriented pyrolytic graphite) manually, it is also
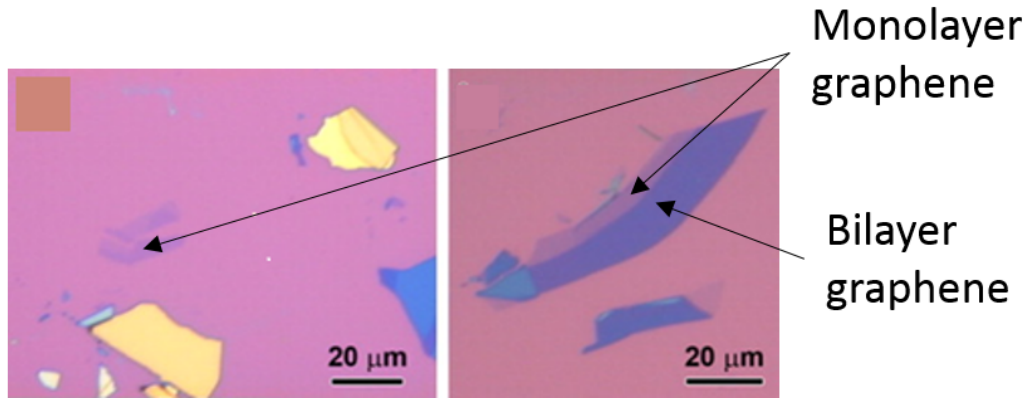
Figure 2.1 The small size (10s of μm) chunks of graphene obtained by exfoliation method showing poor contrast for monolayer graphene and better contrast for bilayer graphene [28].

possible to automate the process by using, for example, ultrasonic cleavage.[29] This leads to stable suspensions of submicron graphene crystallites, which can then be used to make polycrystalline films and composite materials.[29, 30] Conceptually similar is the ultrasonic cleavage of chemically "loosened" graphite, in which atomic planes are partially detached first by intercalation, making the ultrasonication method more efficient.[30] The ultrasonication method allows production of larger area graphene, although controllability of the process and the structural integrity of graphene are still challenges that need to be addressed.

2.2   Epitaxial Growth of Graphene

This technique is well established for producing large area graphene of high quality by thermal annealing of SiC wafers.[31-33] In this method, which takes advantage of well-established SiC epitaxy, 6-H or 4-H polytype of SiC is heated in the temperature range of $1200 - 1600$ °C in ultra-high vacuum (UHV) of 1×10^{-10} Torr for several minutes. At this high temperature Si leaves the SiC surface owing to its higher vapor pressure than carbon. The remaining C rich surface then rearranges on the hexagonal lattice of SiC to generate
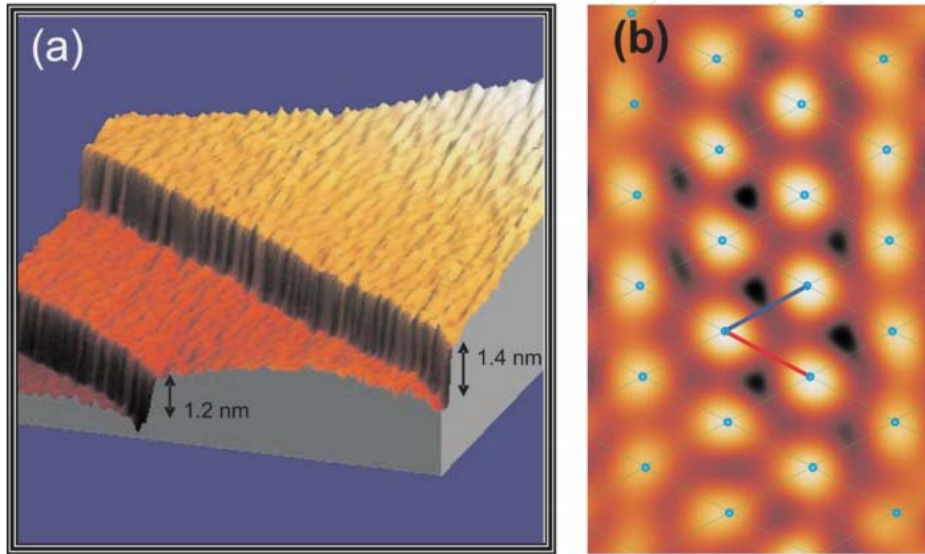
Figure 2.2 (a) STM image of the graphene film formed on a carbon-face semi-insulating SiC substrate showing 1.2 and 1.4 nm steps in the basal plane of the SiC substrate. (b) Atomic resolution STM image of graphene showing triangular sublattice of carbon atoms [35].

single to few-layer graphene.[34] Prior to graphene growth the SiC substrate surface needs to be cleaned by H_2 etching at 1000 ^{o}C in UHV to remove native oxide that is often present. This method results in Graphene growth on both Si and C terminated faces of SiC. Figure 2.2 shows the STM image of graphene grown on semi-insulating C-face SiC.[35] In general, the growth on Si-face is slower and self- limiting, resulting in thinner and better quality graphene (1-3 monolayers), whereas graphene on C-face is usually much thicker (5 – 10 monolayers). The major advantage of this technique is growth of quite uniform, wafer scale and high quality graphene is possible, taking advantage of the precise control of process parameters in a commercial SiC growth chamber. Attempts have also been made to grow graphene on SiC substrate in near atmospheric Ar pressure of 900 mbar and at relatively higher temperature of 1650 ^{o}C with a goal to obtain larger area low defect, mono, bi and tri-layer graphene.[36] One of the disadvantages of this method of graphene synthesis is that

it is very difficult to remove or transfer the graphene to another desired substrate, due to the challenges involved in controllably etching SiC. Therefore, processing of graphene devices needs to be done on the SiC substrate itself. This can be expensive due to the high cost of SiC substrates, and also it does not readily allow the usage of a back gate for realizing transistors, or sensors requiring back-gate modulation.

2.3   Reduced Graphene Oxide

It is chemical route to make graphene from graphite. In this method graphite is oxidized in presence of strong oxidizing agents such as sulphuric acid. A redox reaction takes place in between graphite and oxidizers in which electrons are removed from graphite. The most common method to produce graphite oxide is treating graphite with a mixture of sulphuric acid, sodium nitrate and potassium permanganate. Due to the oxidation process the interplanar spacing between the layers of graphite is increased. The
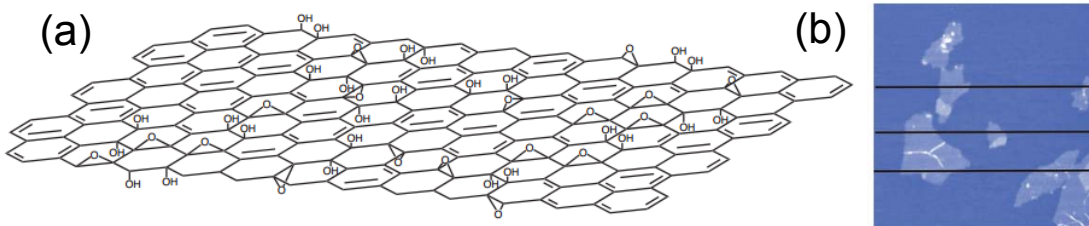
Figure 2.3 (a) Chemical structure of graphene oxide. There are carboxylic and carbonyl groups at the edges but are not shown for clarity. (b) AFM image of exfoliated 1 nm thick graphene oxide sheets [37].

resulting product is graphite oxide. When this graphite oxide is dispersed in solvents like water, graphene oxide results by interaction of water molecules in-between increased separation of interplanar spacing of graphite oxide which helps to separate these layer of graphene oxide using sonication or stirring. This process causes lots of damage to graphene

oxide. The process of reduction of graphene oxide back to individual graphene layers introduces even more defects, therefore the resulting product is called reduced graphene oxide (rGO). Figure 2.3(a) shows chemical structure of graphene oxide and Figure 2.3(b) shows exfoliated graphene oxide.[37] There are various methods of making rGO from graphene oxide such as thermal, chemical and electrochemical means. Some of these techniques can produce very high quality rGO, similar to pristine graphene, but can often be complex or time consuming in nature. The very common technique to make rGO involves, treating GO with hydrazine hydrate at 100 for 24 hours. rGO is ideally suited for large scale industrial application such as energy storage where good quality graphene is not strictly required.

2.4   Chemical Vapor Deposition Growth of Graphene

Chemical vapor deposition (CVD) involves the activation of gaseous reactants or precursors and the subsequent chemical reaction, followed by the formation of a stable solid deposit over a suitable substrate. The energy for the chemical reaction can be supplied by different sources such as heat, light, or electric discharge as in thermal, laser-assisted, or plasma-assisted CVD respectively. Two types of reactions could be possible for the deposition process namely homogeneous gas-phase reactions, which occur in the gas phase and may results in formation of powders, and heterogeneous chemical reactions which occur on or near a heated surface leading to the formation of powders or films. Though CVD can be used to produce ultrafine powders, but in case of depositing extremely thin graphene films heterogeneous chemical reactions should be favored and homogeneous chemical reactions are avoided during the designed experiments. Figure 2.4 shows a schematic diagram of a typical CVD process to grow graphene in a tubular furnace[38]

illustrating the generalized steps which involves reactant transport, their activation by thermal means, transport of reactant by gas phase diffusion through a boundary layer, adsorption, chemical reaction, growth, desorption, removal of reaction product etc.

The CVD technique of graphene growth has assumed prominence due to its ability
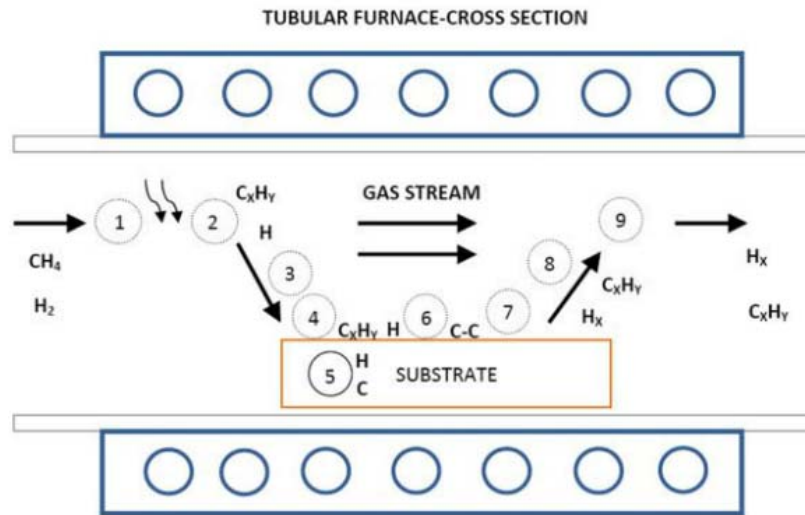
Figure 2.4 The generalized CVD growth of graphene on top of a metal catalyst. The steps involved are: reactant transport, activation, transport of reactant thought boundary layer, reactant adsorption on the surface, dissolution and bulk diffusion, chemical reaction, surface migration, film growth, desorption, transport of product through boundary layer, and transport by forced convection [38].

to grow large area, monolayer, low defect graphene on inexpensive substrates such as cold rolled, high-purity (99.999%), 25 μm thick Cu foils using inexpensive CVD growth hardware and operational cost. There are host of parameter ranges such as atmospheric pressure to ultra-high vacuum, range of precursor gas ratios, different types of transition metal catalyst as substrate and the range of growth temperature that had been explored to grow graphene by CVD technique. Each of the CVD system, that has reported graphene growth, usually has a window or small range of parameters for most optimized growth

which also depends upon the system hardware and its capability. The basic understanding of growth mechanism is needed in order to find suitable parameters for optimizing graphene growth with a given hardware.

The CVD of large-area, monolayer graphene on transition metal films and foils has been widely explored recently. In spite of the significant progress, CVD-grown graphene remains a polycrystalline film made of micrometer- to millimeter-size domains. It has been observed that, the graphene films grown on Ni foils or films do not yield uniform monolayer graphene. In most cases, a mixture of monolayer and few layers (polygraphene) are obtained. Whereas the use of Cu substrate has proved to be excellent candidate for making large-area, uniform thickness (95%), monolayer graphene due to the low solubility of C in Cu. It was suggested and even demonstrated that the graphene growth on Cu is surface-mediated and self-limiting. In this work the CVD of monolayer graphene was optimized by iteratively going through various parameters such as:

- Evaporated thin film verses thicker foil based metal substrate

- Ni foil verses Cu foil based CVD

- Annealing time

- Growth temperature and time

- Ratio of precursor gases

2.4.1 Home Built Graphene CVD System

A crude CVD reactor was built from scratch which involved a round tube furnace, the quartz tube reactor, the precursor gases: CH_4, H_2, and Ar controlled by flow meters, and a low capacity (up to 9 Torr) DryFast diaphragm pump. The gases tanks were connected by polyethylene tubing. There was no good control on flow rates of gases,

pressure and temperature of the system. Under these condition Ni is likely to give an indication of graphitic material growth due to its higher solubility of C atoms. Therefore 300 nm thick evaporated Ni film was used as a substrate for CVD of graphene. Raman characterization (discussed later) suggested the growth of monolayer to few-layer discontinuous graphene film. After getting the initial conformation of growth the CVD systems was revamped to optimize good quality monolayer graphene growth.

The new CVD setup consists of the three gas cylinders, each for CH_4, H_2 and Ar to the corresponding mass flow controllers (MFC) through manual valves and ¼" stainless steel tubing. The stainless steel tubing serves to provide higher conductance path and better leak characteristics as compared to polyethylene tubing. The MFCs were MKS Type 1179A each calibrated for the gas being used. Ar MFC was 1000 sccm range for flow larger amount of Ar and a carrier and diluent gas. H_2 and CH_4 MFCs were 200 and 50 sccm range for keeping CH_4 to H_2 ratio low during the growth. The output from MFCs are joined together using a Swagelok Union Cross. One end of the cross is connected to the ¼" quartz delivery tube by a stainless steel bellows. The reaction chamber consist of 1½" diameter wide and 2' long quartz tube. It is also fitted with ¼" thick compressed BN heat blocker at both the ends. The enclosure is formed by stainless steel end caps with sleeves. The sample or substrate is mounted on a flat quartz boat. The other end of the chamber has one outlet connected to stainless steel tubing with bellows. A barometer and a Pirani gauge (MKS 901P, loadlock transducer) are attached downstream to this stainless tubing to monitor the pressure of the system. This tubing then connects to the inlet of a mechanical pump. The mechanical pump is a rotary vane pump from Pfeiffer Vacuum (Model: Duo 10 M) with a capability of 4.5 mTorr ultimate pressure. However the base system pressure remains in

the range of 100 mTorr. The outlet of the pump is connected to room exhaust line though a manual valve which keep the CVD system isolated from exhaust and saves from occasional oil leak of other pumps which are also connected to exhaust. The quartz tube reactor is housed inside a horizontal single zone split tube furnace from Carbolite. This furnace is capable of operating at 1100 °C for prolonged hours and takes about 45 min to reach that temperature. The temperature is controlled by Carbolite 301 controller. Split furnace was chosen to have a faster cooling rate which has bearing in Ni based CVD and also to cut-down process time. Figure 2.5 shows the picture of this home built graphene CVD system where precursor gas cylinders and mechanical pumps are not in the frame.

Figure 2.5 The home-build CVD graphene growth system

The picture shows stainless steel tubing, MFCs, their controller and read-outs, horizontal split-tube furnace and its controller, quartz tube reactor fitted with stainless steel ends caps, pressure gauge and read-out etc.

2.4.2 Growth on Thin Film

In initial attempt graphene growth was carried out Ni and Cu thin films. We evaporated 5 nm of Ti and 300 nm of Ni sequentially on top of 100 nm thick thermally grown SiO_2 on high conductivity p type Si. The role of Ti was to act as sticking layer in-between SiO_2 and Ni. For copper catalyst we used 300 nm of e-beam evaporated Cu on top of silicon wafer. The samples are loaded in BN boat at room temperature in a 1½" diameter
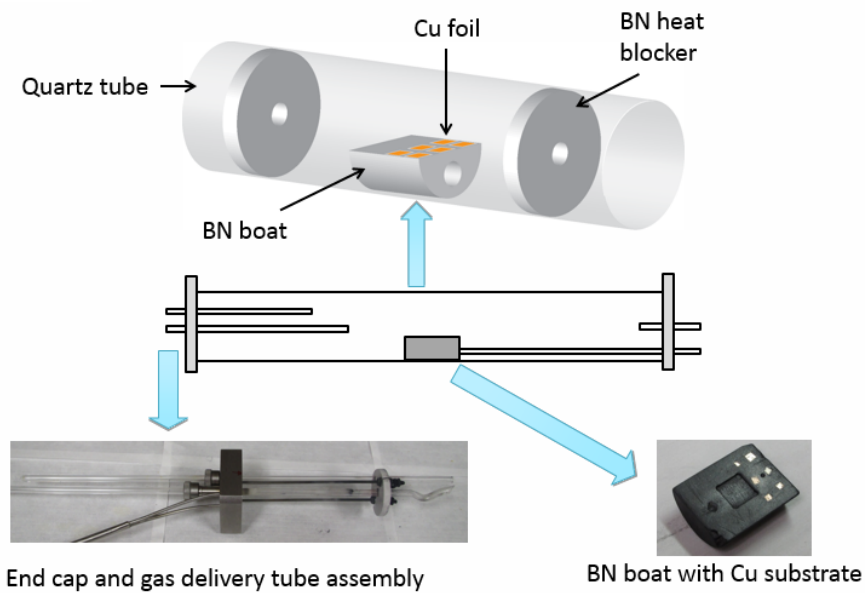
Figure 2.6 Schematic of CVD reactor chamber consisting of quartz tube and stainless steel end caps. BN heat blocker and boats are shown along with end cap.

quartz tube as shown in Figure 2.6. Roughing is done by a low capacity Diaphragm pump first and then Ar and H_2 are flown into the system at a flow rate of 470 and 40 sccm respectively. The system temperature is ramped to 1000 ℃ the desired growth temperature. All the gases used here are ultra-high purity (UHP) quality which means their purity is more than 99.9995 %. Ar is used as a carrier gas. A 10 minutes of annealing is also done at growth temperature to allow some recrystallization of metal catalyst and also their cleaning by H_2 as well. The flow rates for Ar and H_2 are reduce to 100 and 10 sccm. After

24

this the precursor gas i.e. CH$_4$ is flown for 30 minutes with a flow rate of 50 sccm along with Ar and H$_2$ with 40 and 5 sccm flow rates. After this step CH$_4$ and H$_2$ flows are stopped. The parameter optimization became difficult in evaporated thin films. Structural
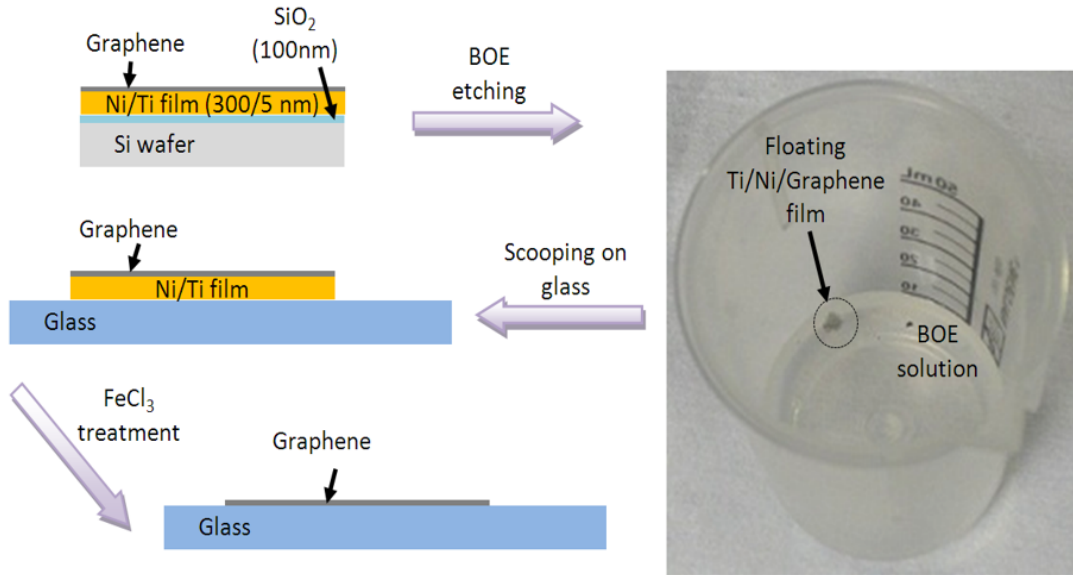
Figure 2.7 Series of steps involved with transferring graphene from Ni film to a glass substrate.

characterization such as Raman spectroscopy revealed a discontinuous growth on Ni films with small domain size. There was no growth observed on Cu films.

Apart from poor growth and coverage on Ni films the film based CVD of graphene suffered from complicated transfer technique. The transfer process involved first the dissolution of SiO$_2$ in buffered oxide etchant (BOE) which separates Si substrate and CVD graphene on 300 nm Ni film. Thereafter scooping the film by a glass substrate and then further treating it in a Ni etchant such as FeCl$_3$. Some of these etchant may get trapped in-between glass substrate and graphene. Figure 2.7 captures the major steps of this transfer process. Due to sum total of difficulty in growth optimization and transfer process other

avenues of growth and transfer were explored such foil based CVD of graphene on Ni and Cu foils.
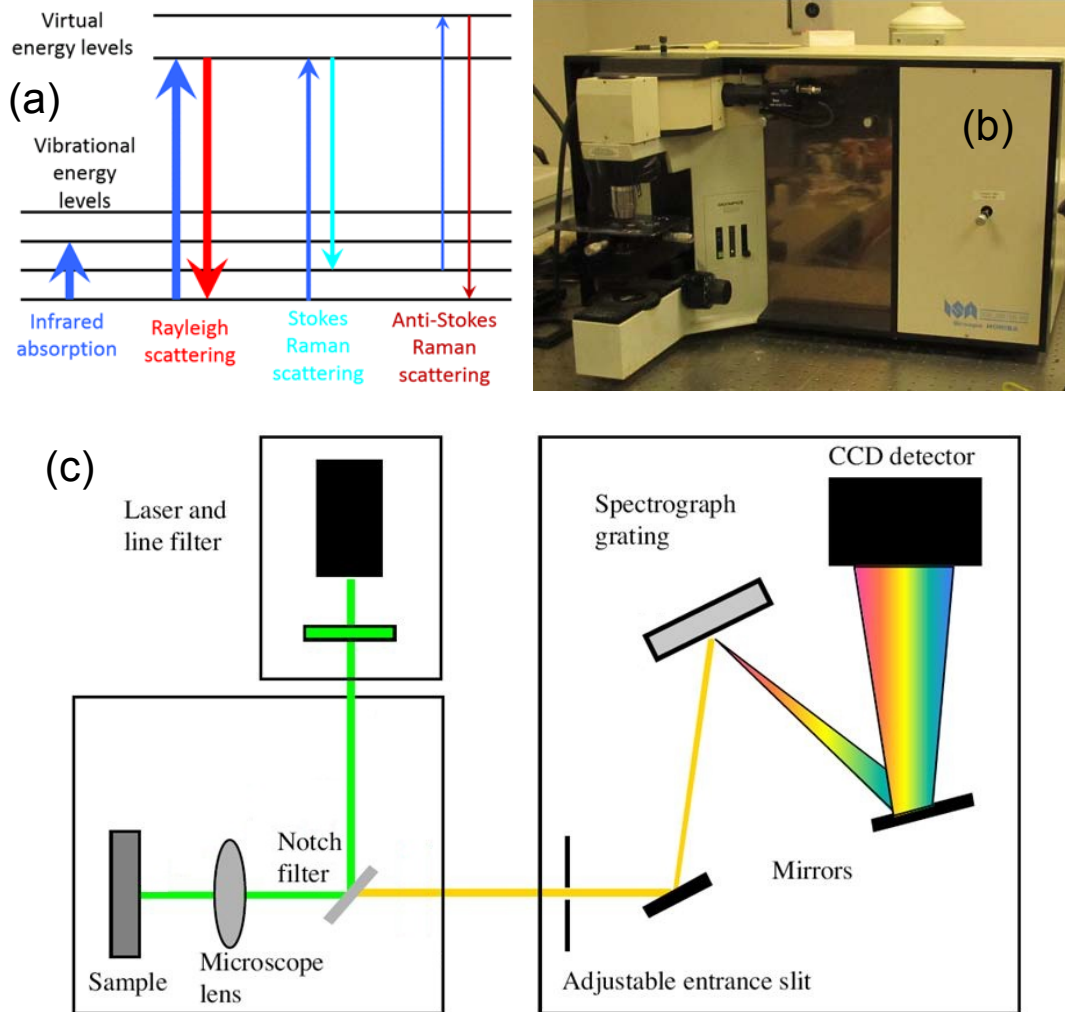
Figure 2.8 (a) The basic physics of Raman scattering involving ground state vibrational levels and virtual states. Infrared absorption is also shown for comaparison. (b) LabRAM Raman Spectrometer from Horiba used in this work. (c) The ray diagram of Raman spectrum set-up consisting of Laser, notch filters, lenses, grating and CCD detector [40].

2.4.3 *Growth on Foils*

Due to optimization problems in thin film based graphene growth, it was attempted on 25-50 μm thick Cu and Ni foils. These foils are polycrystalline in nature and can be

annealed at higher temperature to improve crystalline properties of the material to facilitate good quality growth. They also simplify and improve the graphene transfer process by obviating the need to use HF based solvents to etch SiO_2. It was determined by performing
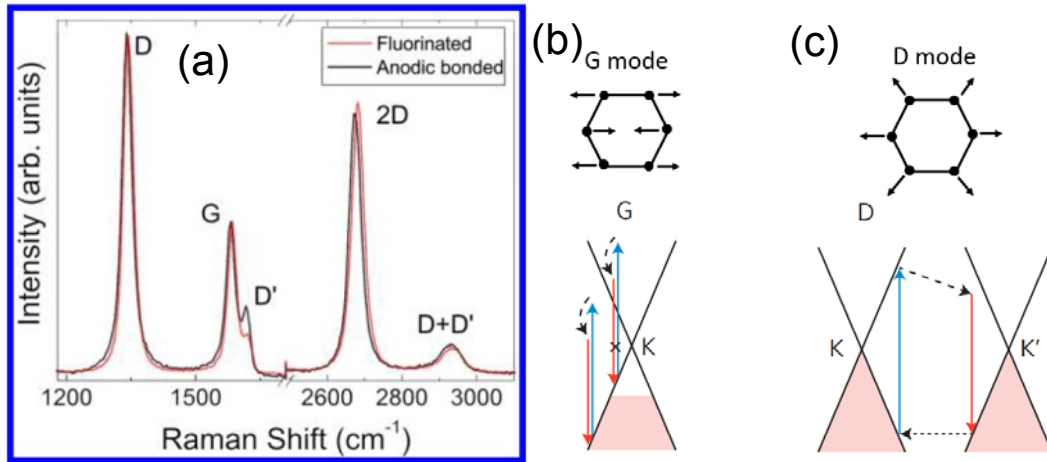
Figure 2.9 (a) Raman spectra of fluorinated and anodic bonded graphene depicting peaks of interest in 1200 to 3000 cm^{-1} range in a defective graphene [41]. (b) G band resulting from in-plane C-C band stretching of the ring and is characteristic of sp^2 carbon system. Electron excitation and phonon generation is shown as resonance process in the E-k diagram of graphene. (c) The radial breathing mode responsible for D peak. It involves intervalley phonon and defect scattering [43].

series of growth on top of Ni and Cu foils, and also by following the published report, that Cu foils are the material of choice for single layer graphene growth. The detailed discussion on foil based CVD follows after the discussion of graphene characterization.

2.5 Raman Characterization of Graphene

In order to understand the type and quality of CVD graphene and to device the strategy to improve the CVD, a reliable and quick feedback is very important. In case of graphene Raman spectroscopy provides quick and immediate feedback on as-grown graphene on metal catalyst without any need for sample preparation. In fact Raman

spectroscopy was used to determine if the thin film based CVD of graphene is suitable since it will require very large extent of optimization.
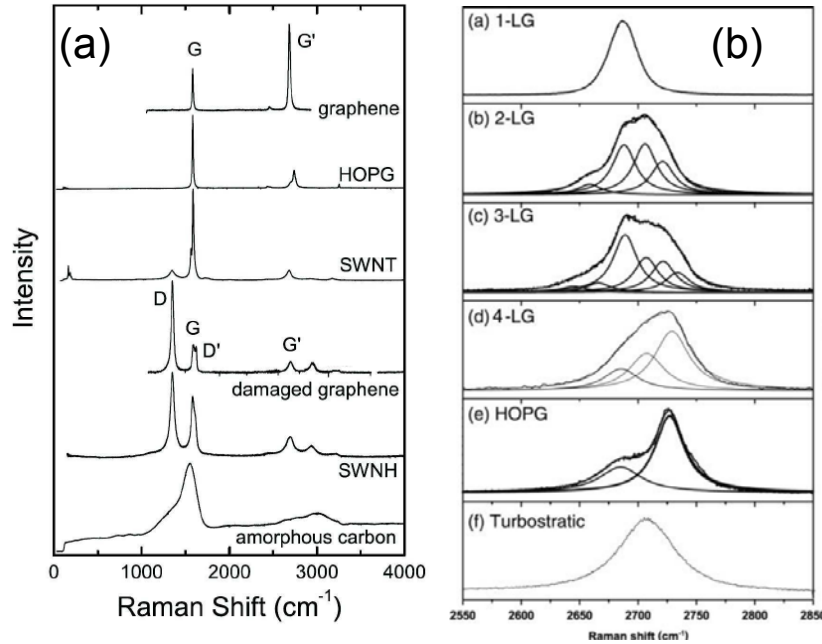
Figure 2.10 (a) Raman spectra of various sp^2 carbon based system showing ability to distinguish them based upon intensity, shape and with of D, G G' or 2D peaks using one simple scan of Raman spectrum [44]. (b) Using the shape of 2D band it is possible to distinguish graphene from graphite and also determine the numbers of monolayers by fitting different Lorentzians to the band [44].

Raman spectroscopy is based upon vibrational spectrum of a material system. It is becoming increasingly popular in detecting organic, inorganic species and crystallinity of the system. It is sensitive to strain and can detect stress in the semiconductor in very small region due to the ability of focusing light beam in very small region. The interaction of incident waves to matter results in scattering of waves apart from other effects such as absorption or transmission. The scattered waves can be of three types, the predominant Raleigh scattered light which has same wavelength as that of the incident wavelength as seen in Figure 2.8(a). The other two types have different wavelength or energy than those of incident photons and are called Raman scattered. These scattered photons interact with

optical phonons of the material therefore contain the material information.[39] When incident photons impart energy to the lattice by emitting a phonon, the scattered photon comes out with lower energy or higher wavelength and the process is called as Stoke shifted scattering. On the other hands if a phonon in absorbed in scattering process it is referred as anti-Stoke shifted scattering as seen in Figure 2.8(a). Anti-Stoke scattering has lower probability process than Stoke scattering therefore in Raman spectrum Stoke shift is measured. However entire Raman scattering is very low probability process as compared to Raleigh scattering (~1 in 10^8 parts) therefore a strong monochromatic light source such as laser is a must for obtaining Raman spectrum. Figure 2.8(c)[40] shows a simplified schematic of Raman setup consisting of laser source, notch filters to avoid Raleigh scattered photon, grating and CCD detector to measure the spectrum. Figure 2.8(b) shows the image of Raman spectrometer setup, LabRAM 1B from Horiba.

The Raman peaks of interest in graphene material system for routine characterization lies in the Raman shift range of 1200 to 3000 cm^{-1} as shown in Figure 2.9.[41] This spectrum corresponds to a defective graphene to capture all possible peaks in the range of interest since some of the peaks may be absent in good quality graphene. The prominent peaks in the Raman spectra of graphene system are G and 2D bands occurring at ~1580 cm^{-1} and ~2700 cm^{-1} respectively. The G band corresponds to doubly degenerate in-plane transverse optic (iTO) and longitudinal optic (LO) phonon mode that corresponds to E_{2g} symmetry at the Brillouin zone canter.[42] Physically speaking, it result from bond stretching of all pairs of sp^2 atoms both in rings and chains as seen in Figure 2.9(b).[43] It is the only band that occurs from first order Raman scattering process in the graphene. The presence of G peak confirms the presence of carbonaceous material with sp^2 bonding and

its intensity is proportional to the thickness of the carbonaceous material. The other prominent band 2D results from a second order scattering process that involves double resonance and two iTO phonons near K point.

There are two defect related peaks in graphene referred as D and D'. The D band corresponds to the double resonance radial breathing modes of sp^2 bonded atoms in the ring (Figure 2.9(c)[43]) and D' corresponds to sp^3 hybridization in the system. These bands are Raman forbidden and only occurs when the periodicity of hexagonal lattice is broken by a point defect, grain boundary, line defect, graphene edge, dopant atom etc. since D band involves one iTO phonon and a defect. The 2D band gets its name for being overtone of D band which means ω_{2D} is about twice the ω_D.
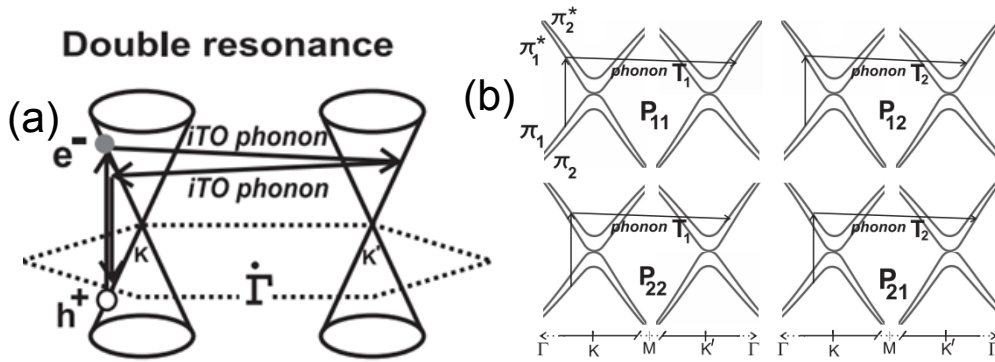
Figure 2.11 (a) A two-phonon second-order Raman spectral processes giving rise to the G' or 2D band (b) Schematic view of the electron dispersion of bilayer graphene near the K and K' points showing two bands. The four DR Raman processes are indicated as P_{11}, P_{22}, P_{12}, and P_{21} [42].

The shape, width, position and relative intensities of these bands or peaks helps in distinguishing between graphite, graphene and various other sp^2 based C systems such as carbon nanotubes. Figure 2.10(a) captures this ability of Raman spectroscopy to distinguish between various carbon based materials very clearly such as amorphous carbon, CNTs, pristine and defective graphene and HOPG.[44] It also helps in determining the number of

monolayers present in the sample, based upon shape and width of 2D band, by fitting various different types of Lorentzians as seen in Figure 2.10(b).
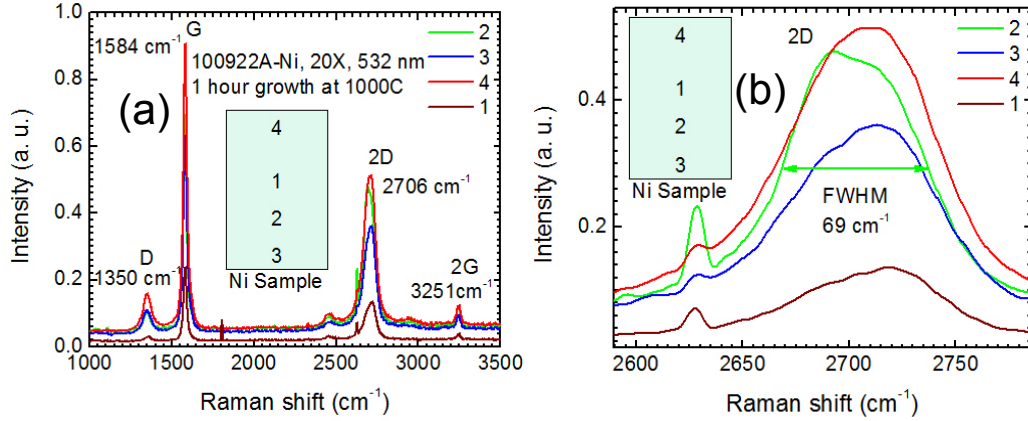
Figure 2.12 (a) Raman spectra of CVD graphene on 300 nm thick Ni film on SiO_2. The different intensity of G peak corresponds to different thickness of graphene at different location in 4 × 7 mm Ni sample. (b) The blown up images of 2D band shows the presence of multi-layer graphene due to broadening (FWHM of 69 cm^{-1} at location 2) that may consist of many Lorentzian peaks.

The 2D peak in graphene is the result of double resonance process and is coupled to electron and phonon in graphene dispersion relations. Electron-phonon scattering along KΓK' directions has to satisfy the scattering process shown in Figure 2.11(a)[42] as per selection rules. A monolayer exfoliated graphene sample at room temperature exhibits a sharp 2D peak consisting of single Lorentzian feature with a full width at half maximum (FWHM) of ~24 cm^{-1}. The intensity of this peak relative to G peak is very high sometime reaching to 4 time more intense than G peak or I_{2D}/I_G ~ 4.[45] This very large intensity of 2D peak in monolayer graphene has been associated to the triple resonance process.[42] In bilayer graphene with Bernal (ABAB) stacking both electronic and phonon bands split in special manner as shown in Figure 2.11(b)[42] for electronic band structure. This leads to 4 different possibility of transition and hence phonon emission. These transitions give rise to

4 different Lorentzian in 2D spectrum of bilayer graphene. The sum total of these peaks are observed as a broadened 2D peak (Figure 2.10(b)) with reduced intensity to that from a monolayer graphene. Similarly trilayer graphene has 6 possible transition leading to six possible Lorentzian with about ~24 cm^{-1} FWHM that can be fitted with 2D peak giving broader line width and smaller intensity to 2D peak of trilayer graphene as in Figure 2.10(b).[44] The 4 layered graphene 2D peak (as seen in Figure 2.10(b)) shows 3 Lorentzian. Five monolayers and beyond the shape of 2D peak becomes similar to that of HOPG or graphite 2D peak. As seen again in Figure 2.10(b), the HOPG 2D peak consists or two Lorentzian. One is about half the intensity of the other which given a distinct shoulder to graphite 2D peak. Figure 2.12(a) shows the Raman spectra taken at 4 different location on a 5 mm × 10 mm size 300 nm thick evaporated Ni film on SiO_2. The D peak intensity suggest low defect concentration in CVD graphene on Ni film. However 2D peaks in Figure 2.12(b) suggest multilayer graphene due to a larger value of 69 cm^{-1} in 2D FWHM. Since the 2D peak shapes are different at differ location therefore multilayered graphene thickness is non-uniform across the sample.

The graphitic system such as HOPG and pyrolytic graphite (PG) have only $2E_{2g}$ vibrational mode Raman active, occurring at 42 and 1581 cm^{-1} along with three distinct second order features at ~2440, ~2730, and ~3240 cm^{-1}.[46] These second order features or overtones have been attributed to overtone scattering from the features in the density of states in the graphite system.[47] In graphene system (monolayer or few-layers) these overtones are also observed of which the one occurring around 2700 ± 50 cm^{-1} is referred as 2D band. The other two overtones has been observed at 2451 and 3251 cm^{-1}, can be seen in Figure 2.12(a) along with 2D peak, in our few-layer graphene sample grown on Ni film,

which were probed with 532 nm laser. The first overtone has also been observed at 2464 cm^{-1} with 632 nm laser excitation on as-grown graphene on Cu and transferred graphene on SiO$_2$.

The information on layer thickness determination is valid for ABAB type Bernal stacked graphene which are obtained by exfoliation of HOPG. The multi-layered graphene obtained by epitaxial method or CVD, in which different layers may random orientation with other is called turbostratic graphene. Due to the random orientation of layers with each other there is very little interaction in-between them, therefore the electronic structure of turbostratic graphene looks almost like a monolayer graphene. This reflect in 2D band of the turbostratic graphene in Figure 2.10(b) which shows it as a single Lorentzian similar to the 2D of monolayer graphene. However it is still possible to distinguish turbostratic from monolayer graphene. There is good amount of broadening of 2D feature due to relaxation of the double resonance Raman selection rules associated with the random orientation of the graphene layers with respect to each other. Therefore FWHM of ~45-60 cm^{-1} is observed in single Lorentzian 2D peak of turbostratic graphene as oppose to 24 cm^{-1} in that of monolayer.[42] The I_{2D}/I_G is also reduced considerably in the range of 0.2 to 0.6 and the position is blue shifted.[48]

The D peak as mentioned before corresponds to amount of disorder or defect in graphene material system. Intensity ratio of D and G peaks in graphene (I_D/I_G) helps to quantify the amount of defects and disorder. In general when I_D/I_G is high then the material is considered highly defective. When the ratio of I_D/I_G is less than 0.3 it considered a good quality graphene having lesser density of defects and disorder. Broadly speaking the intensity ration can quantify two types of defects in graphene. The line defects arising from

smaller graphene crystallite size, L_a or point defects due to absence of C atoms or inclusion of impurity atoms in graphene. The graphene crystalline size in nm is given by the following expression.[49]

$$L_a(nm) = (2.4 \times 10^{-10})\lambda_l^4 \left(\frac{I_D}{I_G}\right)^{-1} \qquad (2.1)$$

Where λ_l is the wavelength of the laser in nm used for Raman spectrum measurements. During the optimization process the small crystalline size of graphene were observed for
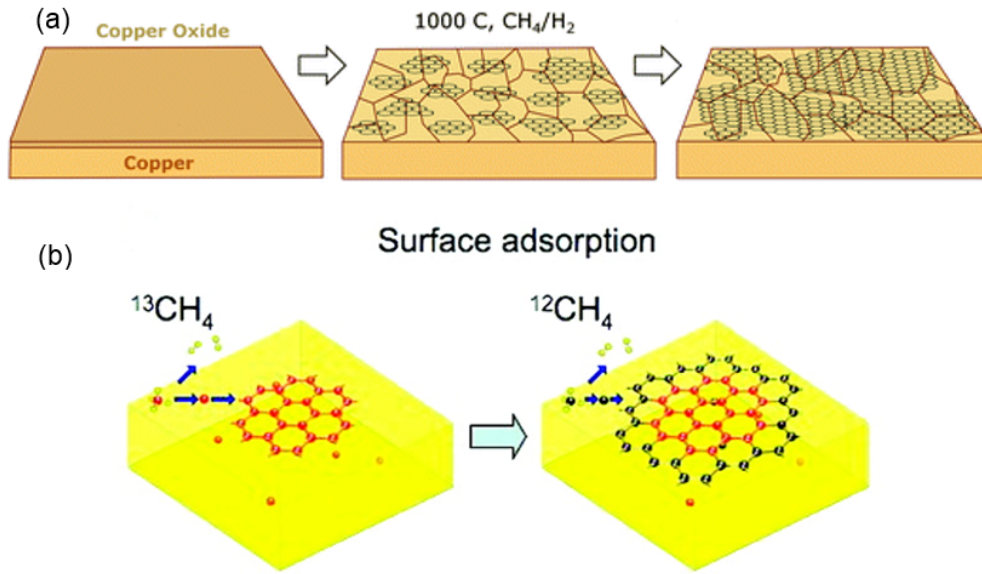
Figure 2.13 (a) The graphene growth mechanism on copper foils [51]. (b) The graphene growth by surface adsorption as revealed by use of C13 and C12 isotopes of carbon [52].

CVD graphene on Cu which will be useful as defective graphene for sensitivity enhancement and will be discussed in chapter 4. In graphene with zero-dimensional point defects, the distance between defects, L_D, is a measure of the amount of disorder in the sample and is given by expression 2.2. [50]

$$L_D^2(nm^2) = (1.8 \pm 0.5) \times 10^{-9}\lambda_l^4 \left(\frac{I_D}{I_G}\right)^{-1} \qquad (2.2)$$

In low defect density regime, when $L_D \geq 10$ nm, it possible to estimate the point defect density in graphene, n_D, by the expression given below.

$$n_D(cm^{-2}) = \frac{(1.8 \pm 0.5) \times 10^{22}}{\lambda_l^4} \left(\frac{I_D}{I_G}\right)^{-1} \qquad (2.3)$$

2.6 Growth on Ni Foil

Ni has very high solubility of carbon atoms at higher temperature exceeding 0.1 atom % at 1000 ℃. The solubility decreases with temperature and extra carbon atoms are segregated out resulting in thicker graphene growth. Due to higher solubility the graphene
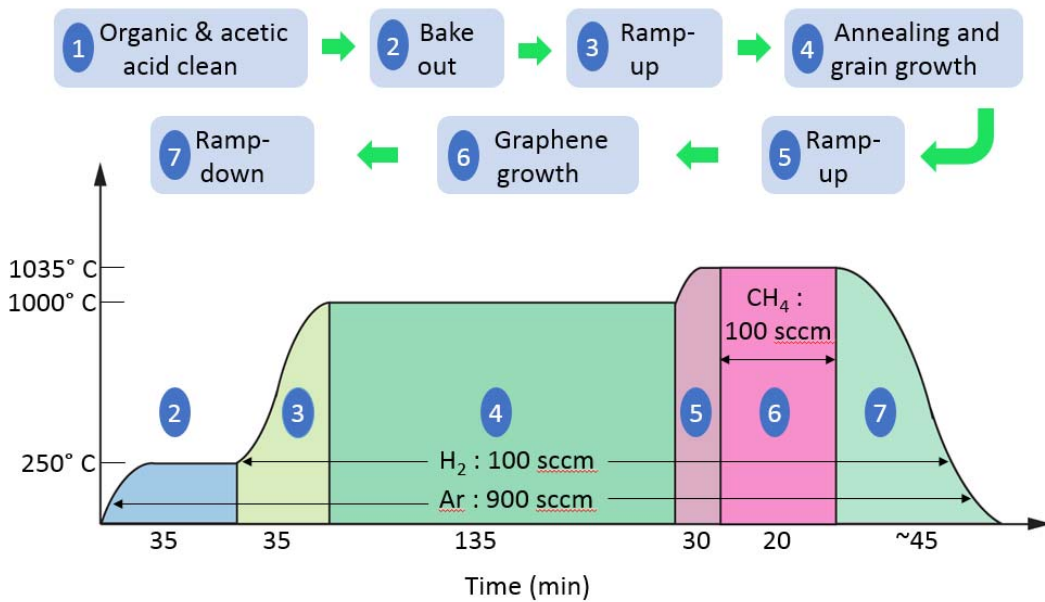
Figure 2.14. Series of steps involved in growing monolayer graphene on Cu foils. The optimized process parameter are shown in the schematic plot.

thickness depends upon growth pressure, concentration or flow rate of CH_4, and rate of cooling. Ni is ideal material to optimize graphene growth when the set-up is made from scratch. It helped us in getting a baseline parameters to grow graphene, although thicker but good quality. However the thinner graphene, six monolayers or small, also referred as

35

few layer graphene (FLG) could be obtained by rapid cooling of the growth system from 1000℃ to room temperature within minutes. Therefore it was needed to choose a material with low C dissolution.

2.7   Growth on Cu Foil

By virtue of low solubility of C atoms in Cu (< 0.001 atoms % at 1000℃) growing thinner (mono and bi-layer) graphene becomes easier compared to Ni. Here thinner graphene layer is not affected much by cooling rates and CH_4 flow rates. The growth mechanism is surface adsorption of C atoms on Cu. At growth temperature say 1000℃ carbon atoms are releases on Cu by dehydrogenation. These released atoms then grow by nucleation and growth as more C atoms are added to the periphery. They keep growing till they become large enough and coalesce to form full coverage of film. Figure 2.13(a) show the schematic of this growth mechanism on Cu foils.[51] The use of C13 and C12 isotopes clearly indicates the surface adsorption type growth mechanism owing to low carbon solubility in Cu. This is illustrated in Figure 2.13(b) as reported by Li *et al.*[52] where red colored C13 isotope is delivered to Cu foil at growth temperature by $^{13}CH_4$ and graphene starts to grow by nucleation and growth. When the gas was switched to $^{12}CH_4$ the black colored C12 carbon atoms continued the growth by getting embedded to the periphery of the red colored C13 carbon based growing grain. This suggests that C doesn't go in the bulk of Cu foils, therefore it does not segregate out at random places resulting into thicker graphene growth. These conclusion were drawn by Li *et al.* using Raman mapping and are indicative of the fact that the copper is the material of choice for thin graphene growth.

We optimized our graphene growth on Cu. The optimization involved a good cleaning procedure for getting rid of copper oxides such as CuO and Cu_2O which are

present in cold rolled Cu foils. The Cu foils were first cleaned in acetone and isopropanol

and then sonicated in acetic acid to remove oxide. They were loaded in growth chamber

under Ar over pressure. The system was evacuated and then Ar was flown at 250℃ for
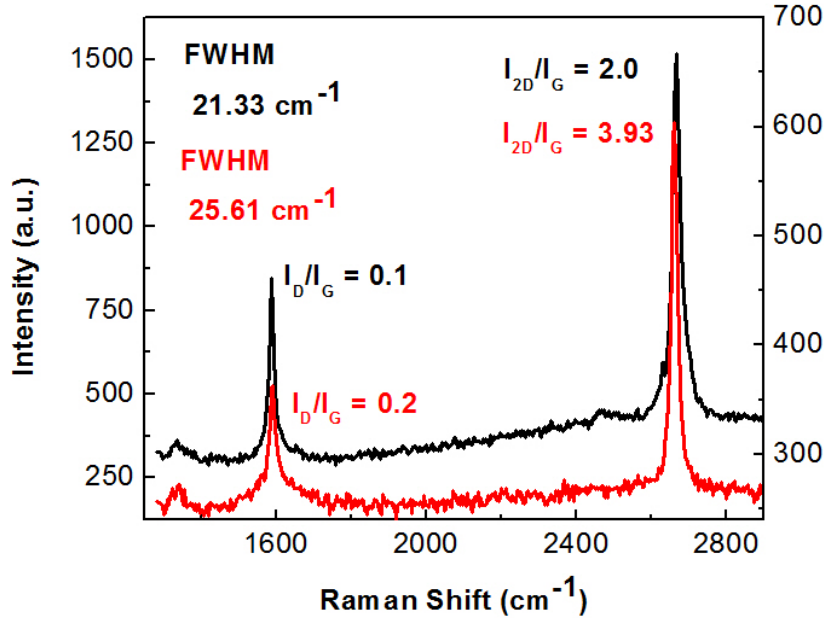
Figure 2.15 Raman spectra of two samples of graphene as-grown on Cu foils by
CVD growth technique with optimized parameters. The 2D FWHM of 21.3 and 25.6
is indicative of monolayer graphene.

bake out. H_2 was flown for 2 hours at 1000℃ to anneal Cu to increase its crystalline quality

and remove any remaining and newly formed oxide. The actual growth was performed at

further elevated temperature of 1035℃ in presence of CH_4. The forced cooling was done

by use of a fan. It takes about 45 minutes to cool down the system to 100℃. Figure 2.14

shows the optimized process parameter and sequence of steps for graphene growth. Raman

spectrum of graphene on Cu foils are shown in Figure 2.15. It plots the spectra for two

different graphene samples. Both the samples show very low defect density as indicated by

I_D/I_G value of 0.1 and 0.2. The I_{2D}/I_G value of 3.9 and 2.0 along with 2D FWHM of 25.6

and 21.3 cm^{-1} clearly indicate the presence of monolayer CVD graphene on 25 μm thick foils.

In summary a CVD reactor was set-up to perform graphene grown on transition metal substrates. The reactor was built by assembling different components such as quartz tube chamber, horizontal split furnace, mechanical pump, MFCs and pressure gauges. The optimized process parameter were obtained by understanding growth mechanism and by performing series of growth on different types of substrates and under different growth conditions. The quality of growth was assessed by Raman spectroscopy on as-grown samples. The device fabrication of CVD graphene would require the development of a reliable graphene transfer process on any desirable substrate and also of device processing techniques. The next chapter address the processing and the sensor development effort from graphene based devices.

CHAPTER 3

SENSING APPLICATIONS OF GRAPHENE

3.1 Introduction

Graphene has drawn huge research interests in sensing applications due to its extraordinary material properties including remarkably high charge carrier mobility of 200,000 cm^{2}V^{-1}s^{-1},[16] very high thermal conductivity[53] and mechanical strength,[21] as well as high degree of chemical inertness at room temperature.[1] The 2D nature of graphene along with its unsaturated C-C (sp^2) bonding makes it highly suitable for sensing applications. The 2D nature makes it essentially a surface, enabling analyte molecules to adsorb very efficiently and produce a large change in its physical properties. On the other hand, the presence of unsaturated sp^2 bond makes it sensitive to a large variety of analytes that can adsorb on its surface and exchange charge with it or modify its surface properties. These exceptional material properties have led to the demonstration of graphene based sensors that are capable of detecting down to a single analyte molecule.[24] Some of the properties of interest in sensing applications are listed in Table 3.1.

In spite of these highly promising aspects of graphene for sensor development, it still suffers from lack of selectivity in detecting molecules which has been studied in this dissertation. In addition, the absence of bandgap and inability to change its resistance appreciably under strain, which makes its potential applications in optoelectronic devices

and nanoelectromechanical systems (NEMS) rather challenging for certain applications. The lack of bandgap in graphene also results in low turn-off ratio in graphene transistors, which makes it unattractive for use in integrated circuits. Therefore, other 2D materials are also being pursued for sensing beyond graphene, and the heterojunctions of these materials as well as other traditional semiconductors with graphene are being considered, for sensing applications where graphene by itself is not capable enough.

Table 3.1 Electronic and Material Properties of single layer graphene

Mobility	6.5×10^4 [54] - 10^6 cm^{2}V^{-1}s^{-1}[55]
Thermal conductivity	$(4.84 \pm 0.44) \times 10^3$ to $(5.3 \pm 0.48) \times 10^3$ W/mK[53]
Young's modulus	1.0[21] to (2.4 ± 0.4) TPa[56]
Breaking strength	42 N/m [21]
Breaking strain	25% [21]
Normalized noise spectral density (at f = 10 Hz)	10^{-9} to 10^{-7} Hz^{-1} [57]
Noise amplitude (µm scale devices)	$\sim 10^{-9}$ to 10^{-7} [57]

3.2 Graphene Sensors

Two broad category of graphene sensor has been demonstrate so far based upon the quantity or stimuli being sensed. These are physical sensors which have been shown to sense physical quantities such as pressure, strain, magnetic field, IR etc., whereas chemical or biological sensors of graphene have been shown to sense various analytes such as ppm or sub-ppm level of NO$_2$ etc. and various kinds of bio-molecules and bio-markers.

3.2.1 Physical Sensors

Due to its outstanding electronic properties, mechanical strength and single atomic layer thickness,[16, 21, 58, 59] graphene can be considered as the ultimate building block for

nanoelectromechanical systems, which are capable of sensing a host of physical parameters including pressure, mass, charge, electric potential, temperature, and magnetic field. Graphene NEMS can also be used as a versatile device for various RF applications. NEMS resonator has been reported from all three basic types- exfoliated,[60] epitaxial,[61] and CVD[62] graphene. Graphene with its linear energy dispersion relationship and zero bandgap can absorb also light from mid-infrared (mid-IR) to ultraviolet wavelength range with almost flat (2.3% for monolayer thickness) absorption spectra which makes it very attractive for optical detector. Percentage increase in light absorption can be possible by employing multilayer graphene. Graphene based IR camera has been reported already.[63] In addition, graphene bolometer,[64] Infrared (IR) detector based upon quantum Hall effect (QHE),[65] and magnetic field tunable IR detector based on Landau Level (LL) formation[66]

Table 3.2 Graphene based physical sensors and their applications

Physical Sensors	Sensing Mechanism	Applications
NEMS Resonators	• Capacitively coupled mechanical resonance • Ultra high quality factor • Gate tenability[62]	• Ultrasensitive mass sensing[67] • Probe for electrical and magnetic properties of lower dimensional materials[58] • High frequency oscillator, filter, modulator, mixers, etc.[68] • Chemical Sensing
Magnetic field sensors	• Detection of magnetic field by Hall Effect[69, 70] • Gate tunable sensitivity[71]	High density magnetic storage application
IR and THz sensor	Light absorption from mid-IR to UV.	• Bolometric Sensor[64] • QHE effect based IR photodetector[72] • Asymmetric contact IR detector[63]
Pressure Sensor	Change in electrical/mechanical properties with applied strain.[73]	• Tunable mechanical resonance • Chemical reactions and phase transitions[74, 75]

have been demonstrated. Some of the unique physical properties of graphene such as thickness in atomic scale, very high carrier mobility and long spin relaxation time also make it ideally suited for magnetic sensor. Graphene magnetic sensor employing Hall geometry has been reported with performance close to already established 2-dimensional electron gas (2DEG) based sensors.[76] The sensitivity of this sensor can also be varied over a wide range by applying back gate bias.[71]

Graphene spin capacitor,[69] and sensor devices with nanoconstriction[77] have also been realized. Pressure sensors from exfoliated[78] and CVD graphene,[79] Silicon Nitride/graphene,[80] epoxy/graphene,[81] Boron Nitride/Graphene[82] have been demonstrated. Also, graphene based charge sensor has been reported where a twin quantum dot (QD) structure in which the larger QD serves as a single electron transistor to read out the charge state of the nearby gate controlled small QD[83] and, real time radiation dosimeter where electrodes are based on graphene.[84] Table 3.2 summarizes the graphene based physical sensors, their sensing mechanism and applications.

3.2.2   Chemical and Biological Sensors

As discussed before, the unique material properties of graphene make it very promising material for chemical and bio molecular sensing applications, where the adsorbed molecules on graphene surface can strongly affect its physical properties, including conductivity[24] and surface work function (SWF).[85, 86] Demonstration of its ultra-high sensitivity, down to a single gas molecule,[24] confirmed its potential application in molecular detection based on changes in conductance,[24, 85] SWF,[85] frequency of the surface acoustic waves,[87] and low frequency noise.[88] A vast majority of the graphene based sensors reported so far are in the form of chemiresistor or chemical field effect

transistors (chem-FETs) where the surface adsorbed molecules or biological species, either adsorbed directly or through receptors, proportionally change the charge carrier density in graphene causing its conductivity to vary linearly with the number of adsorbed molecules. Table 3.3 enlists some of chemical and biological sensor of graphene, their transduction mechanism and analytes being sensed.

Table 3.3 Graphene based chemical and biological sensors

Sensor Type	Physical parameter measured	Analytes/applications
Gas and vapor sensors	• Conductivity[24] • Surface work function[85, 89] • Surface acoustic wave frequency[87] • Low frequency noise[88]	NO_2, NH_3, H_2, etc.[24, 34, 63, 90]
pH sensors	Change in doping with pH	Protein i.e. bovine serum albumin[91]
Heavy metal sensors	Change in doping with metal particle attachment[92]	Mercury(II) (Hg2+)[92]
H_2O_2 sensor	Current change (Cyclic voltammetry)	Nitrite ($NO2^-$)[93]
Glucose sensor	Current change (Cyclic voltammetry)	Electrochemical biosensors to investigate the enzyme-catalyzed reactions in biological systems[94]
Nucleic acid sensor	Current change (Cyclic voltammetry)	Electrochemical detection of nucleobases, nucleotides, and DNAs[95]
Sensor for cancer protein marker	Current change (Cyclic voltammetry)	Sensor to detect prostate-specific antigen the marker for prostate cancer[96]

3.3 Gas Sensing

Sensing chemical species in gaseous or vapor form in trace amount is very important in various walks of life. Figure 3.1 illustrates some of these area where chemical sensing in parts per million (ppm) or even lower concentration is routinely needed. In particular the monitoring of air quality for various pollutants coming from different sources

such as automotive emission exhaust, industrial pollutants such as NO_x, CO, CO_2, SO_2, chlorofluorocarbons etc. are very detrimental. These pollutant could be toxic, can cause global warming, smog or acid rain, all of which are detrimental to all form of life and can have negative long term effect on the environment. Sensing various volatile organic components (VOCs) in trace amount [97, 98] is very critical to diagnostic applications in
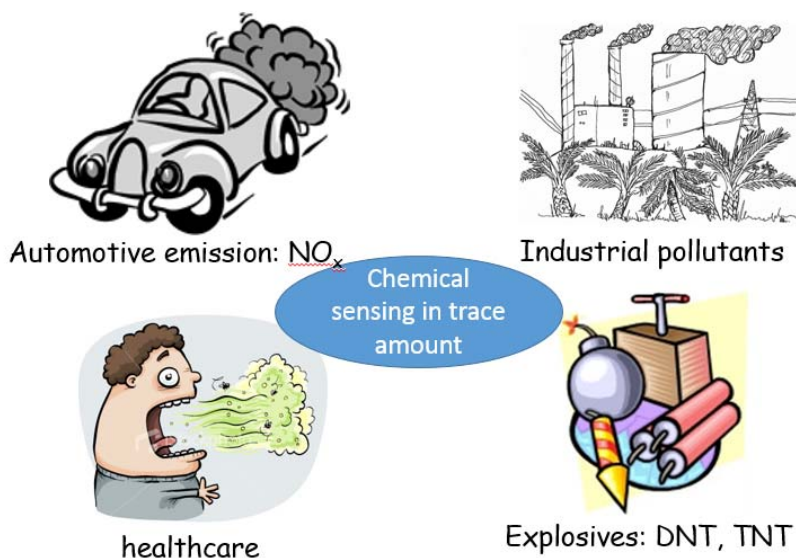
Figure 3.1 Chemical sensing in trace amount (ppm or sub ppm level) is very import in monitoring various pollutants, diagnostic applications in healthcare and in threat detection by sensing molecules such DNT, TNT etc.

healthcare by analyzing the exhaled breath of a patient. Detecting chemical warfare agents and explosives is critical to homeland security. Some of these agents such as nerve agents (Sarin, Soman), mustard gas and explosives (DNT, TNT etc.) are need to be sensed in trace amount as well.

There are a range of available gas sensing technologies. Amongst them mass spectroscopy and gas chromatography techniques are very sensitive and selective to detect particular gases. However the existing systems are bulky, heavy, and are very expensive for many applications. Even the portable counterparts of these gas sensing units are of the

size of a small suitcase. These equipment also require appropriate training for proper operation. The other existing technology which offer more portable unit generally relies upon the sensing gas to modify electrical characteristics of the sensing materials as a transduction mechanism. The most popular of this technology uses metal oxide
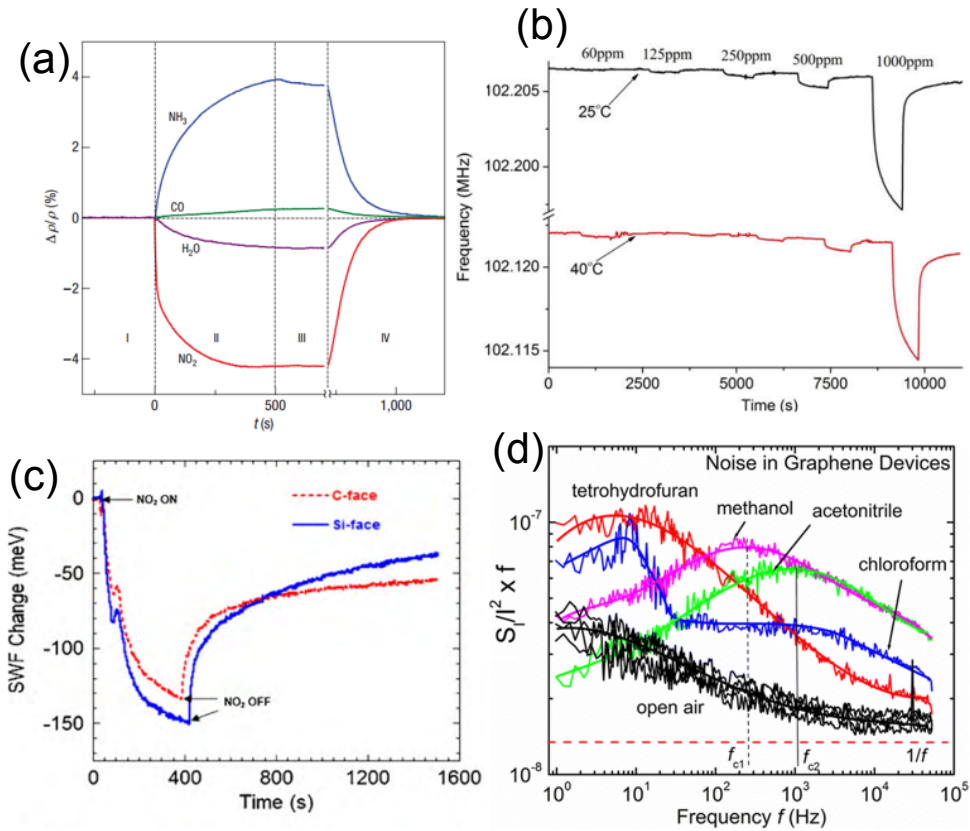
Figure 3.2 Reported sensing modalities of graphene based gas and vapor sensors. Change in (a) conductivity by NO_2, NH_3 and H_2O [24], (b) frequency of SAW by CO [99], (c) SWF by NO_2 [85], and (d) unique 1/f noise spectrum of VOCs [88].

semiconductors such as In_2O_3, SnO_2, ZnO, and WO_3. While metal oxide semiconductor technology is smaller in size and can operate with reduced power compared to mass spectroscopy and gas chromatography, they still cannot be integration with standard silicon or CMOS fabrication. This integration issue results from their relatively high temperature of operation of about 300 °C to 500 °C range, which interferes with the operation of the
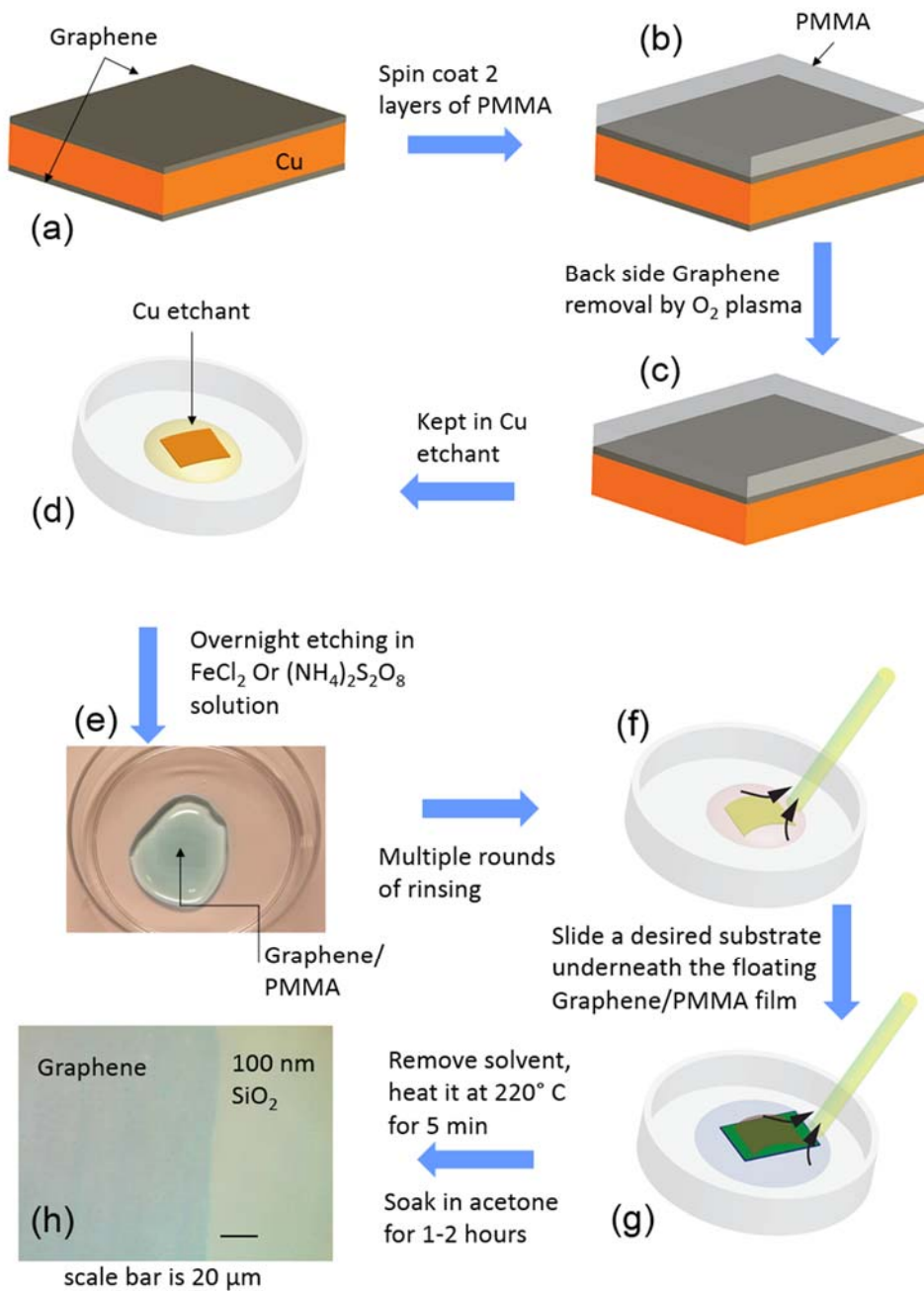
Figure 3.3 Processing steps for graphene transfer on any desirable substrate.

standard Si-based CMOS devices and circuitry. Portable units utilizing these technologies are generally the size of a walky-talky. Furthermore, the power at which they operate

(300mW to 800mW) is still much higher than is desirable for many portable applications. Another drawback these metal oxide suffer is a strong dependence of their critical sensing parameters on growth methods and process conditions.

In recent past graphene has generated huge research interest in developing chemical sensors due to various attractive material properties as discussed in introduction of this chapter. Different transduction mechanism have been proposed and demonstrated the versatility of graphene based gas and vapor sensors such as change in conductivity,[24] frequency of SAW,[99] SWF,[85] and 1/f noise spectrum[88] as shown in Figure 3.2. Amongst these the widely employed transduction mechanism of conductivity change has been investigated in this chapter along with some preliminary results for SWF. The objective of the investigation has been the demonstration of tunability of sensitivity which can lead to selectivity on CVD graphene based back-gated FET devices. The device processing was developed which involved the development of graphene transfer process as well.

3.4   Sensor Fabrication

Conductivity and SWF based sensing modality of graphene gas sensors have been studied in this chapter. While SWF requires a capacitive structure using as-grown graphene as one plate of a capacitor which obviate the need for any device fabrication, whereas conductivity based sensors required full-fledged development graphene FETs. The first step in making any CVD graphene device is transfer of graphene on a desirable substrate.

3.4.1   Graphene Transfer

In CVD based graphene growth on transition metal catalyst, the grown graphene cannot be used directly since it sits on top of a metal film or foil. It is required to be
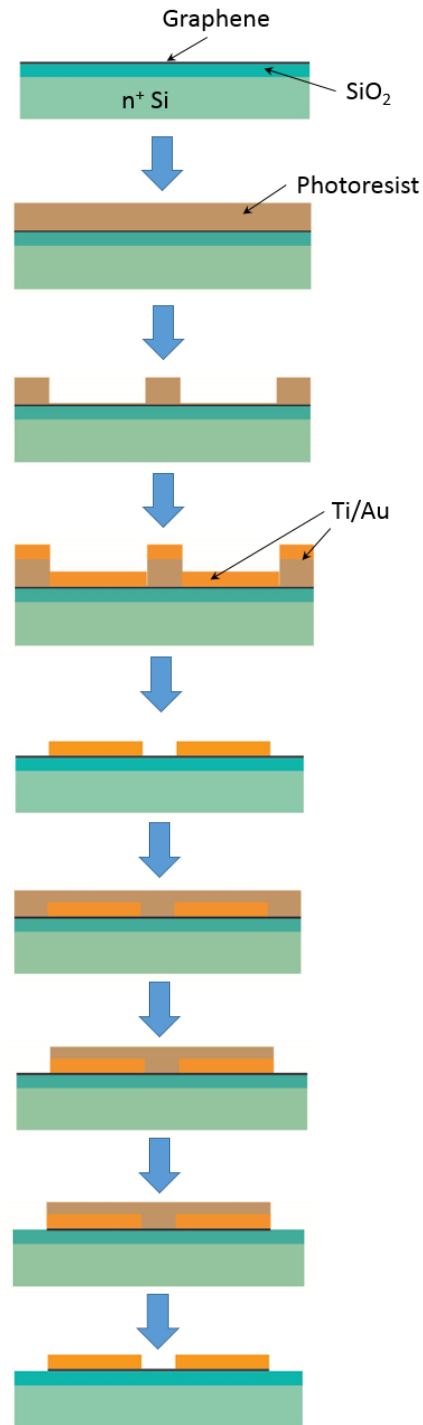
Figure 3.4 Device processing steps for fabrication of graphene FET which will serve as chem-FET.

transferred on a desired substrate for all possible characterization and device making. In

our graphene growth on Cu foil it grows on both sides of the foil. In general graphene grown on the bottom side of the foil is of inferior quality as compared to the one gown on the top side. The graphene transfer process therefore entails the following steps as illustrated in Figure 3.3. The top side graphene is first protected by spin coating of poly methyl methacrylate (PMMA) twice at 3000 rpm for 40 sec. It also provides mechanical strength to graphene in the subsequent processing steps. The PMMA coated sample is loaded upside down in reactive ion etching (RIE) chamber upside down in order to expose the bottom graphene layer. This graphene layer is remover by oxygen plasma which is sustain at 150 W for 180 sec. The sample is then kept in concentrated Cu etchant over night for complete removal of Cu. Both $FeCl_3$ and $(NH_4)_2S_2O_8$ (ammonium persulfate) have been used. This results in graphene/PMMA layer floating in the etchant as seen in Figure 3.3(e). The poor contrast in ammonium persulfate solution is the results of monolayer graphene coated with PMMA. The floated graphene is rinses multiple times in deionized water. A desired substrate can then be slid underneath the floating graphene/PMMA as shown in Figure 3.3(g). The substrate containing transferred graphene/PMMA is allowed to dry in air and then baked at 220 ˚C above the glass transition temperature of PMMA to allow reflow of PMMA in order to heal the wrinkles in graphene. The sample is then dipped in acetone for 2-3 hours to remove PMMA from top of transferred graphene. This is followed by organic cleaning of the sample in acetone and IPA. One such transferred graphene on 100 nm thick SiO_2 is shown in Figure 3.3(h).

3.4.2   *Graphene chem-FET Fabrication*

For making graphene based FETs we chose 100 nm SiO_2/Si substrate. The Si was to be served as global back-gate therefore had low resistivity in the range of 0.008–0.02 Ω-

cm. The graphene was transferred on top of 100 nm SiO$_2$ using process described in previous section. The graphene was then coated with photoresist and conventional lithography was performed to define pattern on resist. Oxygen plasma was used to define pattern on graphene. The resist was then removed in acetone. The patterned graphene was
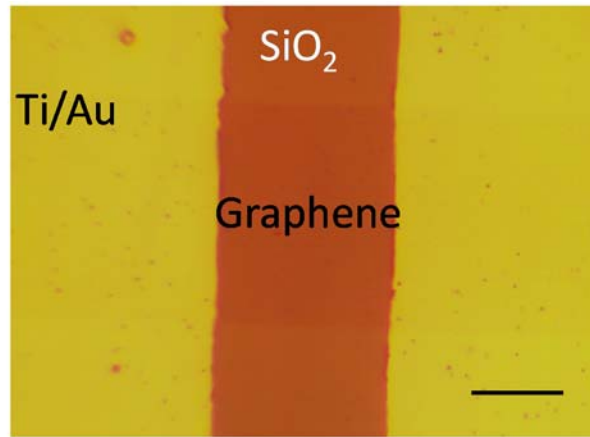
Figure 3.5 Optical micrograph of graphene chem-FET showing 20 μm long and 30 μm wide graphene channel on top of 300 nm SiO$_2$ substrate. The scale bar is 10 μm.

again coated with photoresist for second round of lithography to make contacts on graphene. The patterns for metal contacts were made using lithography as before. 20 nm of Ti and 80 nm of Au were evaporated in e-beam evaporator. The contacts were finally formed using metal lift-off in acetone. A finished device is shown in Figure 3.5 where graphene channel is formed on top of 300 nm thick SiO$_2$ in between Ti/Au source drain electrodes. Figure 3.4 describes these steps schematically.

3.5 Electrical Characterization of Graphene Devices

The sensing response based upon conductivity or resistivity changes would depend upon material and electrical properties and that of electrical contacts. The properties are evaluated through various test structures such as transmission line method (TLM) pads and

Van der Pauw Hall bars etc. It would also be required to evaluate the performance FETs

for the sensing applications.

3.5.1 TLM Characterization

The semiconductor resistance is defined by sheet resistance R_{sh}. The interaction of

semiconductor or semimetal (for example graphene) with metal contacts is characterized

by contact resistance, R_c (Ω) and specific contact resistivity, ρ_c ($\Omega\text{-cm}^2$). We want lower

values of R_c and ρ_c for better ohmic contact behavior. TLM pads are very simple test

structure that lets us measure these parameters for metal semiconductor contacts as shown
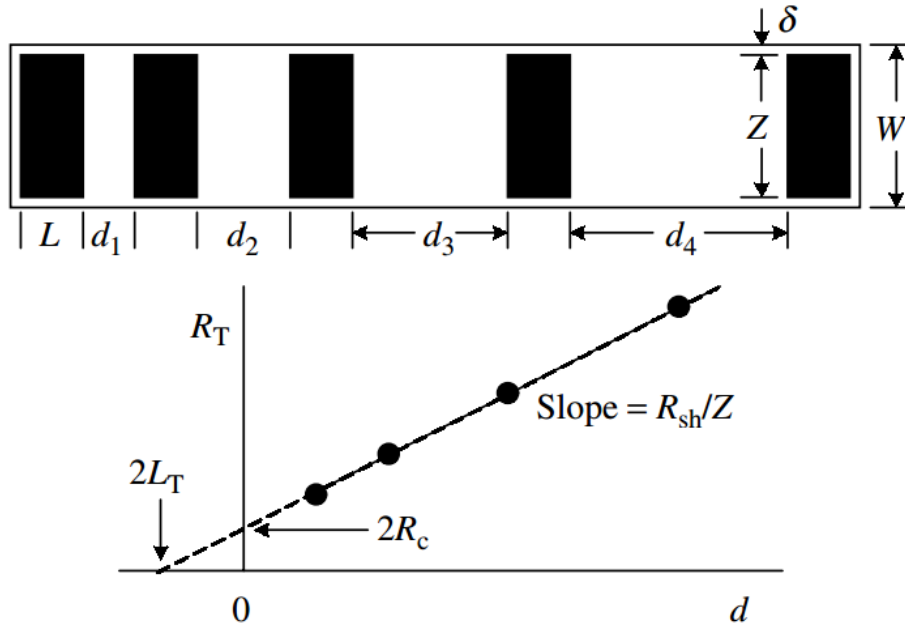
Figure 3.6 Schematic of TLM pads with various geometrical parameters. A plot of
total resistance across two pads from IV measurements as a function of pad spacing
d shows how to extract sheet and contact resistance [39].

in Figure 3.6.[39] The specific contact resistance, ρ_c, is independent of contact area,

therefore becomes important term for comparing ohmic contacts of different sizes. When

the current flows from the channel (material under investigation) to metal contact, it

encounter resistances such as ρ_c and R_{sh} as described in Figure 3.7[39] and goes through the
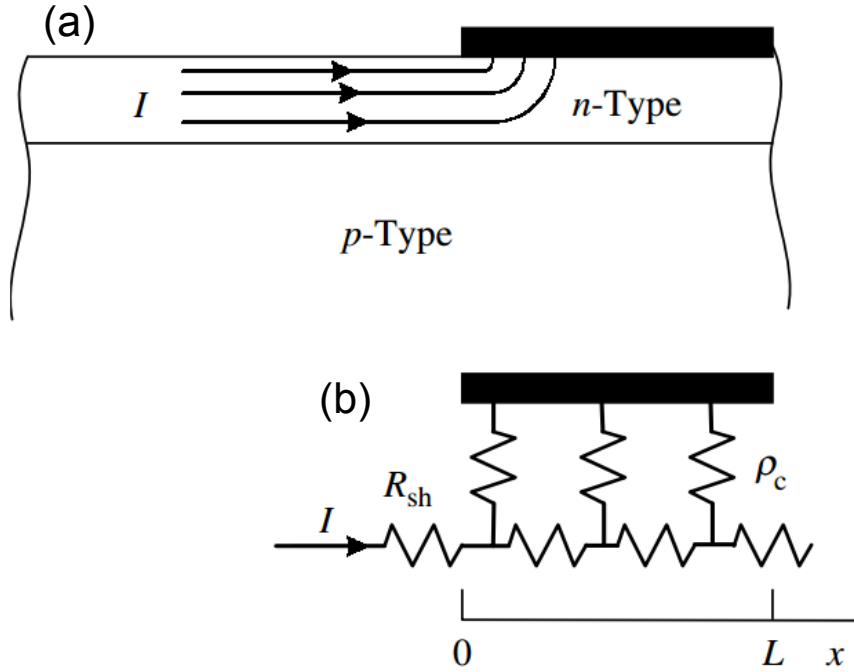
Figure 3.7 The current flow from material to metal contact which follows the path of least resistance. The equivalent circuit shown in terms of ρ_c and R_{sh} [39].

path of least resistance. The potential distribution on contact is determined by both ρ_c and R_{sh}. It is highest at the contact edge and drops exponentially away from the edge. The distance over which the voltage drops to $1/e$ times is called transfer length L_T and is given by the following expression.

$$L_T = \sqrt{\rho_c/R_{sh}} \qquad (3.1)$$

The transfer length can be considered as the distance over which most of the current transfer from material to metal contact or vice versa. Typical values for contact resistance are considered to be $\rho_c \leq 10^{-6}$ Ωcm^2 and transfer length in the order of 1 μm for such contacts. To determine these parameters for graphene, 200 μm × 200 μm wide 20nm Ti/80 nm Au pads with varying separation. Figure 3.8(a) shows TLM characterization on device for which no annealing was performed. The sheet resistance, R_{sh} was computed to be

834.1$\Omega/\square$. The L_T was ~3 µm and R_c was 26.6 Ω. The specific contact resistivity, ρ_c was computed from R_{sh} and L_T using Equation 3.1 and was obtained as 2.75×10^{-4} Ωcm^2. This value of ρ_c is on high side but matches well with reported values of contacts on graphene.
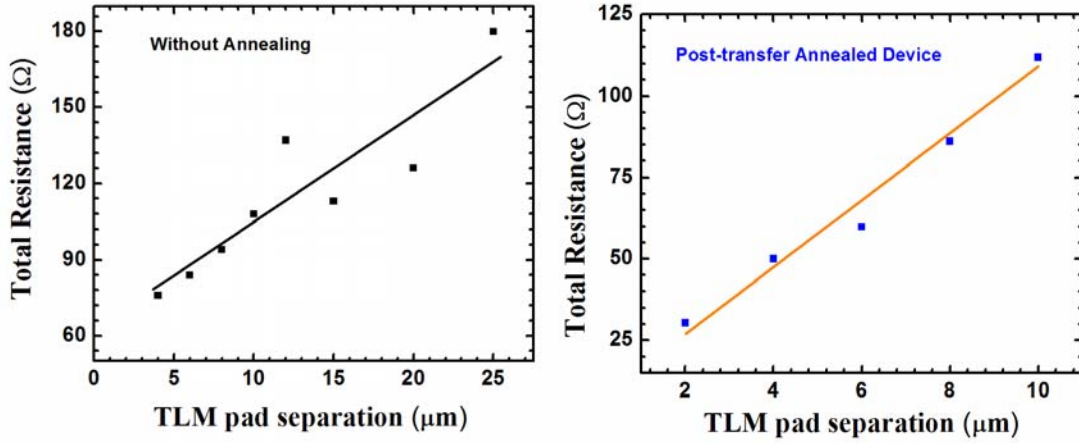
Figure 3.8 TLM measurement on 200 µm × 200 µm wide Ti/Au on graphene. (a) Metal pads deposited with annealing at any stage. (b) The annealing in forming after graphene transfer on SiO$_2$ substrate. The metal contacts were deposited after annealing.

There is a possibility of trapped moistures and PMMA particles and other impurities trapped during the graphene transfer process may cause ρ_c to become higher. To investigate this point further a new set of TLM pads were fabricated. This time the samples were annealed in forming gas environment for 90 minutes at 400 °C. The forming gas was obtained by flowing UHP Ar and H$_2$ at a flow rate of 800 and 200 sccm respectively. The TLM measurements performed on one such sample is shown in Figure 3.8(b). The R_{sh} obtained on these annealed devices was 1972 $\Omega/\square$ which is more than double for the value of graphene that was not annealed. The higher resistance values of graphene could be attributed to higher defect density in the as-grown graphene or it could result from annealing process. The L_T was obtained as ~0.4 µm which resulted ρ_c of 2.8×10^{-6} Ωcm^2. The R_c was found to be 3.8 Ω. These low values of contact resistance and ρ_c are quite

impressive and highlights the importance of annealing in transferred CVD graphene for device fabrication.

3.5.2 Graphene Field Effect Transistor

The current-voltage measurements were performed using a Keithly 2612A System Source Meter unit. Figure 3.9(a) illustrates the schematic of global back-gated graphene
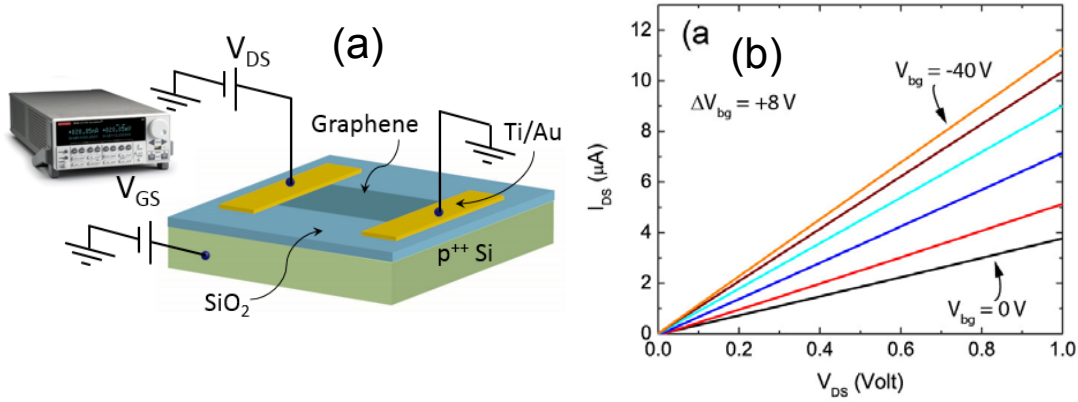
Figure 3.9 (a) Family of curves for graphene chem-FET showing increase in I_{DS} with more negative V_{bg} indicating p-type behavior. (b) I_{DS}-V_{bg} transfer characteristics of the chem-FET with Dirac point at 12 V, indicating p-type behavior of graphene transferred on SiO_2.

FET and the biasing scheme for the measurement of transistor characteristics. In Figure 3.9(b) I_{DS} vs V_{DS} family of curves is shown where back-gate bias V_{bg} varied from -40 to 0 volt with an increment of ΔV_{bg} of 8V. The V_{DS} was varies from 0 to 1V. This shows p-type behavior of transferred graphene in negative V_{bg} range. The more accurate picture of carrier types emerges from transfer characteristics of graphene FET (Figure 3.10)[100] which is also referred as chem-FET for its chemical sensing abilities will be discussed later in the chapter. The I_{DS} vs. V_{bg} plot is ambipolar in nature which is a direct consequence of liner dispersion relation in graphene with zero band gap. The minimum conductivity point in transfer characteristics, also referred as Dirac point, was observed at V_{bg} of 12 V. The

positive Dirac point reaffirms that CVD graphene transferred on SiO_2 is p-type in nature. Another important information about material property that can be obtained from transfer characteristics of this device is field-effect mobility, μ_{FET}, given by the following
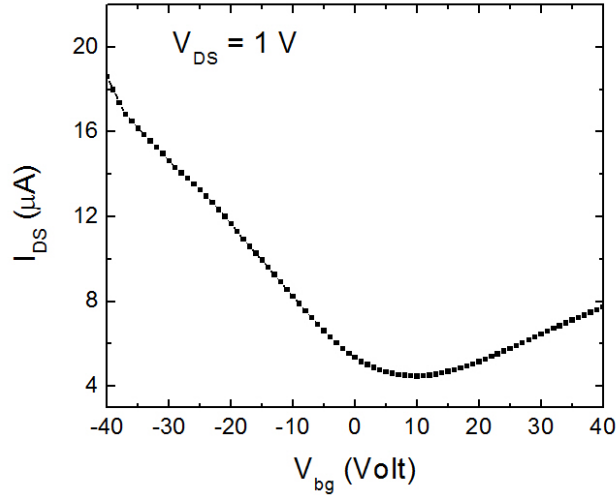
Figure 3.10 I_{DS}-V_{bg} transfer characteristics of the chem-FET with Dirac point at 12 V, indicating p-type behavior of graphene transferred on SiO_2.

expression.

$$\mu_{FET} = g_m \, L/W \, C_{ox} \, V_{DS} \qquad (3.2)$$

Where g_m is transconductance, L is length of graphene channel, W is width of the graphene channel, C_{ox} is the oxide capacitance per unit area. With improvement in the quality of the graphene film we were able to obtain mobility values in the range of 1000 cm^2/Vs on routine basis. Our best μ_{FET} was calculated as 3424 cm^2/Vs. Figure 3.11 shows a bar chart illustrating variation of mobility at different places. These variation may result

Table 3.4 Statistics of mobility values in cm^2/Vs for FETs on a single chip

Number	Mean	Standard deviation	Minimum	Median	Maximum
11	1236.9	903.6	349.7	971.9	3424.6

from already exiting non-uniform defect density in CVD graphene or can be introduced during the processing as well. Table 3.4 enlists the statistics of 11 graphene FETs device for which mobility was calculated from transfer characteristics. Although a large standard
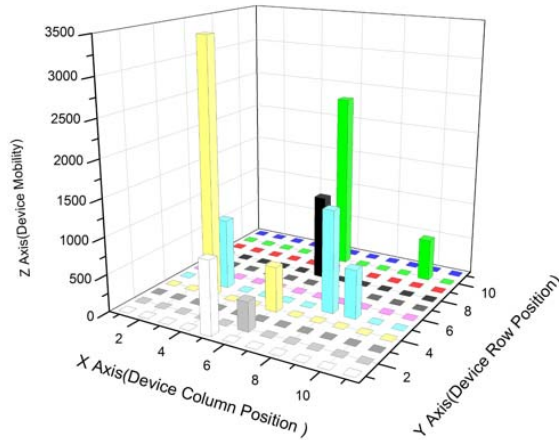
Figure 3.11 The variation of at different location suggest different defect density of graphene at different location

deviation of ~900 cm^2/Vs exist amongst these devices the mean value of 1236 cm^2/Vs is fairly impressive. The minimum value of 349.7 cm^2/Vs is also much improved from the mobility values obtain from the devices in the early phase of CVD optimization for this project.

3.5.3 Hall Measurements

It is a method of determining transport properties of a material such as resistivity, carrier density and mobility. It is based upon Hall Effect in which a magnetic field is applied perpendicular to a slab of material which carries a current across it as described in Figure 3.12 for a bridge-type Hall bar made of graphene. A constant current is flowed along the longitudinal axis of the Hall bar. Due to application of magnetic files charge carrier feels a Lorentz force and drift away from the direction of current to perpendicular direction. This charge separation creates a potential difference across the electrodes perpendicular to
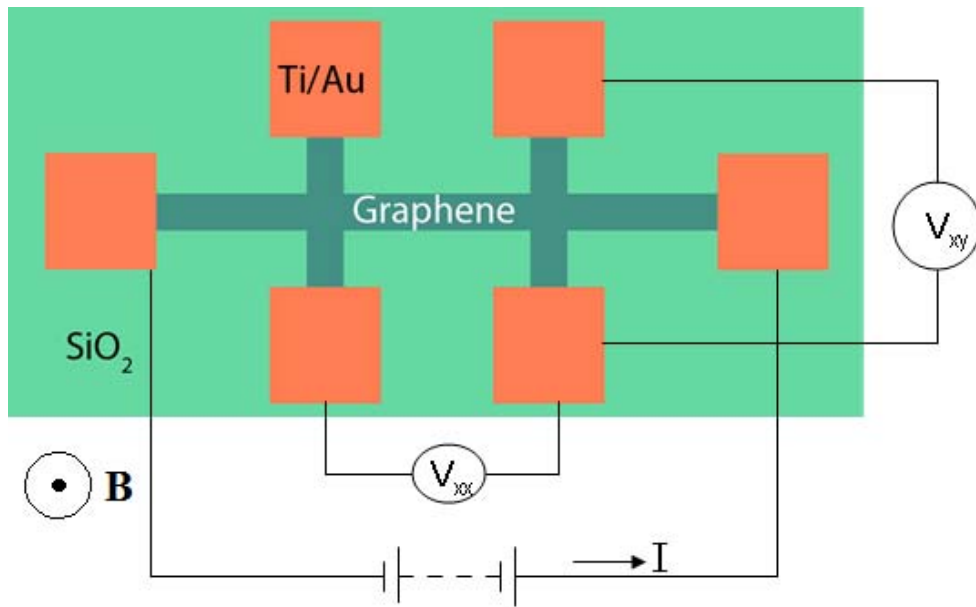
Figure 3.12 Schematic of the bridge-type graphene Hall bar along with schematic of the Hall measurement, where **B** is applied perpendicular to the plane of the paper and Hall voltage V_{xy} is measure across the electrodes shown.

the current flow which can be measured as V_{xy}, as shown in Figure 3.12, also called as Hall

voltage. To determine the transport properties of the transferred graphene films, Hall bar
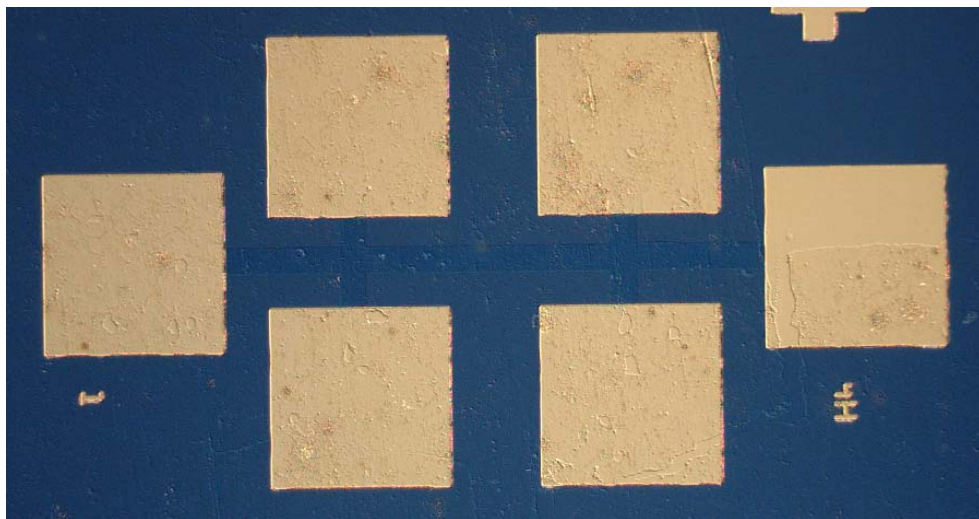
Figure 3.13 Bridge-type graphene Hall bar with 20 μm wide graphene channel fabricated by optical lithography using chrome mask and mask aligner.

patterns were etched and metal contacts were deposited on the transferred graphene film using chrome mask as shown in Figure 3.13. Hall bar with graphene film of 20 µm channel width was patterned (darker blue contrast). Typical four terminal method is used in these experiment, and the experimental bias connections for the measurement of resistance and mobility are shown schematically in Figure 3.12. A constant dc current was applied through
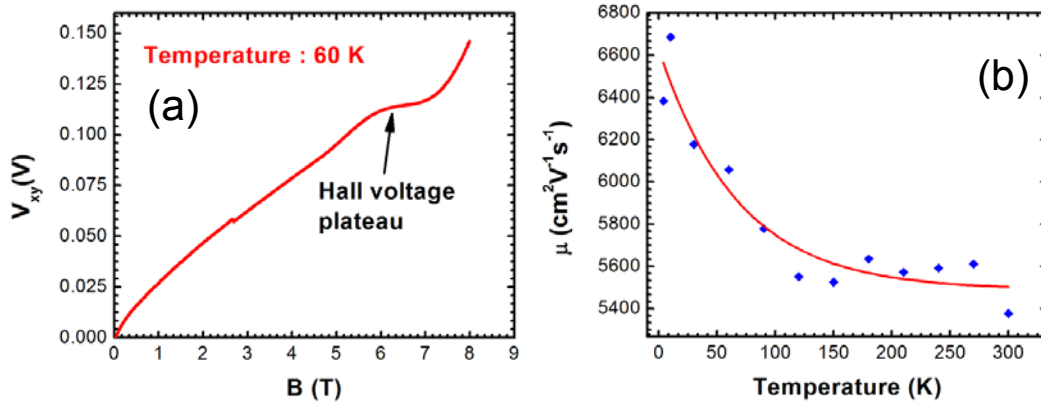
Figure 3.14 (a). Hall voltage V_{xy} at T = 60 K from a graphene Hall bar sample showing the quantum Hall effect. The plateau of V_{xy} is shown by an arrow. (b) Temperature dependence of carrier mobility µ from the sample which showed the quantum hall effect. The red line is the exponential decay fitting.

the devices and the voltages V_{xx} and V_{xy} were measured across the terminals with a magnetic field B varied up to 8 Tesla in perpendicular direction. Out of several devices measured so far a majority showed the normal Hall Effect, where the Hall Voltage kept increasing with the magnetic field. However, for one device, Hall voltage V_{xy} from one device showed a plateau such as in the quantum hall effect when it is cooled down to 60 Kelvin, as shown in Figure 3.14(a). This is a very exciting result and clearly conforms the quality of graphene film synthesized. The value of the plateau fits in the equation

$$V_{xy} = Ih/(4n + 2)e^2 \qquad (3.3)$$

with n = 5, where n is the Laudau-level index. The charge carrier densities and charge carrier mobility values were derived from the hall bar measurement. The charge carrier density of p $\sim 10^{12}$ cm^{-2} and mobility at room temperature of $\mu \sim 1000$ cm^2/Vs were found
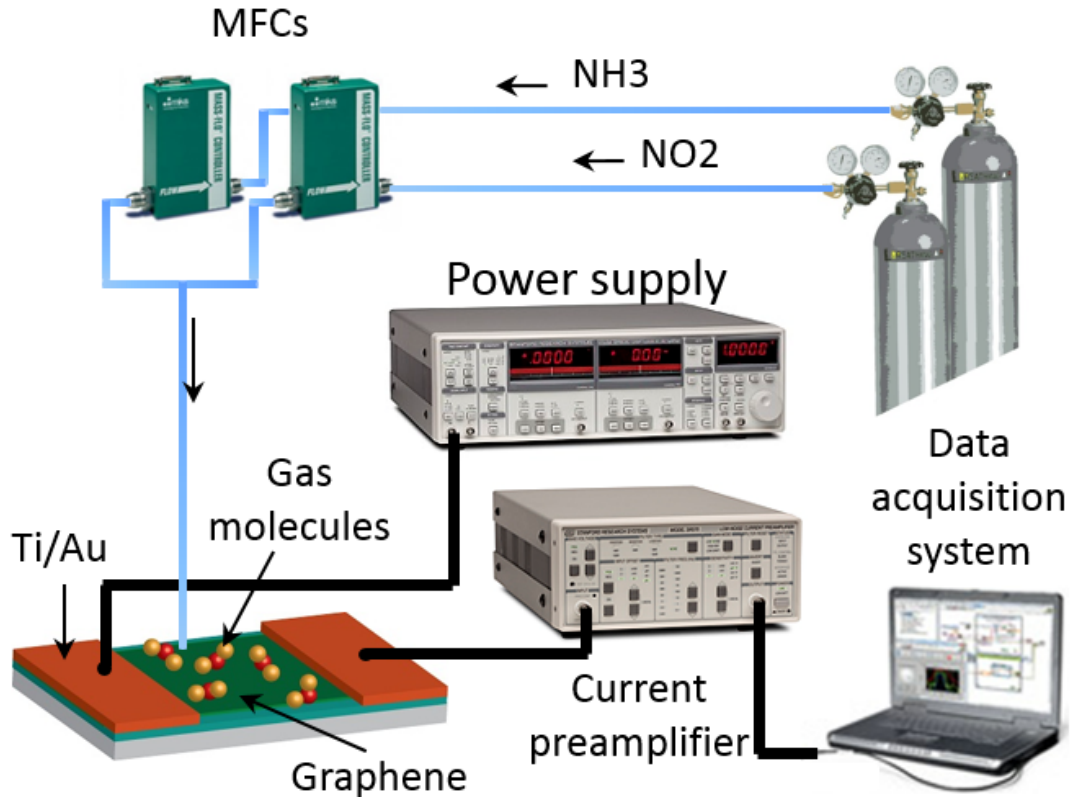
Figure 3.15 Schematic of amperometric measurement set up for chemical sensing where calibrated test gases (20 ppm NO_2, 550 ppm NH_3) are delivered to sensor under test. The current as a function of time is measure by current preamp and recorded by data acquisition system.

for most of the devices. However, the device which showed the quantum hall effect had the mobility as high as 5400 cm^2/Vs at room temperature and 6600 cm^2/Vs at T=l0 K, as shown in Figure 3.14(b). An exponential decay function can fit the temperature dependence of carrier mobility μ.

3.6 Sensing Response of Graphene Chem-FETs

The sensing measurements of graphene chem-FETs were carried out using two different gases, NO_2 and NH_3, which behave as electron acceptor and donor,[101] respectively. The test bench consisted of a customized probe station in AFM set-up. The schematic of sensing set-up is illustrated in Figure 3.15. In this technique a voltage bias in the range of 50 to 100 mV is applied to the device by a lock-in amplifier SR830. The current is fed to a current preamplifier SR570. The output in the form of voltage as time function is read and plotted by a data acquisition system. Test gases such as NO_2 is allowed to flow at the rate of 500 sccm, using MFCs, on the device after a delay of 60 sec of bias tuned on (Figure 3.16(a)).The test gas molecules are then adsorbed on the graphene and modify its conductivity. The process of adsorption of a molecule on a surface could be

Table 3.5 Salient distinguishable features of chemisorption and physisorption[102]

Chemisorption	Physisorption
Charger carrier exchanged in involved	Polarization between adsorbate and surface
Chemical bond formation	van der Waals forces are involved
Stronger interaction, ($\geq$ 1eV)	Weaker interaction, ($\leq$ 0.3 eV), therefore stable only at cryogenic temperatures
highly corrugated potential analogies with coordination chemistry	less strongly directional

broadly of two types, physisorption or chemisorption based upon the interaction between the adsorbing surface and adsorbate (gas molecule). In chemisorption chemical bond formation is involved between adsorbate and the surface whereas weaker interaction such as polarization is involved in physisorption as compared to charge transfer between

them.[102] The distinction between physisorption and chemisorption becomes difficult due to existence of almost continuous spectrum of interaction strength. However it is possible to a broader distinction between them based upon their salient features listed in Table 3.5.

Like chemical bond chemisorption is highly directional; and adsorbates stick at specific sites therefore binding interaction is strongly dependent upon exact position and orientation of the adsorbates with respect to the surface. This feature of chemisorption have
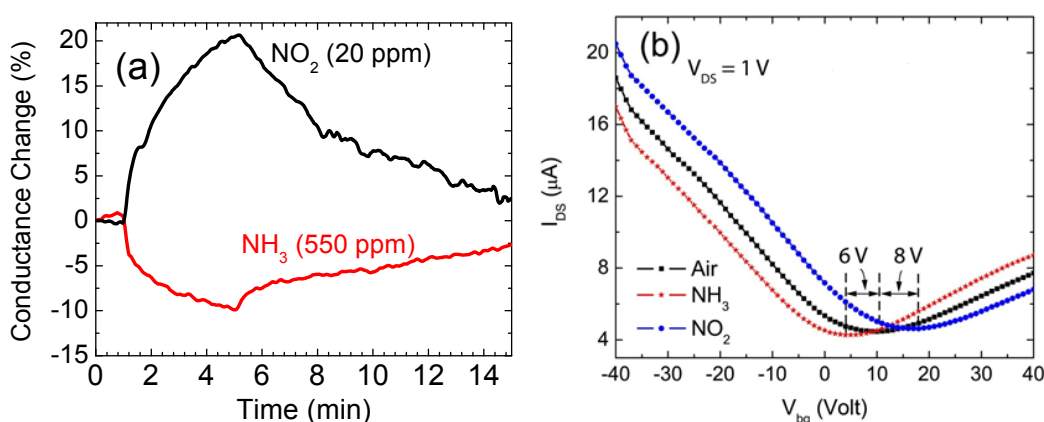
Figure 3.16 (a) Gas sensing response of graphene chem-FET at V_{bg} = 0V towards hole donating NO2 and electron donating NH3 in terms of % conductance change. (b) Transfer characteristics of the chem-FET in air, 20 ppm NO2 and 550 ppm NH3 showing a shift of Dirac point.

implication in chemical sensing in general which may be responsible for different rates of current or conductivity change in graphene based sensors upon exposure, and withdrawal of exposure of analytes to graphene surface. On metal surface the chemisorbed atoms tends to attach to the sites offering highest coordination. For example in Pt (111) surface O tends to sit at FCC three fold hollow sites with bond energy of ~370kJ mol^{-1}.[103] Since defects in general tends to offer more coordination or binding sites therefore defective graphene are observed to have better sensing response to analytes as noted in this dissertation as well.

In physisorption, adsorbates do not experience strong directional interactions. Therefore, they bond more weakly to specific sites and experience an attractive interaction with the surface that is much more uniform across the surface. In many cases, the interactions between physisorbates are even stronger than the interaction with the surface, however in some cases strong chemical attraction from the surface may cause physisorbed species to become chemisorbed which could be a possibility for NO_2 or NH_3 adsorption on graphene.

Irrespective of actual initial mechanism of adsorption the charge exchange between graphene and adsorbed molecules, a clear sign of chemisorption, causes the conductivity of graphene to change upon exposure of NO_2 or NH_3 molecules. This results in a change in current and is recoded as a function of time. It is very important to highlight here that all these measurements are carried under ambient conditions to assess the possibility of making practical sensors using graphene.

Sensitivity of a chem-FET is defined as percentage conductance change caused by the flow of the test gas, and calculate as $100 \times (I_g - I_0)/I_0$, where I_0 is the base current in absence of the test gas, and I_g is the current in presence of the gas at the given exposure time. Figure. 3.15(a) compares the percentage conductance change (as a function of time) for the two gases as their flow is turned on and then off. We found that upon exposure to 20 ppm NO_2 for 2 minutes, the conductance increased by 21%, while with 550 ppm NH_3 exposure the conductance decreased by 10%. This behavior is expected, since NO_2 being an electron acceptor, would increase the density of holes in graphene following adsorption, and increase in the conductivity of a p-type graphene. On the other hand, NH_3 being an electron donor would decrease the density of holes, and hence decrease the conductivity.

Notably, the change in conductivity due to NH_3 adsorption is much less than that due to NO_2, in spite of higher concentration of the former, which can be attributed to lower charge (0.03q) transfer per molecule from NH_3 molecules to graphene compared to 0.3 q per molecule of NO_2.[101]

To determine the extent of charge density modulation due to molecular doping by NH_3 and NO_2, we measured the I_{DS}-V_{bg} characteristics of the device prior to gas exposure and compared that to the plots after NO_2 and NH_3 exposure as shown in Figure 3.16(b). The transconductance g_m calculated from Figure 3.16(b) at V_{DS} = 1 V was 0.35 μS. Utilizing this in the formula for field effect mobility μ_{FET}:

$$\mu_{FET} = \frac{g_m L}{W\, C_{ox} V_{ds}} \qquad (3.4)$$

The mobility was calculated as 10.15 cm^2/Vs. The carrier density was then computed from the formula,

$$p = \sigma t/q\mu = GL/(q\mu W) \qquad (3.5)$$

and at zero gate bias came out to be 3.35×10^{12} cm^{-2}, where G is the conductance of the graphene film. Although the mobility seems to be rather low, it actually agrees well with the carrier mobility in CVD graphene films transferred to SiO_2/Si substrates, where it is in the range of 20 – 150 cm^2/Vs.[104, 105] The low mobility of transferred graphene could be attributed to fixed charges trapped at the SiO_2/graphene interface[106] and relatively larger defects in graphene causing more scattering of charge carriers. From Figure 3.16(b) the I_{DS}-V_{bg} curve was found to be shifted to the right by 8 V upon 20 minutes of exposure to NO_2, which indicates further p-type doping due to adsorption of electron withdrawing NO_2 molecules. The same duration of exposure to NH_3 resulted in the I_{DS}-V_g curve shifting to the left by 6 V, which is due to n-type doping caused by the electron donating NH_3

molecules. The change in carrier density due to the molecular doping can be obtained from the adsorption induced shift in transfer characteristics using the equation,[1]

$$\Delta n = \left(\varepsilon\varepsilon_0 \Delta V_{Dirac,gas}\right)/q t_{ox} \quad (3.6)$$

where ε is the dielectric constant of SiO_2 (3.9), ε_0 is the vacuum permittivity, t_{ox} is the oxide thickness (100 nm), q is the electronic charge, and $\Delta V_{Dirac,gas}$ is the change in the Dirac point due to the molecular adsorption. From the shift in Dirac point in the two cases, changes in carrier density can be computed as 1.73×10^{12} and 1.29×10^{12} cm^{-2} for NO_2 and NH_3, respectively. The fractional changes in conductivity (= $\Delta p/p$) for NO_2 and NH_3 for 20 min is computed as 51.6% and 38.5%, which are typically observed for our devices where the 2 minutes exposure resulted in changes of 21 and 10% for NO_2 and NH_3, respectively.

3.7 Sensitivity Tuning in Chem-FETs

The modulation of the Fermi level of graphene by back-gate bias is expected to strongly affect the sensitivity of the chem-FET toward various gas molecules. This concept was systematically investigated in this work by varying the back-gate bias of the graphene chem-FET devices from -45 V to 5V, and recording the sensitivity toward NO_2 and NH_3 at each bias step. The dependence of sensing responses on back gate bias for NO_2 and NH_3 are shown in Figure 3.17(a, b). From Figure 3.17(a) graphene's sensitivity which is defined as percentage conductance change, was found to decreases from 26.1% to 3.6% for 20 ppm NO_2 as V_{bg} changed from 5 to -35V. The opposite trend was observed for NH_3 in Figure 3.17(b) where the sensitivity decreased from 7.6% to 0% as V_{bg} changes from -30 to 5V. There are two factors that can affect the conductivity change due to gaseous adsorption,

$\Delta\sigma$, which is inversely proportional to the initial carrier concentration before adsorption, p_0, and directly proportional to the change in carrier concentration due to gas adsorption, Δp. Since the transferred graphene on SiO_2 is p-type in nature, a positive gate bias would reduce the hole concentration. With fractional change in conductivity, given by the relation

$$\Delta\sigma/\sigma = \Delta p/p \qquad (3.7)$$

an increase in p_0 would certainly reduce the sensitivity toward the adsorbed molecules even if Δp remains constant. It would be interesting if the corresponding movement of the Fermi level, in response to the change in back-gate bias, affects Δp, the charge transfer between the adsorbed molecules and graphene film. To investigate this, Δp
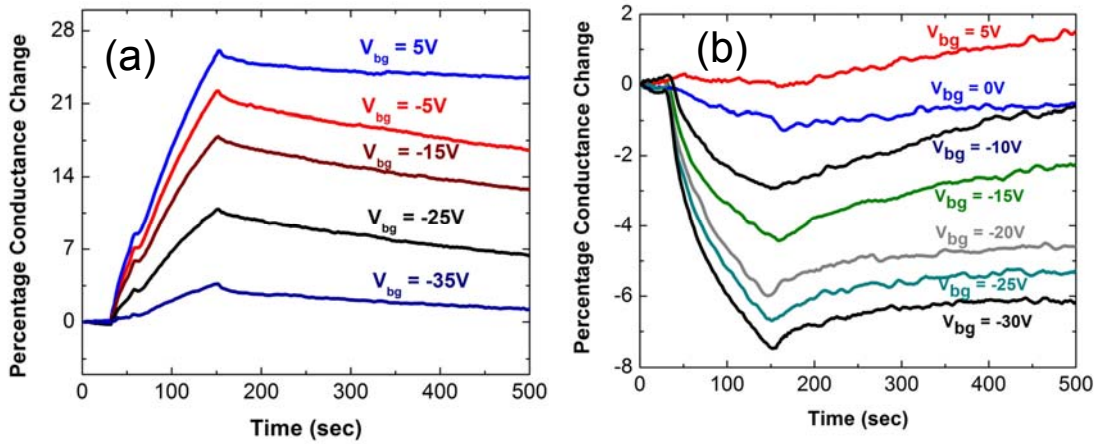
Figure 3.17 Variation of back gated graphene sensor response for (a) 20 ppm NO_2 exposure with the increase in gate bias from negative to positive values and (b) 550 ppm NH_3 exposure with the gate bias change from negative to positive values.

was calculated from the experimentally measured σ and $\Delta\sigma/\sigma$ due to gaseous adsorption at each voltage bias.

For a 30×30 μm device, the initial carrier density, $p[= \sigma t/q\mu = GL/(q\mu W)]$ at $V_{bg} = 5V$ is calculated as $3.16\times10^{12}\,cm^{-2}$, where G is the conductance of the graphene film. The calculated values of carrier concentration at each voltage bias are shown in Table 3.6.

65

For our calculations, we assumed $\mu = 10.15$ cm²/Vs as calculated earlier for this device. The mobility was assumed to remain constant over the back-gate bias range considered (5 to -45 V), as g_m (the slope of I_{DS}-V_{bg} curve) was found to remain fairly constant over that
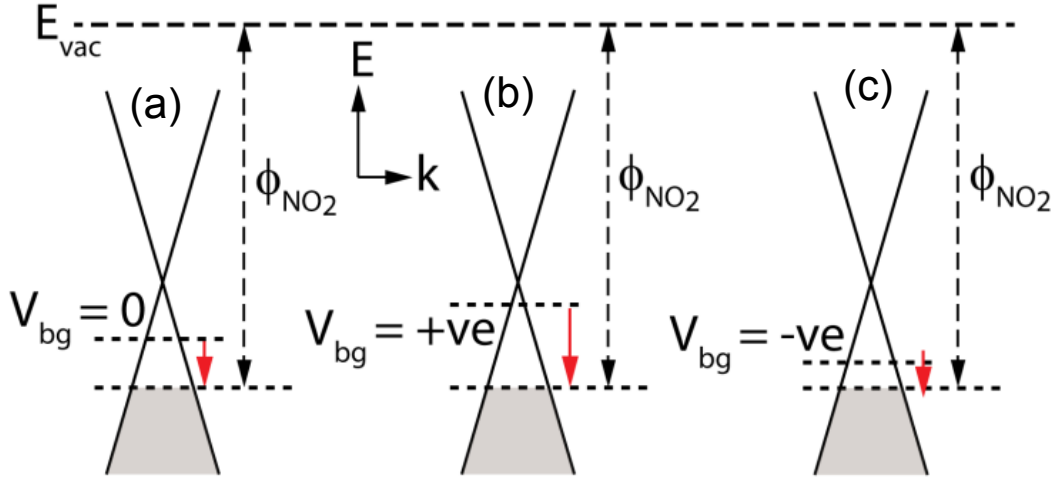
Figure 3.18 Band diagrams showing movement of Fermi level in back gated graphene chem-FET as a result of gate bias and NO₂ adsorption at (a) no bias, (b) positive and, (c) negative gate bias. Fermi level moves downward upon exposure to NO₂ in all 3 cases due to increase in hole concentration.

range in Figure 3.16(b). From Figure 3.17(a) we find that for $V_{bg} = 5$ V, the fractional change in conductivity $\Delta\sigma/\sigma$ due to NO₂ adsorption is 0.261. Utilizing the relation $[\Delta\sigma/\sigma = \Delta p/p]$ and the value of p for that bias from Table 3.6 (column 3), the change in carrier density, Δp_{NO_2} is calculated as 8.25×10^{11} cm⁻². The calculated values of Δp_{NO_2} are summarized in column 4 of Table 3.6, where the charge transfer doping Δp_{NO_2} is found to decrease from 8.25×10^{11} cm⁻² to undetectable as V_{bg} decreases from 5 to -45 V. Following a similar process p and Δp_{NH_3} were calculated for NH₃ adsorption for different V_{bg}, and are shown in Table 3.7. In contrast to NO₂, and affirming its donor like behavior, the charge transfer doping Δp_{NH_3} is found to increase from undetectable to 3.39×10^{11} cm⁻² as V_{bg}

decreases from 5 to -30 V. Since NO_2 forms acceptor states (unoccupied molecular orbitals) below the Dirac point,[107] more negative gate bias would lower the Fermi level and bring it closer to acceptor state energy level, so the magnitude of charge transfer (Δp_{NO_2}) between NO_2 molecules and graphene would reduce. Figure 3.18 shows the band diagrams with acceptor and the Fermi energy levels for different gate biases. Since the charge transfer is a self-limiting process, its rate will also depend on the energy difference between the Fermi level and the acceptor level; hence Δp_{NO_2} corresponding to a given time interval, for instance 120 s in our experiments, will be dependent on V_{bg}, as observed experimentally (Table 3.6). The reverse is observed for electron donor NH_3, which forms donor states above the Dirac point, therefore a change in V_{bg} to more negative values causes the Fermi level to move downward, increasing the energy difference and hence the magnitude and rate of charge transfer doping.

The Fermi level position for each back gate bias can be calculated using the equation,[13]

$$E_F = \sqrt{\pi p (\hbar v_F)^2}, \quad (3.8)$$

where E_F is the Fermi level position relative to the Dirac point. The change in Fermi level due to molecular adsorption $\Delta E_{F,ads}$ $(= E_{F_0} - E_{F_1})$ can also be calculated using:

$$\Delta n_{ads} = \left|\left(E_{F_1}{}^2 - E_{F_0}{}^2\right)\right|/\pi(\hbar v_F)^2 \quad (3.9)$$

and setting $E_{F_0} = 0$, where E_{F_0} and E_{F_1} are the initial and final Fermi levels, respectively, Δn_{ads} is the adsorption induced change in charge carrier density, and v_F is the Fermi velocity of electrons (10^8 cm/s).[108]

Table 3.6. Effect of back gate bias on initial carrier density, Fermi level position, and charge exchange due to flow of NO_2

Back gate bias (V)	Initial Conductance (μS), (change in %)	Initial carrier density, p_o (cm^{-2})	Adsorption induced carrier density change (cm^{-2}), Δp	Fermi level position E_F (meV)	Adsorption induced Fermi level change ΔE_F (meV)
5	5.13 (26.1)	3.16×10^{12}	8.25×10^{11}	207.5	106.0
-5	5.32 (22.2)	3.28×10^{12}	7.28×10^{11}	211.3	99.6
-15	5.88 (17.8)	3.62×10^{12}	6.45×10^{11}	222.2	93.7
-25	7.09 (10.8)	4.37×10^{12}	4.72×10^{11}	243.9	80.2
-35	9.04 (3.6)	5.57×10^{12}	2.00×10^{11}	275.4	52.2
-45	10.87 (0)	6.69×10^{12}	Below detection limit	302.0	Below detection limit

Table 3.7. Effect of back gate bias on initial carrier density, Fermi level position, and charge exchange due to flow of NH_3

Back gate Bias (V)	Initial Conductance (μS), (change in %)	Initial carrier density, p_o (cm^{-2})	Adsorption induced carrier density change (cm^{-2}), Δp	Fermi level position E_F (meV)	Adsorption induced Fermi level change ΔE_F (meV)
-30	7.25 (7.6)	4.46×10^{12}	3.39×10^{11}	246.6	68.0
-25	6.93 (6.76)	4.27×10^{12}	2.88×10^{11}	241.1	62.7
-20	6.54 (6)	4.02×10^{12}	2.41×10^{11}	234.2	57.4
-15	5.93 (4.5)	3.65×10^{12}	1.64×10^{11}	223.0	47.3
-10	5.24 (3)	3.23×10^{11}	9.69×10^{10}	209.7	36.3
0	4.17 (1.36)	2.57×10^{11}	3.49×10^{10}	187.0	21.8
5	4.08 (0)	2.51×10^{11}	Below detection limit	185.0	Below detection limit

The pre-exposure Fermi level and its shift caused by NO_2 and NH_3 molecular doping are also summarized in Tables 3.6 and 3.7. We find for NO_2, as the initial Fermi level moves downward, the change in Fermi level due to adsorption $\Delta E_{F,ads}$ reduces monotonically, as expected from discussions earlier. Furthermore, the combined value of
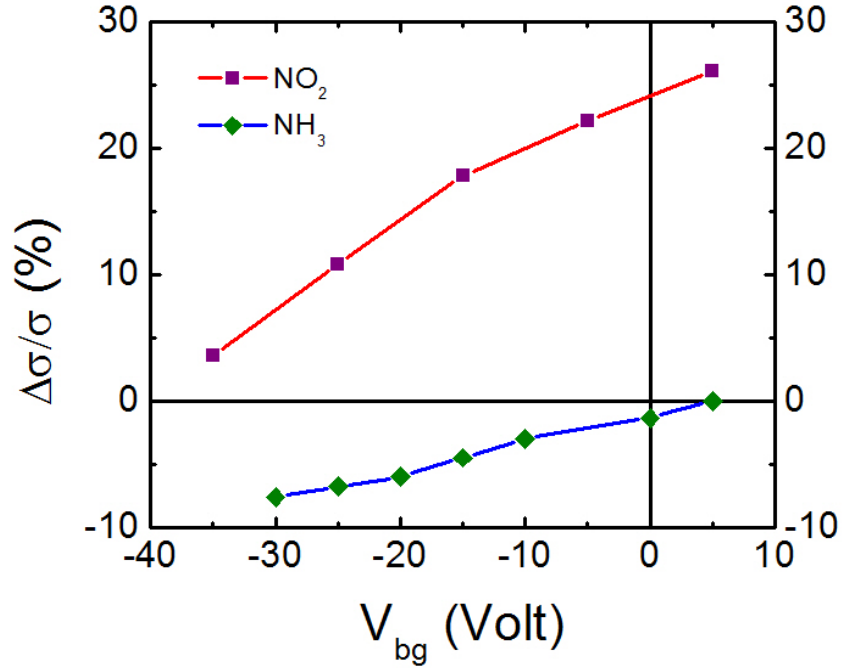
Figure 3.19 Sensitivity response plotted for 20 ppm NO_2 and 550 ppm of NH_3 as a function of V_{bg}. The selective NO_2 detection could be possible at V_{bg} of 5V and selective NH_3 could be had at V_{bg} of -40V.

initial E_F and $\Delta E_{F,ads}$ is ~320 meV at different back-gate biases. From this observation, it can be argued that the acceptor energy level of NO_2 is ~320 meV below the Dirac point. This is in excellent agreement with the reported theoretical and experimental values of NO_2 acceptor energy level of $300 - 400$ meV.[101, 109] For NH_3, the reverse trend is observed, i.e. as the Fermi level moves downward, its change due to adsorption increases. The change in conductivity is undetectable at $V_{bg} = 5$ V, for which the Fermi position is calculated to be

~185 meV below the Dirac point. This is in contrast to earlier reports of NH_3 donor energy level, which is generally expected to be above the Dirac point.[101]

It is interesting to note here that for p-type graphene the carrier concentration change and the Fermi level movement act together to enhance the detection sensitivity for both donor and acceptor type gases. Thus, the sensitivity for gaseous detection for p-type graphene can generally expected to be higher than that of n-type graphene for acceptor type molecules such as NO_2. In addition, it has been demonstrated here for the first time that molecular doping by adsorbed gas molecules depends on the position of the Fermi level relative the donor/acceptor states and it can be tuned by appropriate back gate bias. However, whether the back-gate bias simply affects charge transfer between adsorbed molecules and graphene, or it affects the density of the adsorbed molecules, or a combination of both, needs to be investigated further.

3.8   Selectivity in Graphene Chem-FETs

It could be possible to impart selectivity towards NO_2 and NH_3 in graphene chem-FETs as shown in Figure 3.19. At positive V_{bg} of 5V in the figure, the sensitivity of NH_3 is almost 0% whereas NO_2 response is ~26%. Therefore at 5V back-gate bias the graphene chem-FET will detect NO_2 selectively in a mixture of NO_2 and NH_3. Similarly to have selective NH_3 response the chem-FET should be operated at V_{bg} of ~40 V. In this chapter we saw the effectiveness of graphene chem-FET to show a tunable sensitivity towards polar analytes (NO_2 and NH_3) with possibility of selectivity while operating close to defect level of the analyte in the graphene.

In summary graphene based chem-FETs were fabricated by developing graphene transfer and graphene device processing by photolithography and other techniques. TLM pads and Hall bars were characterized to gauge various parameters for device performance such as mobility, carrier concentration, specific contact resistivity etc. The tuning of sensitivity of chem-FETs was achieved by use of a back-gate bias. However the sensitivity remains fairly low in the range of 50-60 %. In the following chapter the strategy to enhance the sensitivity towards polar molecules and sensing of nonpolar molecules by functionalization will be discussed.

CHAPTER 4

SENSITIVITY MODULATION

In the short span of a decade since its first isolation in year 2004 graphene has shown a great promise as a sensing material. Different sensing methodologies have been demonstrated such as change in conductivity, surface work-function, frequency of surface acoustic waves and 1/f noise spectrum to detect various analyte molecules in very low concentration. Amongst these modality, conductivity appears to be commercially viable modality for chemical sensing. The adsorbed molecules change the conductivity of graphene by charge exchange between them. This change can be readily monitored in time dependent amperometric measurements. The graphene based sensors operating in this mode are termed as chemiresistors. In general graphene chemiresistors suffers from low sensitivity values not exceeding 100% towards ppm level NO_2 and other analytes. In this chapter we will discuss and propose the means to improve sensitivity of graphene based sensors working in amperometric mode.

4.1 Methods of Chemical Sensitivity Modulation

4.1.1 Sensitivity Modulation by Use of a Back-gate Bias

Graphene chem-FETs have been demonstrated to improve sensitivity towards NO_2 and NH_3 as discussed in previous chapter. The use of global back gate modulates carrier concentration and also graphene Fermi level. The sensitivity changes from very low to a

72

value as high as 26% in case of NO_2 as Fermi level moves with different back-gate bias. This is one way to enhance sensitivity, however the sensitivity number remains low since sensitivity is directly proportional to numbers of molecules adsorbed to the graphene surface to dope it. One way to improve the sensitivity number would be to increase the number of adsorbed molecules for a given concentration by increasing the capture site in the graphene.

4.1.2 Sensitivity Modulation by Defects

The sensitivity of graphene based sensors devices are strongly affected by the presence of defects in graphene, which can be in the form of grain boundaries, vacancies or point defects, dopants, wrinkles, change of hybridization from sp^2 to sp^3 or simply atomic discontinuity at the edge.[41] Defects in graphene are generally introduced during their growth or during subsequent processing for making electronic devices. They can also be introduced by irradiation of electrons and ion-beams to graphene.[110] In general, the nature and extent of defect depends upon the technique of making graphene. Some techniques result in graphene with low defect density, such as exfoliation, which can produce graphene with edge discontinuity as the only defect, which is unavoidable. Chemical derivation of graphene, such as reduced graphene oxide, tends to be more defective in general, due to incomplete reduction of graphene oxide. The popular methods of making large area or wafer size graphene, such as CVD and epitaxial, can also introduce defects.

Defects in a material generally tend to degrade their physical properties. However in graphene material system the defects can be exploited to tailor the local properties of the graphene to impart new functionalities. Banhart and co-workers have reviewed point and

line defects, and reconstructions of graphene lattice around these intrinsic defects leading

to interesting effects and potential application along with the roles of extrinsic defects such

as foreign atoms.[111] Defect density can also affect chemical sensing and broad band photo
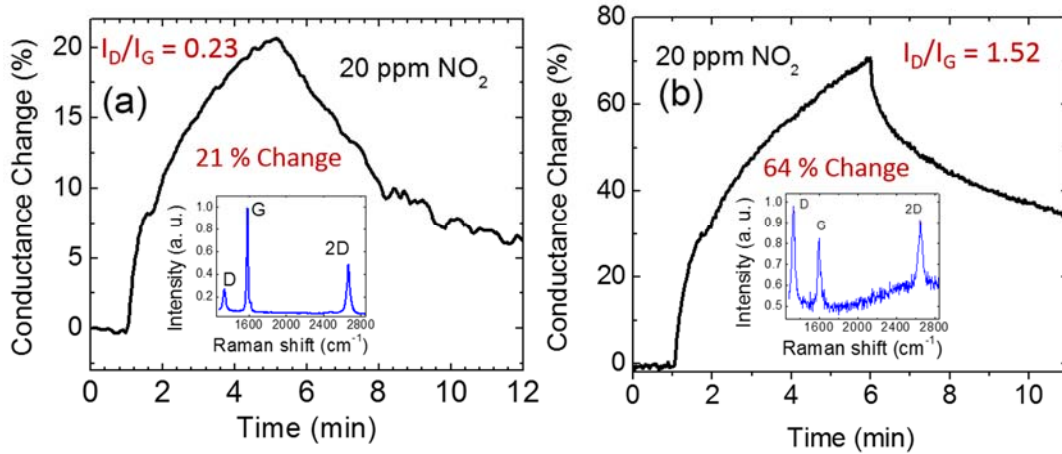
Figure 4.1 The role of defect in sensitivity enhancement. (a) The response of 21% for a low defect (I_D/I_G = 0.23 from Raman in inset) graphene chemiresistor. (b) A higher response of 64% for a highly defective (I_D/I_G = 1.52) chemiresistor.

detection of graphene based sensors. Theoretical calculations using density functional

theory has been used to predict the sensitivity of pristine, B-doped, N-doped, and defective

graphene.[112] The adsorption energies of CO, NO, NO_2 and NH_3 were determined for the

above mentioned graphene. The adsorption energy was found to be largest for defective

graphene and CO, NO, NO_2 combination, whereas in case of NH_3 it was B-doped graphene.

These calculations suggests that the defective or doped graphene have higher propensity to

adsorb gaseous molecules by virtue of their increase in adsorption energy or an increase in

the adsorption sites.[112]

We have also found similar sensitivity improvement for NO_2 using defective

graphene. Figure 4.1 illustrated this effect where inset shows the Raman spectrum

characterizing the defects in graphene chemiresistor. The device with low defect density ($I_D/I_G = 0.23$) shows a response of 21% upon exposure to 20 ppm NO$_2$ for 4 minute duration in Figure 4.1(a). Figure 4.1(b) shows sensitivity improvement to 64% under same test condition for a highly defective ($I_D/I_G = 1.52$) graphene chemiresistor. The sensing response in these two types of graphene chemiresistor with different defect density is the result of change in conductivity, as discussed in section 3.6, due to charge carrier exchange between chemisorbed NO$_2$ and graphene. Liang and co-worker have modeled[113] adsorption-desorption kinetics in carbon nanotubes and graphene based sensors by modifying kinetic Langmuir model. In this model a fraction molecules that are exposed to the surface will stick and adsorb in direct proportionality to number or concentration of available sites. This model addresses the incomplete recovery of the property such as conductivity by proposing two-types of adsorption sites, normal sites and poison sites. At poison sites the adsorbates bond very strongly as compared to normal site so that the time scale of desorption becomes much larger than the time scale of sensing measurements. Defects in graphene had been suggested to be the source of these poison sites. Once occupied they reduce graphene's sensitivity towards further exposure of analytes in subsequent measurements. Therefore these defects behave same as catalyst poising and has been characterized by different sticking coefficient in the model of Liang *et. al.*[113]

This model therefore suggest that more number of defects or poison sites will reduce the ability of the graphene sensor to recover after exposure to analytes despite the fact that more defects will increase the sensing response. This was observed in our measurements during recovery of graphene chemiresistors. The low defect sensor in Figure 4.1(a) shows a higher recovery of ~71% from a value of 21% Δσ to 6% Δσ for a duration

75

of 5 minutes of recovery after the NO₂ exposure was stopped, as compared to smaller recovery of ~40% in highly defective graphene in Figure 4.1(b) where Δσ dropped from 70% to 40% in the same duration of 5 minutes of recovery. In defective graphene we did observe the enhancement of about 3 times in sensitivity which is quite impressive but comes with a cost of longer recovery duration. Moreover despite of significant improvement of sensitivity in graphene chemiresistors by introduction of defects, these sensitivity values still remains fairly low due to liner dependence of conductivity change with number of adsorbed molecules.

4.2.3   Sensitivity Modulation by Heterostructure

In a simple graphene based chemiresistor or chem-FET the carrier transport in the device is governed by simple Ohm's law, $I \propto q\mu nE$, where I is current in the device, q is electronic charge, μ is mobility, n is carrier concentration, E is electric field across the device. The change in current caused by adsorbed gases, $\Delta I \propto \Delta n$ is linearly proportional to the transduction mechanism as illustrated in Figure 4.2(a) with the help of graphene band structure. However in diode structures the transport across the junction formed by a metal and a semiconductor is governed by thermionic emission model given by:[114]

$$I = I_S \left[exp\left(\frac{qV}{\eta kT}\right) - 1 \right] = AA^*T^2 exp\left(-\frac{\phi_B}{kT}\right) \left[exp\left(\frac{qV}{\eta kT}\right) - 1 \right] \quad (4.1)$$

where I_S is the reverse saturation current, A is the Schottky contact area, A* is the effective Richardson Constant, η is the diode ideality factor, T is the temperature, ϕ_B is the Schottky barrier height (SBH), and k is the Boltzmann constant. In reverse bias operation of a Schottky diode the magnitude of current is very small and is given by I_S term of the equation. The reverse saturation current is exponentially dependent upon the SBH, ϕ_B. The

SBH is determined by the difference of metal work function and semiconductor electron affinity.
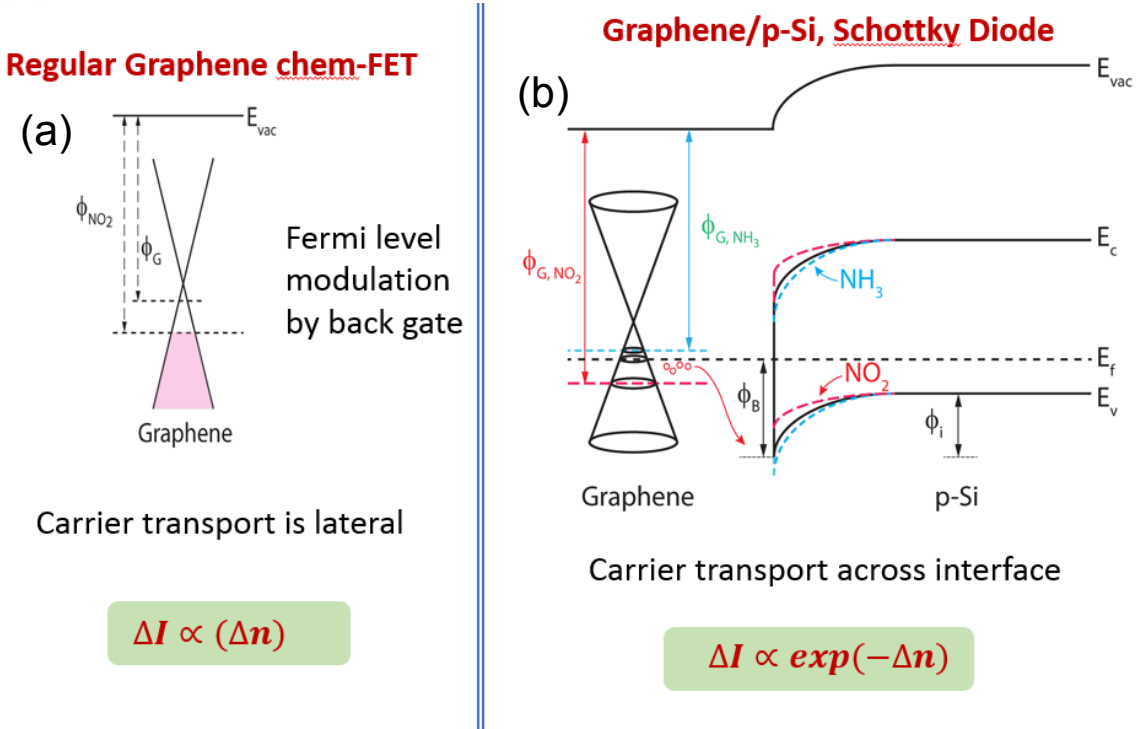
Figure 4.2 (a) In lateral transport, whether defect mediated or back gate modulated, the change in current, ΔI, is directly proportional to number of adsorbed molecules, Δn, for chemical sensing, (b) where as in vertical transport across a graphene/semiconductor heterostructure, ΔI can be exponentially dependent upon Δn.

If we happen to make a Schottky diode by use of graphene, semiconductor heterostructure then SBH will be determined by the difference of graphene's Fermi level and semiconductor's electron affinity as illustrated in Figure 4.2(b) with the help of graphene/p-Si equilibrium band diagram. The Fermi level of graphene is tied to carrier concentration in graphene by virtue of its atomic level thickness. The exposure of analytes on graphene surface will move its Fermi level up or down depending upon the type of doping. Now we will have $\Delta I_s \propto \exp(\Delta \phi_B \propto \Delta n)$ and the current in reverse bias will respond exponentially to number of adsorbed molecule in graphene semiconductor

heterostructure Schottky diode. Such chemical sensing device is expected to give highly sensitivity response to very low concentration of analytes. To test this hypothesis we fabricated graphene/Si Schottky diodes.
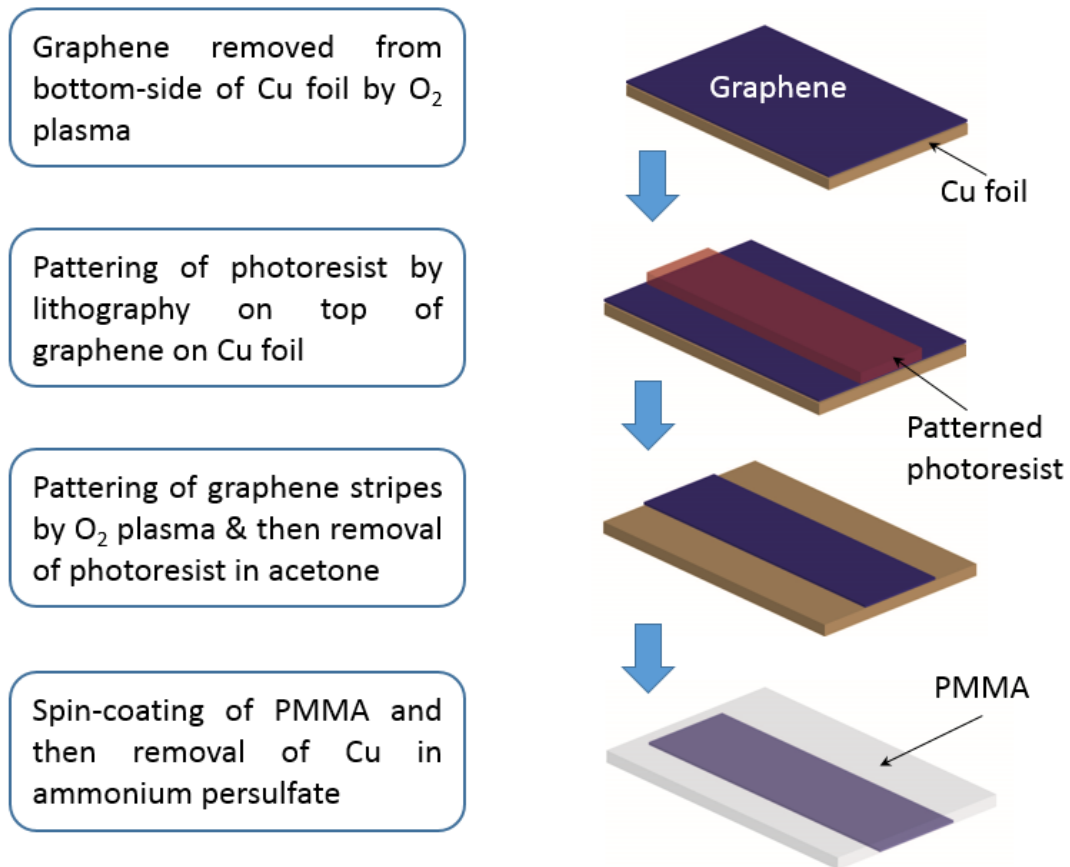
Figure 4.3 The main processing steps for the pattering of graphene before transfer on the patterned substrate by series of steps such as photolithography, O_2 plasma etch, PMMA coating and Cu removal.

4.2   Fabrication of Graphene/Si Diodes

The fabrication of graphene/Si diodes can be categorized in 3 stages of processing.

1) Processing of graphene

2) Preparation of SiO_2/Si substrate

3) Graphene transfer and post processing

4.2.1 Processing of Graphene

For these graphene/Si unique device structure we did not have readymade mask for patterning so we had to improvising upon the available processing technique. For this reason entire processing was broken into three broad processing. This first one required the pattering of graphene on copper foil itself before transferring it on the substrate. The lithography on transferred graphene was avoided in order to minimize the introduction of
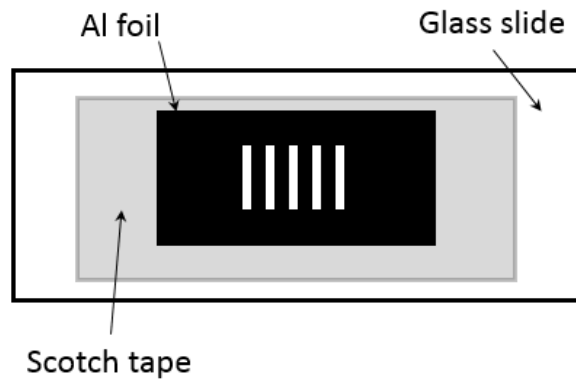
Figure 4.4 Homemade mask on Al foil for defining sub mm size stripe of CVD graphene on Cu foils

processing related defects in graphene. The sequence of major processing steps are illustrated in Figure 4.3.The very first step was to pattern graphene in sub mm wide stripes. For this purpose a homemade mask of Al foil having sub mm width window opened by a razor blade was employed. Figure 4.4 illustrates this mask on glass slide where masking material was Al foil and scotch tape composite. 1813 photoresist was coated at 4000 rpm for 30 sec duration to perform the positive resist lithography. Strips were defined by O_2 plasma etch in RIE chamber. Thereafter patterned graphene on Cu was heated in acetone at 60 °C for 10 min to remove the resist. Then Cu foil with graphene strips was coated
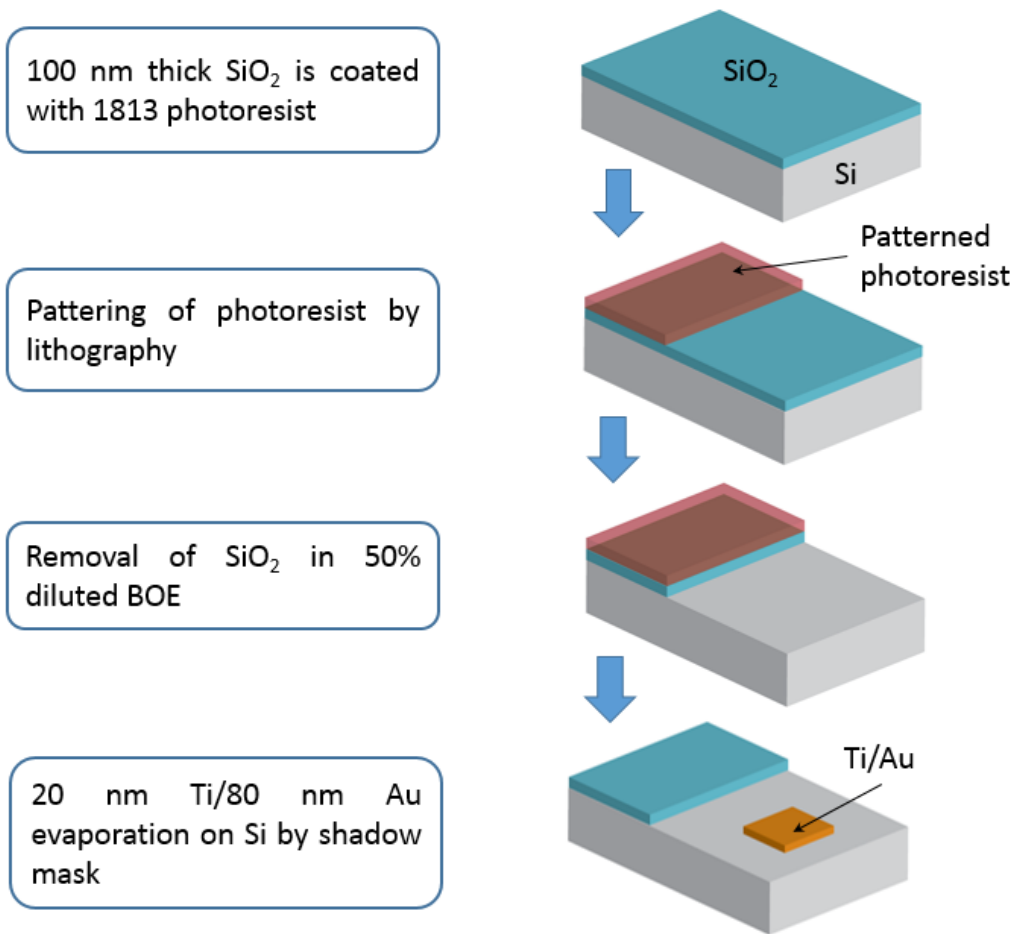
Figure 4.5 The processing steps for the pattering SiO$_2$/Si substrate and deposition of metal contacts on Si.

with two layers of poly methyl methacrylate (PMMA), to add mechanical strength during subsequent processing, and baked for 1 min at 150 °C. Next, the graphene layer on the back side of the sample was removed by oxygen plasma etching, which was followed by Cu etching in 0.5 M ammonium persulfate solution for more than 12 hour, releasing the graphene/PMMA bi-layer.[115]

4.2.2 *Processing of SiO2/Si Substrate*

The p- and n-Si used in this work lightly doped and have resistivity in the range of 1-10 Ω-cm. This light doping ensures the contact with graphene to remain Schottky. Both types of Si has 100 thick dry thermal oxide on them. The SiO_2 on both p- and n-Si has been
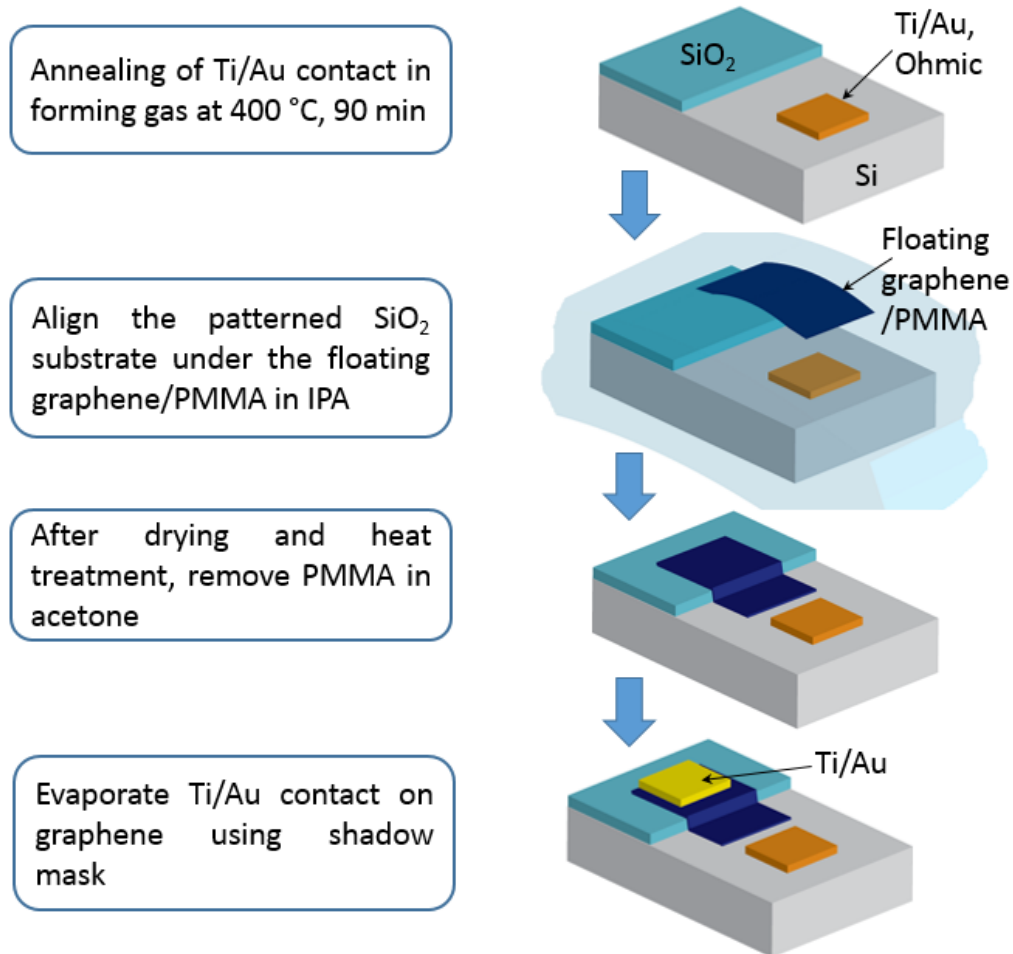
Figure 4.6 The graphene transfer process on top of patterned SiO_2/Si substrate is shown here schematically.

selectively removed by 1:5 diluted buffered HF. The processing steps are described in Figure 4.5. Ti/Au was deposited on the back side and selectively on top side of Si using a shadow mask. The sample was then annealed in forming gas atmosphere at 400 °C for 90

minutes to make ohmic contacts. The forming gas was obtained by flow Ar and H_2 at 800 and 200 sccm respectively.

4.2.3   Graphene Transfer and Post Processing

Graphene/PMMA bi-layer was rinsed thoroughly in deionized water and IPA. The patterned SiO_2/Si substrate congaing annealed Ti/Au ohmic contacts were dipped in BOE for 10 sec in order to remove native oxide just prior to graphene transfer. The patterned substrate was then inserted under the graphene/PMMA bi-layer floating in IPA. It was carefully aligned so that the graphene stripe remains perpendicular to etched SiO_2 edge on Si substrate. The solvent is then removed carefully to let graphene/PMMA to settle down gently on the substrate. Figure 4.6 captures this part of processing. It was then baked at 220 °C for 5 minutes to reflow the PMMA resulting in more uniformity and less cracking in transferred graphene. Finally, the sample was placed in acetone for 2 hour to remove PMMA.[115, 116] Ti (20 nm)/Au (80 nm) contacts were evaporated on graphene transferred on SiO_2/Si using shadow mask.

4.3   Characterization of Graphene/Si Diode

4.3.1   Raman Characterization of Graphene/Si Diode

It is possible to learn the amount of defects generated in graphene during the processing by Raman spectroscopy by D peak intensity. Figure 4.7(a) shows the Raman spectrum for the as-grown CVD graphene on copper foil, which was used for the diode fabrication, showing signature D, G, and 2D peaks. The I_D/I_G ratio of 0.2 indicates good quality of the graphene. The I_G/I_{2D} ratio of 3.9 and 2D peak full width at half maximum (FWHM) of ~21.33 cm^{-1} indicates the presence of single layer graphene.[45] Raman spectra

82

of graphene transferred on Si and SiO₂/Si substrates from the graphene/p-Si devices are also shown in the middle and bottom panels of Figure 4. 7(a). The I_D/I_G ratio of 0.2 and
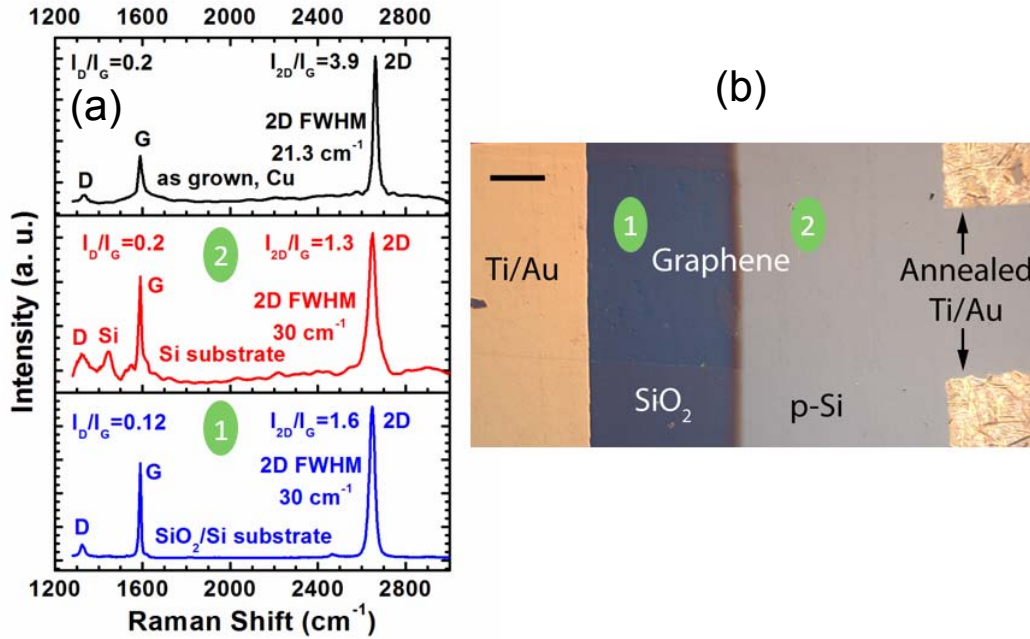
Figure 4.7 (a) Representative Raman spectra of CVD graphene grown on copper (top panel), transferred on Si (middle panel) and SiO₂/Si (bottom panel) substrate showing the characteristic G, D and 2D peaks. (b) Optical micrograph of a graphene/p-Si Schottky diode illustrating transferred graphene on SiO₂ and p-Si, Ti/Au contact on graphene and annealed Ti/Au contact on p-Si. The scale bar is 200 μm.

0.12 suggest that the quality of graphene remains preserved by and large during the transfer process. The extra defects are not generated during the device processing as well, highlighting the robustness of graphene device processing.

Figure 4.7(b) captures the optical micrograph of one of the graphene/p-Si diode. Annealed Ti/Au electrodes are seen at the right corners with rough morphology. Whereas the same Ti/Au contacts, deposited separately, on graphene appear to have smooth morphology in absence of annealing. It was determined from TLM characterization that forming Ohmic contact on graphene by Ti/Au does not require annealing. Graphene can

be seen on top of SiO_2 at location 1 due to contrast generated with thin film of SiO_2 whereas no contrast is generated for graphene on top of Si. This is again indicative of the optimization achieved in clean transfer and processing.

4.3.2 Current-Voltage Characterization of Graphene/Si Diodes

Electrical characterization of the graphene/Si heterojunction showed Schottky type current-voltage (I-V) characteristics, which is in agreement with earlier reports.[117] A voltage bias was applied to the Si contact for both p- and n-Si diodes and the graphene contact was kept as ground. Representative I-V characteristics for graphene/p-Si and graphene/n-Si heterojunction Schottky diodes are shown in Figure 4.8. In both cases, the diode current increases exponentially with voltage initially (up to ~ 1V, see inset plots), before being dominated by series resistance. Nonetheless, these results are consistent with recent reports,[117] indicating that graphene forms Schottky contact with both n-type and p-type Si. This is expected since the reported work function for graphene of 4.5 eV is about midway between the work functions for p-type and n-type Si with electron affinity of 4.05 eV and bandgap of 1.12 eV at room temperature. Examining the insets in Figure 4.8, we find that in reverse bias the current increases monotonically with increasing bias magnitude This is because with increase in reverse bias graphene's work function changes (due to change in carrier concentration), which causes a lowering of the SBH.[118, 119] The insets of Figure 4.8(a,b) show the logarithmic I-V plots for graphene Schottky junctions with p- and n-Si, respectively. Using these plots, and the measured area of 9×10^{-3} cm^{-2} and A^* values of 46.32 and 252 $Acm^{-2}K^{-2}$ for p-Si[120] and n-Si,[121] respectively, we find $\eta = 4.88$, and $\phi_B = 0.65$ eV for the former, and $\eta = 3.7$ and $\phi_B = 0.71$ eV, for the later. These values are

in close agreement with those reported recently.[119, 121] Notably, for these junctions, $\eta > 1$ is commonly observed, which has been attributed to barrier height variation with reverse bias arising from graphene's bias dependent work function, image charge induced Schottky
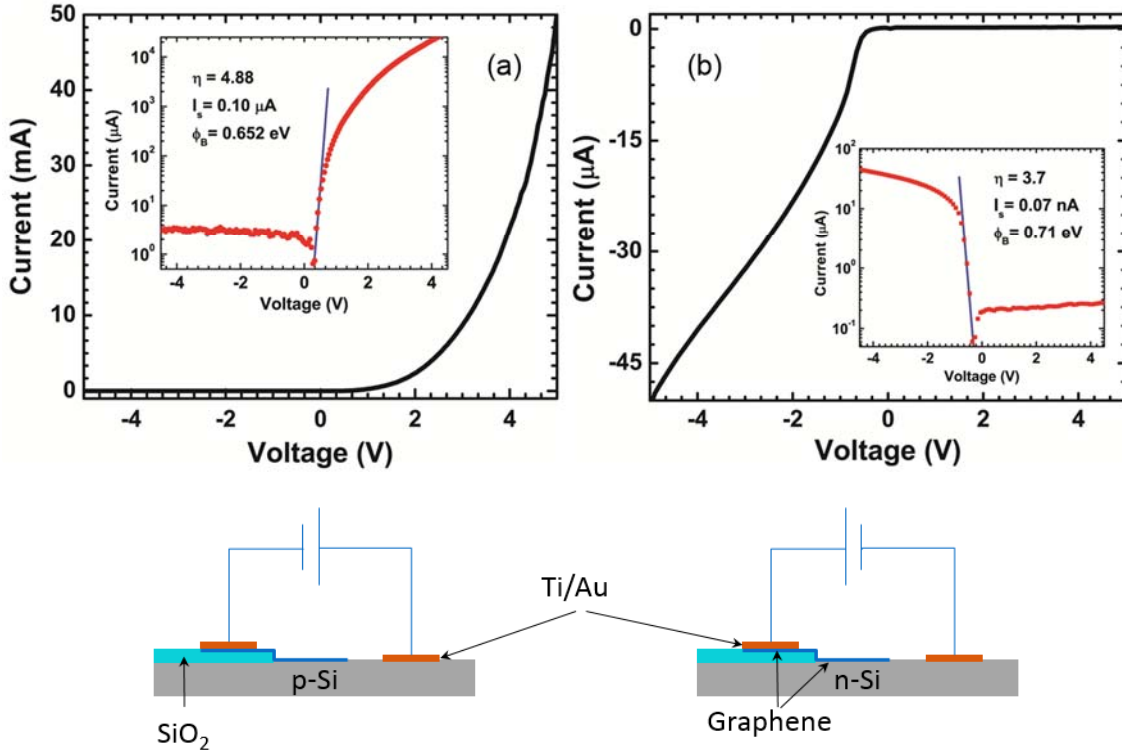
Figure 4.8 Current-Voltage (I-V) characteristics of (a) graphene/p-Si and (b) graphene/n-Si devices showing rectifying behavior. I-V characteristics in logarithmic scale shown in the inset exhibit 4 and 3 orders of magnitude change in current for graphene/p-Si and graphene/n-Si devices, respectively.

barrier lowering, and Schottky barrier inhomogeneity.[118, 119, 122]

4.3.3 Diode Current-Voltage in Different Environment

Upon establishing the Schottky behavior of the fabricated devices, the current-voltage characteristics were performed under different experimental conditions to assess their suitability in chemical sensing. 20 ppm NO_2 and 550 ppm NH_3 was used to study the responses in both dark and illuminated (using light from a halogen lamp using a fiber optic
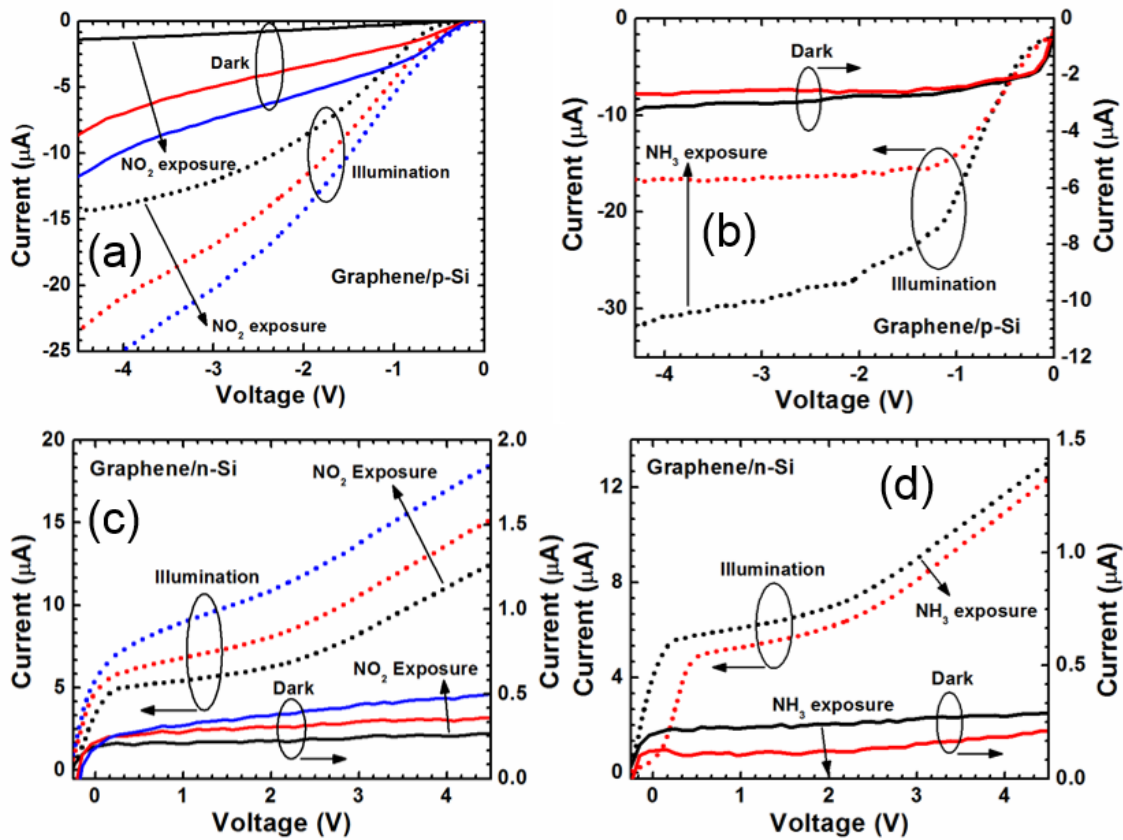
Figure 4.9 Reverse bias current-voltage characteristics of graphene/p-Si in dark and in illumination for different exposure times of (a) NO_2 and (b) NH_3. The solid curves correspond to measurements in dark condition and dotted curves to those under illumination. The black (both solid and dotted) curves represent pre-exposure characteristics, while the red and blue curves represent those after 10 minutes and 30 minutes of gas exposure. Reverse current across the graphene/n-Si heterojunction device (c) is increasing for NO_2 and (d) decreasing for NH_3.

cable) ambient conditions. The reverse bias I-V characteristics of the graphene/p-Si diode sensor recorded after different durations of exposure to NO_2 and NH_3 are shown in Figure 4.9(a, b) respectively. We find that with NO_2 exposure, the current increases dramatically both in dark and illuminated conditions due to lowering of the SBH. For example, at -4V bias, the current increased more than 8 times from 1.2 to 9.8 μA (a change of 716 %) with

30 minutes of NO_2 exposure in dark, while it increased from 13.9 to 24.9 μA (a change of 79 %) for the same duration under illumination. In contrast, for NH_3 exposure the change (reduction) in current is rather small in dark (13.6%), but improves under illumination (Figure 4.9(b)), with the current decreasing from 30.5 to 17.4 μA after 30 min exposure (a change of 43%). The response for NO_2 is extremely large, and to the best of our knowledge have not been observed with any graphene based sensor in ambient conditions till date. For, Graphene/n-Si devices, similar responses have been obtained, i.e. NO_2 response (Figure 4.9(c)) is large and increases with exposure time, while for NH_3 (Figure 4.9(d)), there is clear distinctive response in presence of both dark and light, but it saturates quickly.

4.3.4 Capacitance-Voltage Measurements

To determine the magnitude of change in SBH at graphene/Si heterojunction due to molecular adsorption, capacitance-voltage (C-V) measurements were performed (i) in air at steady state, (ii) after 20 min of 20 ppm NO_2 exposure, and (iii) after 20 min of 550 ppm NH_3 exposure. The $1/C^2$ vs. V_R plots obtained for 20 min of NO_2 and NH_3 exposure are compared to those obtained prior to gas exposure in Figure 4.10(a). The built-in voltage, V_{bi} can be determined from the relationship between the C^{-2} and applied reverse bias V_R given as:

$$C^{-2} = \frac{2(V_{bi} + V_R)}{q \epsilon_S N_{A/D}} \qquad (4.2)$$

Here q is the electronic charge, ϵ_s is the semiconductor permittivity, and $N_{A/D}$ is the acceptor/donor doping.[123] From extrapolating the plots, the built-in voltages (V_{bi}) are determined as 0.69 eV for pre-exposed condition, and 0.46 and 0.85 eV after 20 min exposure to NO_2 and NH_3, respectively. The graphene/p-Si SBH is given as, $\phi_B = V_{bi} + (E_F - E_V)$, where E_F is the Fermi level and E_V is the valance band edge of Si. $E_F - E_V$ is

estimated to be ~ 0.2 eV for the p-type Si used from the resistivity of $1 - 10 \ \Omega$cm specified by the manufacturer. Thus, the pre-exposed SBH becomes 0.89 eV, which is in good agreement with earlier results.[119, 124] Figure 4.10(b) illustrates the time evolution of V_{bi}
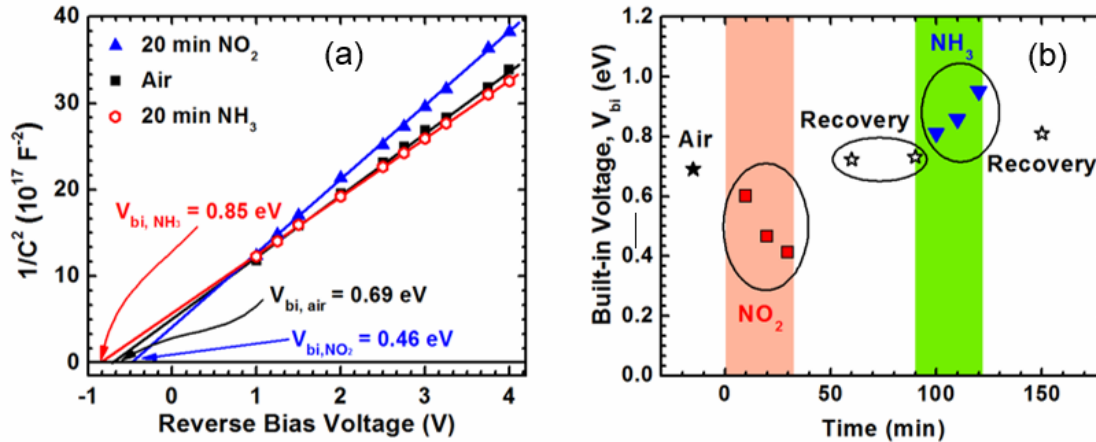
Figure 4.10 (a) Built-in voltage extracted from the C^{-2} vs. reverse voltage plot for graphene/p-Si in ambient condition (black square), in NO_2 (blue triangle) and in NH_3 (red hexagon). The gas exposure duration was 20 minutes for both NO_2 and NH_3. (b) Time evolution of extracted built-in voltage in the different conditions: in ambient air, NO_2 exposure, at recovery, NH_3 exposure and at recovery again.

from initial steady state value in ambient condition, as the 20 ppm NO_2 flow is started over the sensor and stopped, and 550 ppm NH_3 flow is started and stopped, successively. As expected, we find that V_{bi} keeps on decreasing from the initial steady state value of 0.69 eV upon exposure to NO_2, and then recovers back close to the initial value as the NO_2 flow is stopped. It further continues to rise with NH_3 exposure, and recovers back to the original steady state value as the NH_3 flow is stopped. We find that the change in V_{bi}, and hence in SBH, due to NO_2 exposure is larger than that due to NH_3 exposure (0.23 and 0.16 eV, respectively, in 20 min), in spite of the much higher concentration of the later. This can be attributed to the weak electron donating nature of NH_3 (0.03q) compared to the strong electron accepting (0.3q) nature of NO_2.[101] The SBH determined from C-V measurements

is higher than that obtained from I-V measurements, i.e. 0.89 and 0.65 eV, respectively for

graphene/p-Si diodes (steady state value in ambient). The difference can arise partly from

the uncertainty in determining $E_F - E_V$ (see above discussions), and also from Schottky
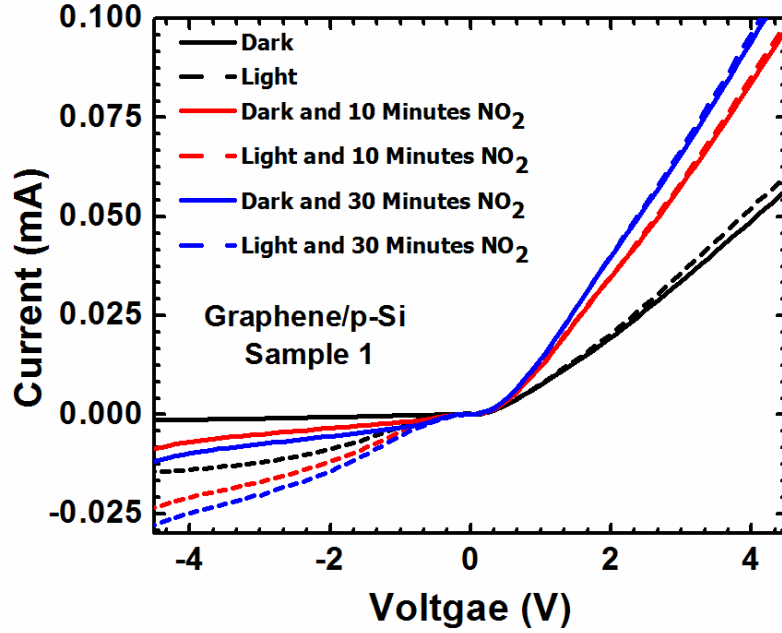
Figure 4.11 Complete current-voltage characteristics of graphene/p-Si diode under optical illumination and under dark conditions with 10 and 30 minute duration of 20 ppm NO₂ exposure.

barrier inhomogeneity and additional leakage paths at the junction, which generally

underestimates the SBH determined from I-V measurements.[118, 119, 122]

4.4 Graphene/Si Chemi-Diode Performance

4.4.1 *Forward Bias verses Reverse Bias Sensing in Chemi-Diode*

Compared to the sensing responses observed in reverse bias, the forward bias

responses for both NO₂ (20 ppm) and NH₃ (550 ppm) are significantly lower, i.e. 92% and

6.5% at 4V bias for graphene/p-Si Schottky diode, compared to 716% and 43% for 4 V

reverse bias, respectively. The change in the entire I-V characteristics of the diodes with
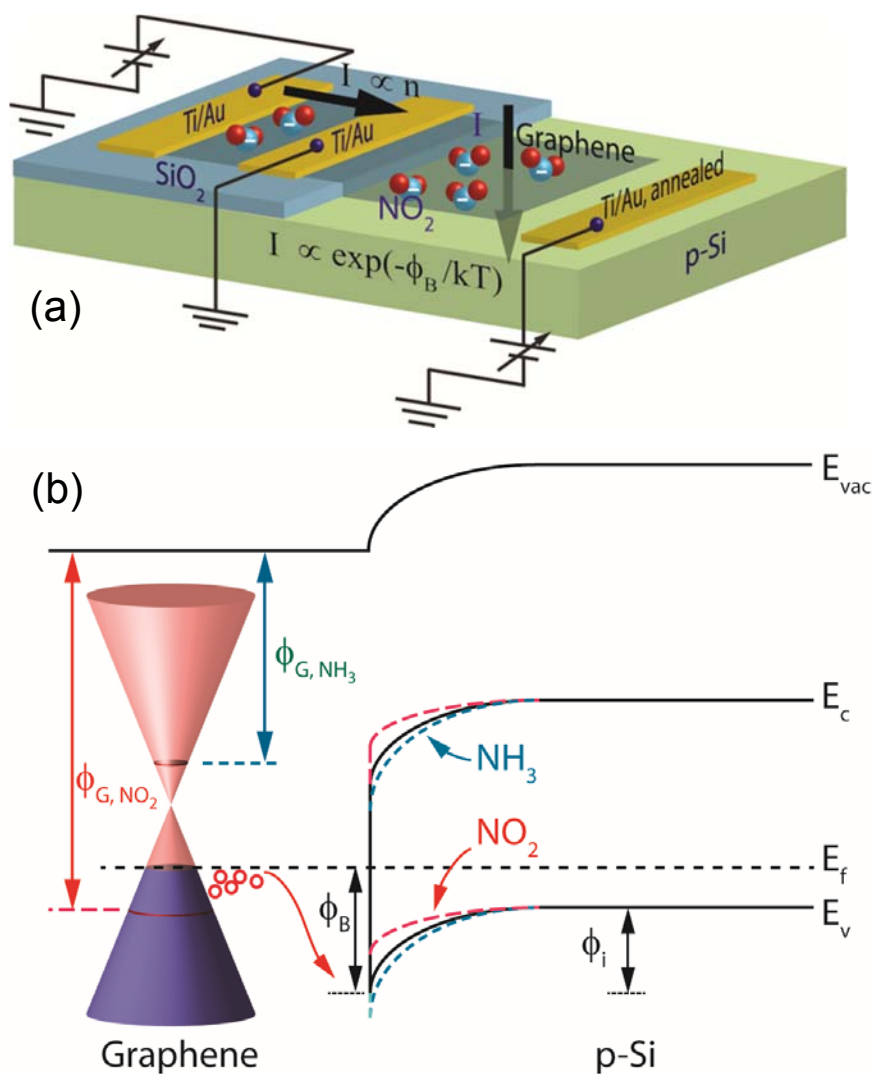
Figure 4.12 (a) Device schematic and biasing scheme of graphene chemiresistor and graphene/Si Schottky diode sensor fabricated on the same chip. Chemiresistor is a case of lateral transport where current is proportional to number of charge carriers in graphene. Whereas the carrier transport across the vertically stacked graphene/p-Si heterojunction results in current that is exponentially dependent upon SBH under reverser bias condition. (b) The energy band diagram of Graphene/p-Si heterostructure in three different conditions, showing reduction in SBH for NO_2, and increase in SBH for NH_3 exposure, as compared to the pre-exposure condition.

NO_2 and NH_3 exposure is shown in Figure 4.11. This can be attributed to the effect of diode series resistance which becomes significant for forward bias operation, as discussed earlier.

Similarly, our responses of 43% obtained at -4V bias for 550 ppm NH_3 is much improved

compared to the forward bias response of only a few percent obtained for graphene/Si Schottky diode sensor for 4% NH_3 as reported in reference 15. Although, biasing the diode in the sub-threshold region can minimize the effect of diode series resistance, it is difficult to reliably bias a sensor in this region due to environmental factors affecting the turn-on voltage. In addition, it would not be possible to tune the diode sensitivity in forward bias as it can be done in reverse bias.

4.4.2   Chemi-Diode verses Chemiresistor

To make a direct comparison of the performance of the graphene/Si heterojunction diode sensor and conventional graphene chemiresistor type sensor, both the devices were fabricated side by side on the same chip from the same transferred graphene film. The chemiresistor was fabricated on SiO_2 covered area of a Si substrate, while the heterojunction diode sensor was fabricated on bare Si with SiO_2 etched away, as shown schematically in Figure 4.12(a). The I-V characteristics of graphene Chemiresistor is shown in Figure 4.13(c). The responses from the two sensors are compared in Figure 4.13(a) for 10 min NO_2 exposure (shaded region). We observe that the chemiresistor current changes by only 7.8 %, increasing from 1.027 to 1.1065 mA, while that in the diode sensor changes by 104 % increasing from 2.12 to 4.34 μA, under the same applied bias magnitude of 4 V (reverse bias for the diode sensor). This constitutes a 13.3 times enhancement in response for the diode sensor compared to the regular chemiresistor sensor, clearly highlighting the improved performance of the former. For NH_3 the difference in response is less dramatic, but a significant 3 times higher response is observed for Graphene/p-Si diode sensors compared to the graphene chemiresistor (Figure 4.13(b)). Very significantly, the reverse bias operation of the diode sensor enables it to operate at a

much lower power level of 2.12 μA × 4 V = 8.48 μW compared to the chemiresistor, which requires an operational power of 1.027 mA × 4 V = 4.108 mW, a reduction of 484 times, which is highly desirable for sensor system design.
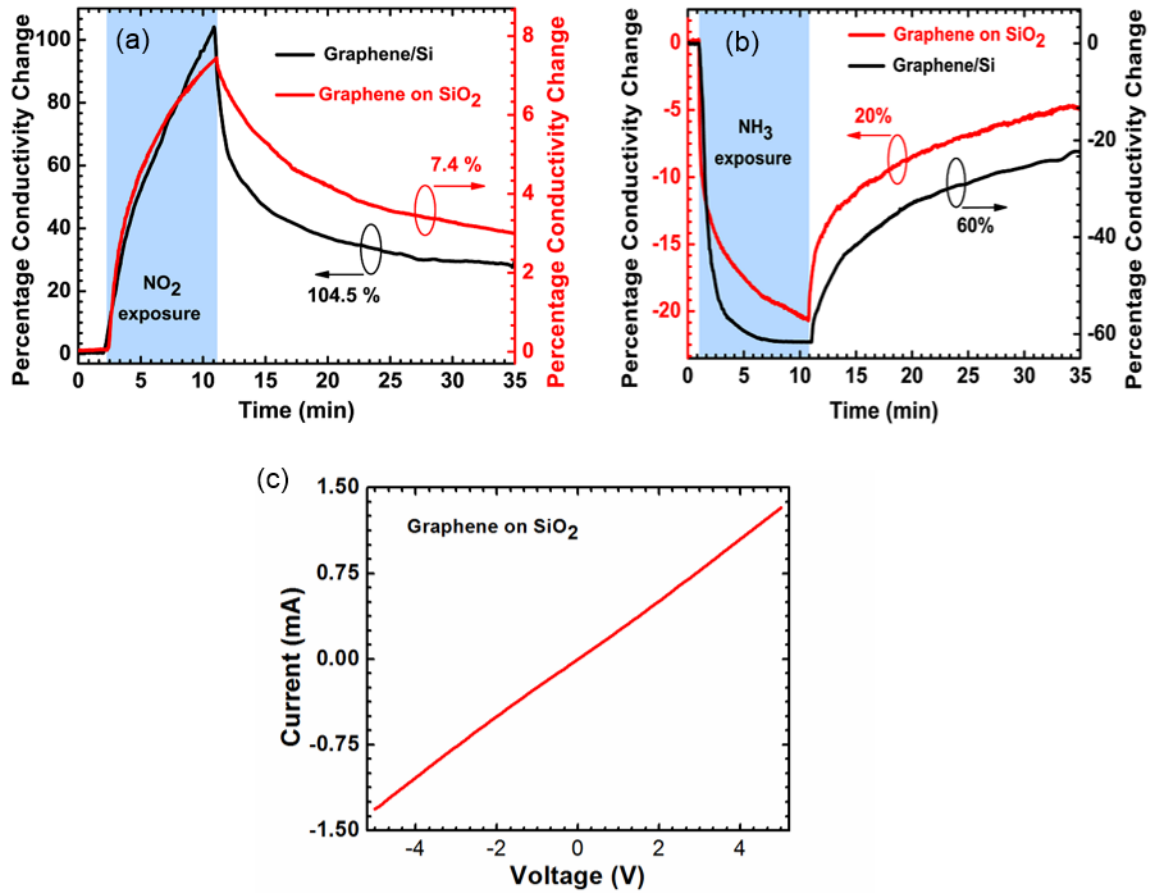
Figure 4.13 (a) Comparison between the NO₂ responses of graphene/p-Si heterojunction device and graphene chemiresistor on SiO₂ fabricated on the same chip side by side. The black line shows the response of graphene/p-Si device and red line shows the response of graphene on SiO₂ for NO₂ exposure. The exposure duration (10 minutes) and bias voltage magnitude (4V) is same for both the cases where reverse bias is applied across the graphene/p-Si device. (b) Comparison of NH₃ sensing behavior where the black and red lines show the responses of the graphene/p-Si device and graphene chemiresistor, respectively, for NH₃ exposure. (c) Current-Voltage characteristics of graphene chemiresistor on SiO₂

Careful observation of Figure 4.13(a,b) indicates that exposure to NO₂ results in a fast and almost linearly changing conductivity, which does not saturate even after 10 min

of exposure. In contrast, with NH$_3$ exposure, the conductivity changes at a slower rate (in terms of percentage change), and reaches a constant value in 1 – 2 min. This can be explained by considering previously reported results that the propensity for charge transfer between adsorbed molecules and graphene decreases as the graphene Fermi level moves closer to the defect level introduced by the adsorbed molecules.[100] Initially, the graphene Fermi level, though below Dirac point, is much closer to the NH$_3$ induced defect level, which is slightly above the Dirac point, compared to NO$_2$ defect level which is typically formed 300 – 400 meV below the Dirac point (Figure 4.12(b) shows the band diagram for graphene/p-Si heterojunction along with the NO$_2$ and NH$_3$ induced defect levels).[100, 101, 109] Therefore, the charge transfer process between NO$_2$ and graphene is much faster compared to NH$_3$, for which the response saturates as the Fermi level reaches close to the defect energy level introduced by its adsorption. To verify this idea further, we performed a series of measurements and studied the response as a function of concentration, exposure time and reverse bias voltage.

4.4.3   Chemical Concentration Dependence of Chemi-Diodes

Figure 4.14(a) shows the sensor response as a function of NO$_2$ concentration downward from 20 ppm. We find that a concentration down to 200 ppb can be sensed easily, although the response is slower for lower concentrations, probably due to the sensor operation in ambient conditions. The response plotted as a function of concentration in logarithmic scale (Figure 4.14(b)) shows a linearly increasing sensitivity from 7 to 410% for a concentration variation from 200 ppb to 20 ppm. The NH$_3$ response for 5 minutes exposure is shown in Figure 4.14(c) with concentrations varying from 10 to 550 ppm. The response magnitude can be seen to increase logarithmically with the increase in
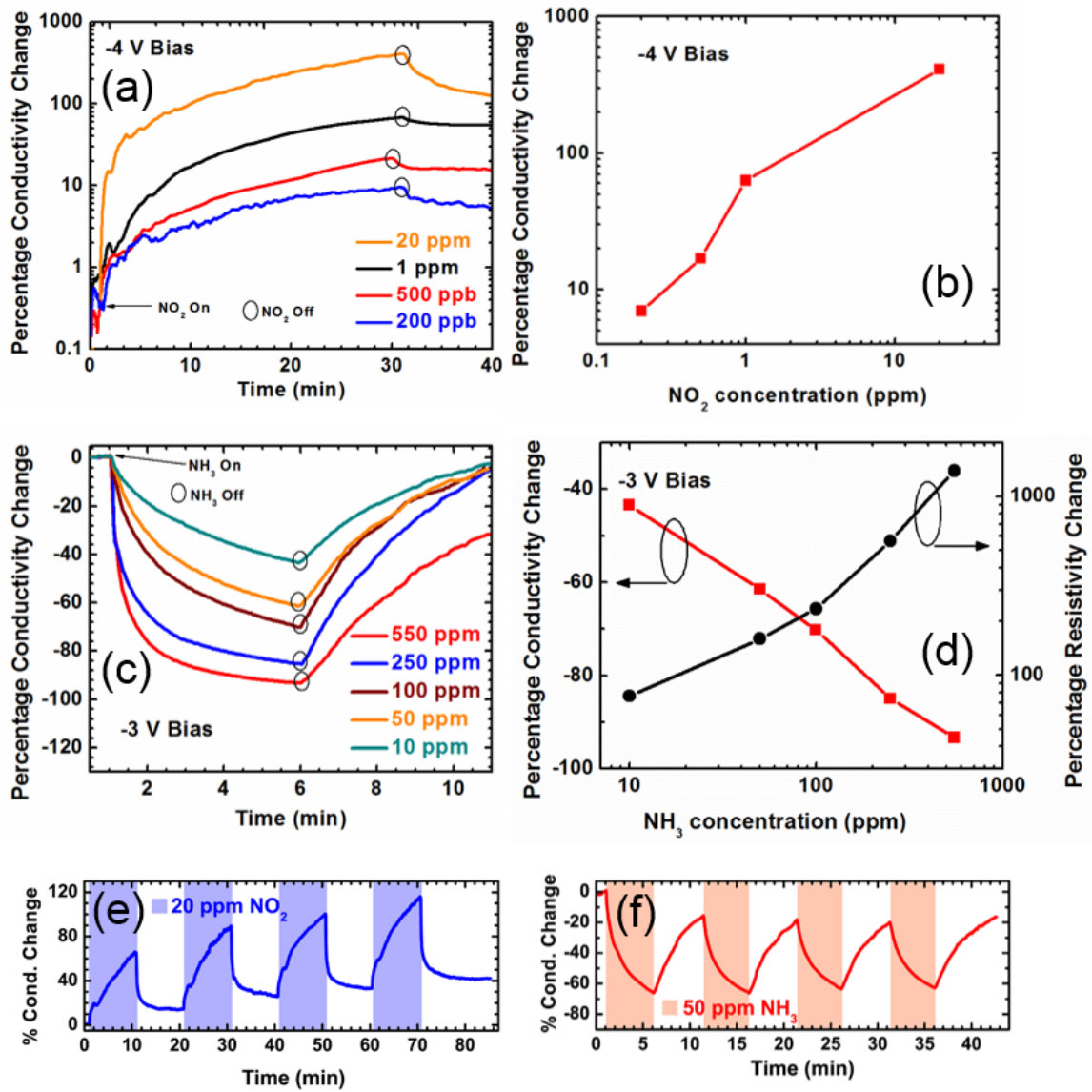
Figure 4.14 (a) Sensor response for different NO_2 concentration decreasing from 20 ppm to 200 ppb for 30 minutes of exposure at -4 V reverse bias. (b) Log-log plot of the maximum conductivity change as a function of NO_2 concentration. (c) Sensitivity plots for different concentration of NH_3 varying from 550 ppm to 10 ppm for 5 minutes of exposure at reverse bias of -3V. (d) Logarithmic plot of maximum conductivity change along with the corresponding resistivity change with NH_3 concentration. The repeatability of sensor response of the diodes is illustrated for (e) 20 ppm NO_2 and (f) 50 ppm NH_3 sensing

concentration as shown in Figure 4.14(d). However, a logarithmic plot of percentage resistivity change as a function of concentration is almost linear as seen in Figure 4.14(d).

94

For 10 ppm, the conductivity magnitude change is 43.4% which increased to 93.3% for 550 ppm NH_3. The corresponding resistivity change is 76.6% for 10 ppm and an enormous 1392.5% for 550 ppm NH_3. To investigate the repeatability of the reverse biased sensor response, it was exposed to 20 ppm NO_2 and 50 ppm NH_3 for 4 successive cycles, and the responses are shown in Figures 4.14(e) and (f), respectively. For the initial NO_2 exposure, the graphene/p-Si sensor shows 64% increase in conductivity in 10 minutes. The recovery was carried out in ambient condition for the same time duration (10 minutes), and the sensor recovered to less than 20% of the maximum response (Figure 4.14(e)). For the subsequent cycles the sensor showed very good repeatability, although the maximum value of the response increased slightly in every cycle due to incomplete recovery. The graphene/p-Si sensor showed very repeatable responses for 50 ppm NH_3 as well, when exposed to 5 minutes on/off duration for 4 consecutive cycles. For the initial NH_3 exposure, the sensor showed 66% decrease in the conductivity and in 5 minutes recovered to less than 20% in ambient condition (Figure 4.14(f)). Very similar responses were recorded for the next 3 cycles. Thus, we find that for both electron acceptor and donor type of gas molecules the diode sensor responses are quite repeatable. Although we have included sensing response down to 200 ppb of NO_2, with proper optimization of the sensor, detection down to low ppb range is anticipated. In the low frequency range (<100 KHz), which is relevant for sensor operation, the ultimate sensor performance is typically limited by the 1/f noise, which in graphene chemiresistor sensors arises out of the fluctuations in number of charge carriers and mobility caused by charged impurities and scattering centers.[57] For the proposed sensor based on graphene/Si heterojunction, the 1/f noise is still expected to be predominant in low frequencies, however, the factors affecting it need to be carefully

investigated, especially bearing in mind that the overall noise is affected by current transport through a graphene resistor, a graphene/Si heterojunction and a Si resistor.
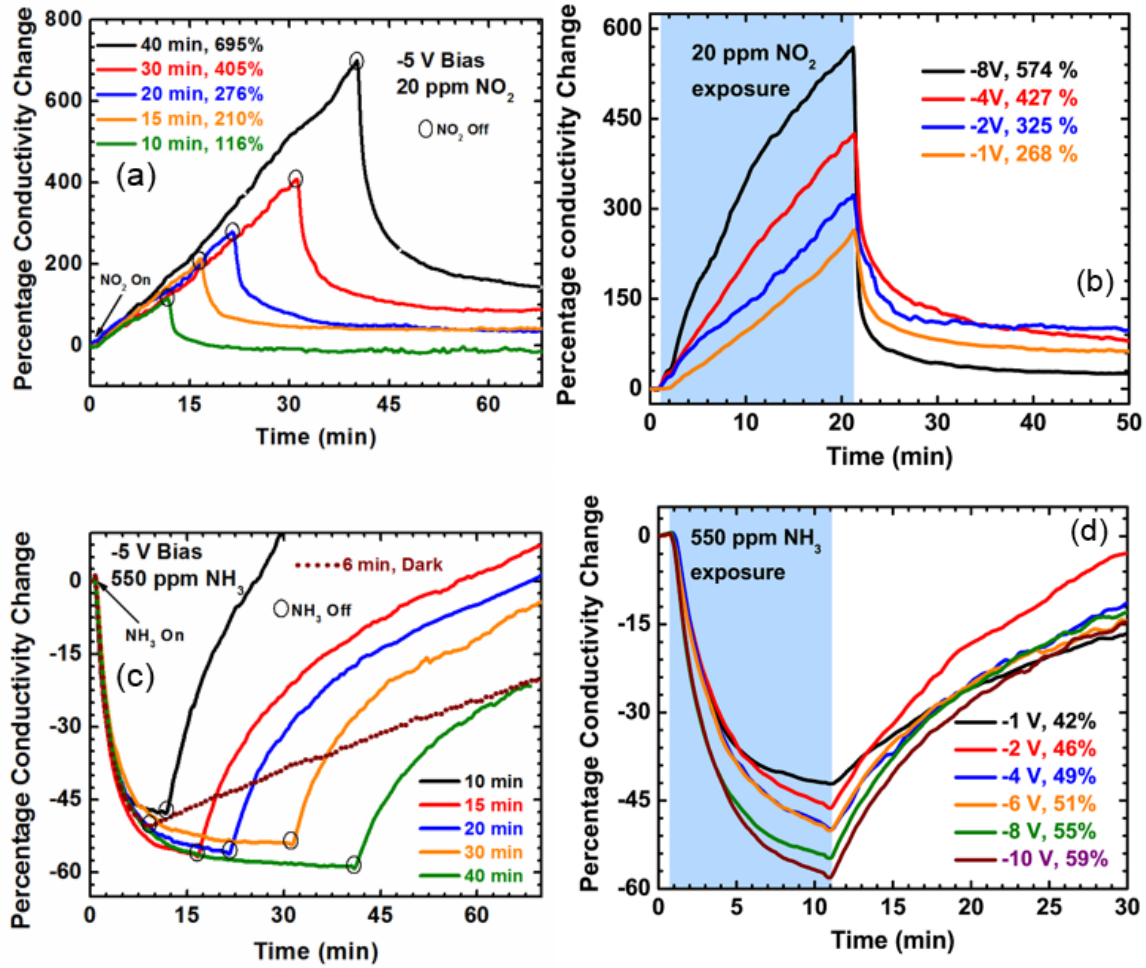
Figure 4.15 The diode response as a function of exposure time and reverse bias has been illustrated here. (a) Sensitivity to 20 ppm NO_2 for different exposure time where no saturation of the diode is observed till 40 minutes of exposure. (b) Diode response for 20 minutes of exposure to 20 ppm NO_2 at varying reverse bias of -1 to -8V suggesting a tunability of response is possible by varying the reverse bias. (c) Response to 550 ppm of NH_3 with different exposure time. A saturation behavior is observed for current lowering NH_3. (d) Diode response to 10 minutes of exposure to 550 ppm NH_3 at different reverse bias from -1 to -10V suggesting a tunable response to NH_3 as well

4.4.4 Sensitivity Tuning in Chemi-Diodes

Figure 4.15(a,b) shows the effect of exposure time and bias voltage for NO_2, while those for NH_3 are shown in Figure 4.15(c,d). From Figure 4.15(a,b) we find that simply increasing the duration of exposure to NO_2 does not affect the rate of change of current to a noticeable extent, however, changing the magnitude of the applied reverse bias affects it significantly. With higher reverse bias, the current increases at a faster rate initially, but shows some tapering afterwards, which can be clearly seen for V_g = -8 V. With more negative bias applied to p-Si, the graphene Fermi level goes down further away from the Dirac point toward the NO_2 defect level, reducing the SBH. The reduction in SBH causes the junction current to increase, and responses to be faster initially, which however tapers

Table 4.1 Approximate rise and recovery rate for NO_2 and NH_3 exposure at different bias voltage

Bias Voltage (V)	Rise Rate (NO_2) (percentage/sec)	Recovery Rate (NO_2) (percentage/sec)	Rise Rate (NH_3) (percentage/sec)	Recovery Rate (NH_3) (percentage/sec)
-1	0.19	1.61	0.28	0.04
-2	0.22	1.88	0.23	0.06
-4	0.41	3	0.27	0.06
-8	0.71	7.43	0.38	0.08

off as the Fermi level approaches the NO_2 defect level (Figure 4.15(b)). Such tapering effects are clearly seen for NH_3 responses in Figure 4.15(c,d), where the responses saturate early, as expected from discussions above, and do not change with varying exposure time. With the application of higher reverse bias, the Fermi level moves downward, increasing

its separation with the NH$_3$ induced defect level, and causing the NH$_3$ responses to exhibit less saturating trend as seen from Figure 4.15(d).
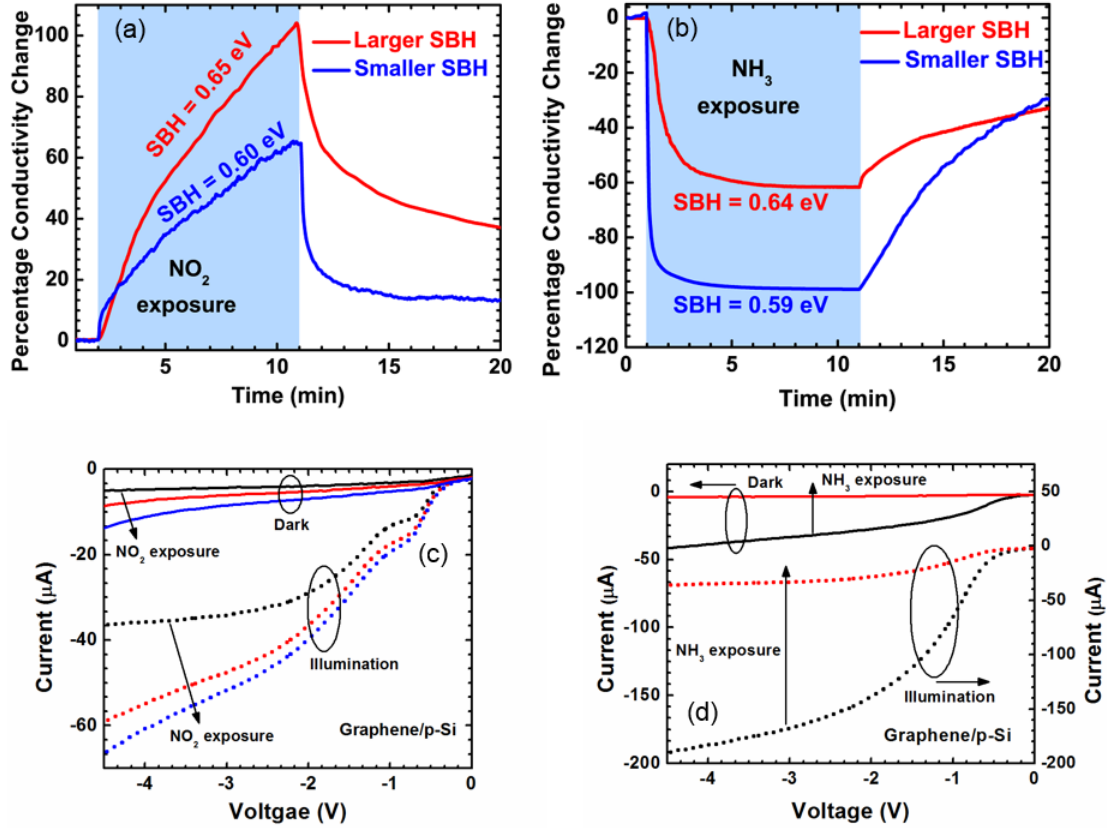
Figure 4.16 The effect of SBH on Graphene/p-type heterostructure Schottky diode sensitivity for (a) NO$_2$ and (b) NH$_3$. Effects of (c) NO$_2$ and (d) NH$_3$ exposure on reverse biased I-V characteristics for a diode sensor. Black curves correspond to pre-exposed condition, solid for dark and dotted for illumination, red curve corresponds to 10 min and blue to 30 min of gas exposure. Lower SBH of the diode sensor results in inferior response to NO$_2$ exposure (c) and improved response for NH$_3$ (d) is observed compared to the responses in Figure 4.9(a,b) respectively.

Although the response and recovery times for the sensors cannot be determined directly from Figure 4.15, (since the sensor response did not saturate or recover fully within the time period of measurement), the temporal response of the sensor can still be quantified

by the rise rate, the percentage change in conductivity per sec, which is typically dependent on the analyte concentration. For NO_2, the extracted rise rate shows a linear increase with the bias voltage, changing from 0.19 to 0.71 percent/sec with increase in reverse bias from -1 to -8 V. These rates are tabulated in Table 4.1. Rise rate for NH_3 exposure also shows a similar increasing trend with the magnitude of the reverse bias. From Figure 4.15(c) we note that the responses measured under illumination have much faster recovery transients compared to the one measured in dark condition. This is because higher photo-generated minority carrier density near the junction under illumination allows the adsorbed NH_3 molecules (positively charged) to become quickly charge neutral and desorb. Careful observation of the recovery transients in Figure 4.15(b) indicates that the desorption transient for NO_2 becomes faster with the application of higher negative bias as noted in Table 4.1. The recovery rate increases from 1.61 to 7.43 percent/sec for the bias voltage increase from -1 to -8 V. For NH_3, the recovery rate increases only slightly from 0.04 to 0.08 percent/sec.

4.4.5   *Role of SBH in Improving Selective of Chemi-Diodes*

It follows from our experimental results that a reverse biased graphene (or another suitable 2D material)/semiconductor "Schottky type" heterojunction can be utilized as a unique platform for developing highly sensitive, fast responding and tunable sensor with a very low operational power requirement. A 2D material, such as graphene, uniquely allows the modulation of the interface SBH while analyte molecules adsorb on the outer surface. Such a SBH modulation then causes an exponential change in junction current, which imparts them extremely high sensitivity. The low power requirement of the sensor is a direct consequence of its reverse bias operation. Therefore, for optimized sensor design,

the Fermi level difference between graphene and the semiconductor needs to be carefully chosen keeping in mind the specific analyte to be detected. For example, with electron acceptor NO_2 and graphene/p-Si diode sensor combination, high sensitivity in conjunction with low operational power can be achieved if SBH is higher and the adsorbing molecules reduce the heterojunction SBH, so that the junction current changes from its usual low value to a higher value. On the other hand, for electron donor NH_3, a lower SBH is preferred so that NH_3 adsorption can increase the SBH and reduce the original higher reverse current to a significant extent which would result in very high sensor response. Our experimental results support these assertions, as illustrated in Figure 4.16(a), where the diode with larger SBH (~0.65 eV) shows a much improved response of 104 % for 10 min exposure to 20 ppm NO_2 compared to one with low SBH (~0.60 eV), which shows a relatively lower response of 65%. On the other hand, as seen in Figure 8b for NH_3, the sensor diode with smaller SBH (~0.59 eV) has a much larger response of 99% (resistivity change of 9900 %) when exposed to 550 ppm NH_3 for 10 minutes while a diode with SBH of ~0.65 eV in blue shows a response of 61% (resistivity change of 156%) only. These results are further corroborated through reverse biased I-V characteristics of diode (Figure 4.16(c,d)) taken under various gas exposures. A diode with a smaller SBH of 0.6 eV shows smaller response of 132% for 30 min exposure to 20 ppm NO_2, compared to the diode in Figure 3a with a SBH of 0.65 eV, which exhibits 716% response under similar test conditions. On the other hand, for NH_3 (550 ppm) a larger 90% change at -4 V bias with 10 minutes exposure in dark is observed for a ~0.59 eV SBH diode, compared to the larger SBH (~0.64 eV) diode in Figure 4.9(b), which shows 13% change under similar test conditions. It should also be noted that variability in the graphene sensors can be caused by

environmental issues as well as material imperfections.[34] Since the performance of the sensor depends on the equilibrium SBH, which can be strongly affected by both these factors, the various steps leading to the sensor realization (i.e. synthesis, transfer and device fabrication) need to be carefully optimized to minimize their impact.

In general, for sensors made of 3-dimensional materials, the current transient saturation happens when all possible surface states are occupied by the adsorbing molecules for a given analyte concentration. Only with 2-dimensional materials like graphene, it is possible for the Fermi level to change due to charge exchange with adsorbed molecules or with application of a reverse bias. If the charge exchange causes the Fermi level to reach the level of the defect energy states induced by the adsorbed molecules then the current transient will saturate even before all possible surface state occupation happens at a given concentration. The effect of reverse bias on the NO_2 and NH_3 sensing transients observed for our sensor clearly indicates that the later mechanism (alignment of graphene Fermi level with defect energy level) is more important in causing current transient saturation in these sensors. This offers interesting possibilities of utilizing the reverse bias as a handle to control the Fermi level and tune the sensitivity as well as the response time of sensors made of appropriate 2D material/semiconductor hetero-junctions.

4.5   Functionalization of Graphene/Si Diode

Graphene has demonstrated very high sensitivity to a large variety of polar molecules, (i.e. NO_2 and NH_3)[125] it is insensitive to most non-polar molecules, such as H_2, with which it does not exchange charge. A surface functionalization is therefore necessary for detecting these non-polar molecules. It has been demonstrated that surface functionalization of graphene by catalytically active noble metals (such as Pd and Pt) leads

to charge transfer between graphene and the metal hydride formed in presence of H_2 facilitating its detection.[126-128] There are reports on H_2 sensors utilizing epitaxial graphene,[127] graphene synthesized through chemical vapor deposition (CVD),[126] and chemically synthesized graphene nanoribbon networks,[128] which are functionalized with either Pd or Pt to impart H_2 sensitivity. Of these, only the chemically synthesized graphene nanoribbon network based sensor has so far shown good H_2 sensitivity (producing ~55% change in resistance for 40 ppm H_2), while others showed much lower sensitivity in the range of few percent for tens of ppm H_2 exposure. The higher sensitivity of the graphene nanoribbon networks[128] can be attributed to its porous structure and high specific surface area.

In general, the sensitivity of these commonly used "chemiresistor" type sensors is dependent on two factors: (i) the amount of charge exchanged from the analytes (facilitated by the functionalization layer), and (ii) the mobility of the charge carriers, since resistivity is inversely proportional to the product of mobility and charge density. The former depends on the material properties and thickness of the functionalization layer used, while the latter is controlled by the graphene quality, and more significantly, by the charge carrier scattering caused by the functionalization layer[129, 130] and substrate underneath the graphene.[115] The functionalization layer can further reduce the mobility[131], and if conducting, can also provide a parallel path for current flow thereby further reducing sensitivity. Therefore, sensing paradigms where the sensitivity of the sensor does not directly depend on the mobility of the charge carriers would be of significant interest.

Catalytically active noble metal functionalized Graphene/Si Schottky diode H_2 sensor operated in reverse bias, which takes advantage of the exponential change in current

due to SBH change, and exhibits several times higher sensitivity compared to the best performance of graphene based chemiresistor type H_2 sensor functionalized similarly. In fact, the sensitivity of the sensor allows us to reach a detection limit close to the atmospheric concentration of H_2 (~0.6 ppm).[132] The reverse bias operation also allows modulation of the Fermi level of graphene depending on the magnitude of the bias, which can lead to the tuning of sensitivity of the sensor and expansion of the dynamic range. Another advantage of the reverse bias operation of the sensor is its low power requirement due to low steady state current in the range of μA flowing in reverse bias. The fabrication of these devices followed the same processing steps as those of graphene/Si diodes described in section 4.2. Additionally as a last step different thickness (1-3 nm) of Pd and Pt were evaporated on graphene, transferred on Si, in e-beam metal deposition chamber using shadow mask.

4.6   Characterization of Pt and Pd Functionalized Chemi-Diode

4.6.1   *Raman Characterization of Functionalized Chemi-Diodes*

Raman spectra were measured on graphene transferred to the Si substrate to determine the quality of transferred graphene. Figure 4.17(a), (b), and (c) show the representative Raman spectra of graphene transferred on Si as well as Pd and Pt decorated graphene on Si. All signature peaks, D, G and 2D, along with the Si peak at 1451 cm^{-1}, can be observed. The transferred graphene layer on top of Si (figure 4.17(a)) shows intensity ratio, I_D/I_G ratio of 0.16, suggesting high quality graphene. The I_{2D}/I_G ratio of 2.47, and 2D peak full width at half maximum of 34.38 cm^{-1}, are indicative of single layer graphene. The I_D/I_G ratio of 0.32 for Pd decorated graphene (figure 4.17(b)) suggests some degradation in the quality of graphene following e-beam evaporation of 3 nm thick Pd nanoparticles for
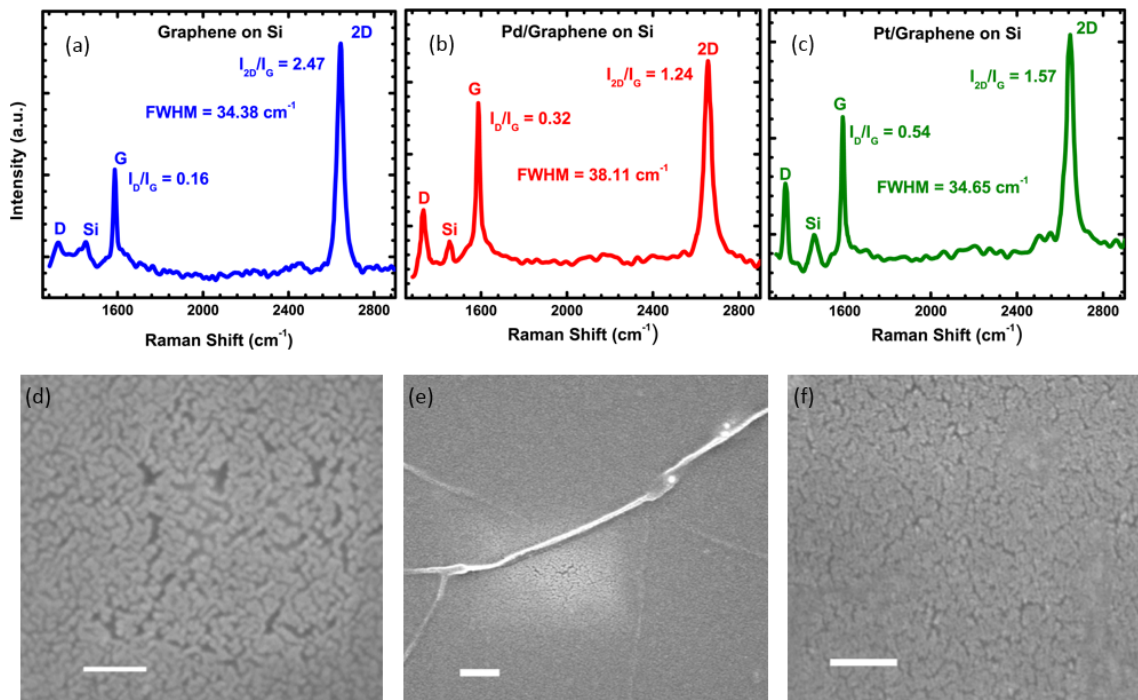
Figure 4.17 Raman spectra of (a) Graphene on p-Si, (b) Pd-deposited graphene on p-Si, (c) Pt-deposited graphene on p-Si; (d) SEM top view image of 3 nm Pd-functionalized graphene on p-Si. Scale Bar is 50 nm. (e) Zoomed out image of that shown in (d) showing graphene wrinkles. Scale Bar is 100 nm. (f) Pt-functionalized graphene on p-Si. Scale Bar is 100 nm.

functionalization. This degradation might be due to the creation of point defects in graphene by the metal atoms hitting it during e-beam evaporation. For 2 nm thick Pt functionalized graphene the I_D/I_G ratio is higher, 0.54 (figure 4.17(c)), which indicates higher defect density in the film. It is probably a consequence of higher film damage caused by heavier Pt atoms during evaporation process compared to Pd atoms. Deposited metal films typically grow on crystalline substrates through nucleation followed by grain growth. The growing grains coarsen and coalesce to form complete film coverage as metal evaporation continues. Figure 4.17(d) captures the initially formed grains of Pd on graphene/Si in a scanning electron microscopy (SEM) micrograph. Due to the small growth

duration, (~2 mins for 3 nm thickness) the Pd grains could not become large enough to coalesce completely, therefore partial coverage of Pd film is observed. A zoomed out SEM micrograph (figure 4.17(e)) at the same location shows an overall smooth coverage with a few wrinkles in the graphene layer. Figure 4.17(f) shows an SEM micrograph depicting similar coverage for deposited Pt film with 2 nm thickness.

4.6.2   *Current-Voltage Characterization of Functionalized Chemi-Diodes*

Figure 4.18(a) shows the schematic of a graphene chemiresistor sensor fabricated side by side with a graphene/Si heterojunction chemi-diode sensor with metal film functionalization layer. Optical microscopy image of the fabricated Pd-functionalized graphene/Si Schottky diode sensor is shown in Figure 4.18(b). The initial electrical
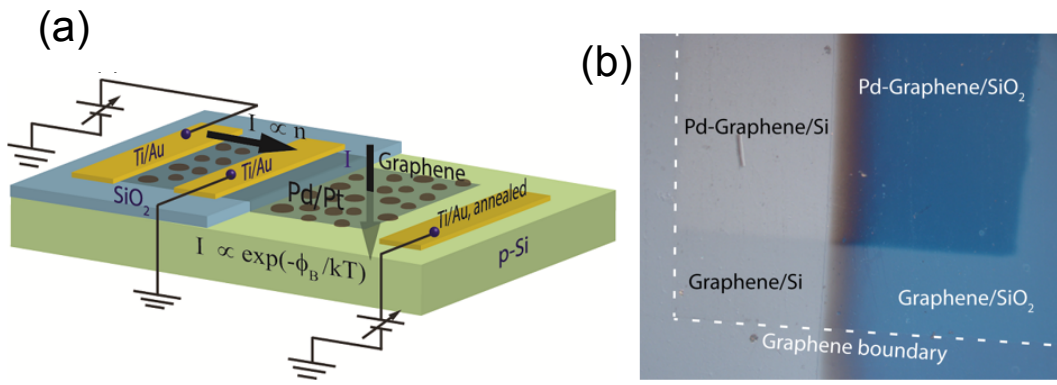
Figure 4.18 (a) Device schematic and biasing scheme of Pt/Pd functionalized graphene chemiresistor and graphene/Si Schottky diode sensors fabricated on the same chip. Gray spots indicate metal decoration. (b) Optical Image of graphene/p-Si heterojunction Schottky diode sensor with 3 nm Pd-functionalization, white dashed box approximately enclosed the graphene on both Si and SiO2, graphene is visible on SiO2, and Pd-functionalization is also showing contrast on SiO2 region covered by graphene.

characteristic of chemi-diode before Pd and Pt deposition is shown by the solid black curves in Figure 4.19(a) and (d), respectively, which exhibits typical rectifying characteristic in agreement with previous reports.[117, 133] From Figure 4.19(a), the

extrapolated ideality factor and SBH using the thermionic emission model are 1.68 and 0.648 eV, respectively, which are quite close to those reported in the literature.[121] The higher ideality factor has been attributed to various factors including SBH variation with reverse bias arising from graphene's bias dependent work function, Schottky Barrier inhomogeneity, and image charge induced SBH lowering.[118, 119, 122] Due to graphene's bias dependent work function, with the increase in reverse bias magnitude the SBH at graphene/Si interface decreases and correspondingly the reverse current increases, which is noticeable from the inset of Figure 4.19(a).

4.6.3   *Sensing Response of Functionalized diodes*

After separate deposition of 3 nm Pd and 2 nm Pt over the graphene/Si heterojunction on two different devices, both forward and reverse currents were found to increase, however, the I-V characteristics still remained distinctly Schottky (dashed blue curve in Figure 4.19(a) and (b)). The increase in current is due to the reduction in graphene/Si barrier height caused by "p-type doping" of the deposited Pd/Pt layer. Such doping of graphene by metallic thin films resulting in significant movement of the Dirac point, to both right and left (depending on the work function of the deposited metal compared to that of graphene), has been reported earlier.[134] Since the work function of Pd and Pt[135] is much higher than graphene (4.5 eV), electrons from graphene are expected to move to Pd/Pt, effectively inducing p-type doping in graphene, and causing downward movement of its Fermi level. This effect has been both theoretically predicted[136] and experimentally observed for Pt-functionalized graphene.[127] The downward movement of graphene Fermi level would then reduce the hole barrier height at the graphene/Si interface,

which was experimentally observed as the SBH changed from 0.648 to 0.546 eV after the 3 nm Pd deposition and 0.643 to 0.592 eV after 2 nm Pt deposition.
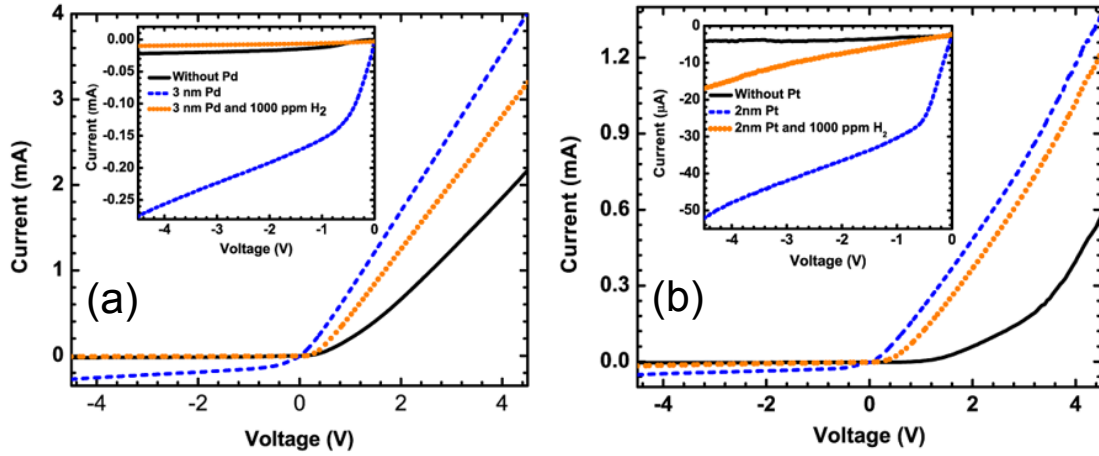
Figure 4.19 (a) Current-Voltage (I-V) characteristics of graphene/p-Si, after Pd-functionalization, and after 10 minutes exposure of the Pd-functionalized sensor to 1000 ppm H_2. (b) I-V characteristics of graphene/p-Si (black solid line), after Pt-functionalization and after 10 mins exposure of the Pt-functionalized sensor to 1000 ppm H_2.

To investigate the effect of H_2, exposure, the I-V characteristic was retaken after 10 minutes of 1000 ppm H_2 flow as shown by the orange dotted curve in Figure 4.19(a) and (b). From Figure 4.19(a), we find that both forward and reverse currents decreased in magnitude with H_2 exposure, which is expected since the SBH increased from 0.546 to 0.59 eV in case of Pd functionalized device. The SBH increase can be explained by the following mechanism: In presence of Pd or Pt, H_2 dissociates into atomic hydrogen and forms metal hydrides (PdH_x, PtH), which have lower work function then the pure Pd and Pt, respectively. [126-128] This results in electron transfer to graphene reducing its p-doping, and increasing hole barrier height at the graphene/Si interface. However, the percentage change in forward current is much smaller than the reverse current, i.e. at 4V forward bias,

the current decreased from 3.56 to 2.81 mA (21.06% change) while at -4 V bias it changed from -256.65 to -9.42 µA (96.33%).

The series resistance was also extracted from the diode forward characteristics (following the similar methods employed in reference 20), and found it to change from 1.05 (pre-exposure) to 1.32 kΩ, after exposure to 1000 ppm H_2, for Pd functionalization. In terms of resistance change, a commonly used metric for H_2 sensing, [126-128] the changes at 4 V forward and reverse bias are ~1.26 and ~27 times, respectively. Clearly, the sensitivity (defined as the ratio of change in resistance due to H_2 exposure to the initial resistance before exposure, expressed as a percentage) is dramatically enhanced in reverse bias. In addition, the power consumed is much reduced in reverse bias, only 1.03 mW, compared to 14.24 mW in forward bias, which is ~14 times higher. Reverse bias operating power can be further reduced to µW range simply by scaling down the device dimensions. However, the device dimensions should be carefully chosen to keep signal to noise ratio (SNR) acceptable since SNR degrades as the device is scaled down. A similar response is also observed for Pt functionalization, and shown in figure 2(d), the SBH changed from 0.592 to 0.623 eV with the exposure of 1000 ppm H_2 and at -4 V bias, current decreased from -47.8 to -14.94 µA (68.74% change) which is higher than the response obtained at 4 V forward bias, 1.168 to 1.1017 mA (5.68% change). The series resistance increased from 3.11 to 3.44 kΩ after exposure to 1000 ppm H_2.

4.6.4 *Functionalized diodes verses chemi resistor towards H_2 Sensitivity*

To directly compare the performances of Graphene/Si chemi-diode and graphene chemiresistor, they were fabricated side by side on the same chip (schematically shown in Figure 4.18(a)) using the same graphene sample and functionalized by 3 nm Pd and 2 nm

Pt, separately. Performances of both chemi-diode and chemiresistor sensors with 3 nm Pd functionalization upon exposure to 200 ppm H_2 for 10 minutes, at -5V bias are shown together in Figure 4.20(a). Graphene/Si diode sensor shows 122% resistance change (red curve), while the response for graphene chemiresistor is a mere 2.9% (blue curve). Thus,
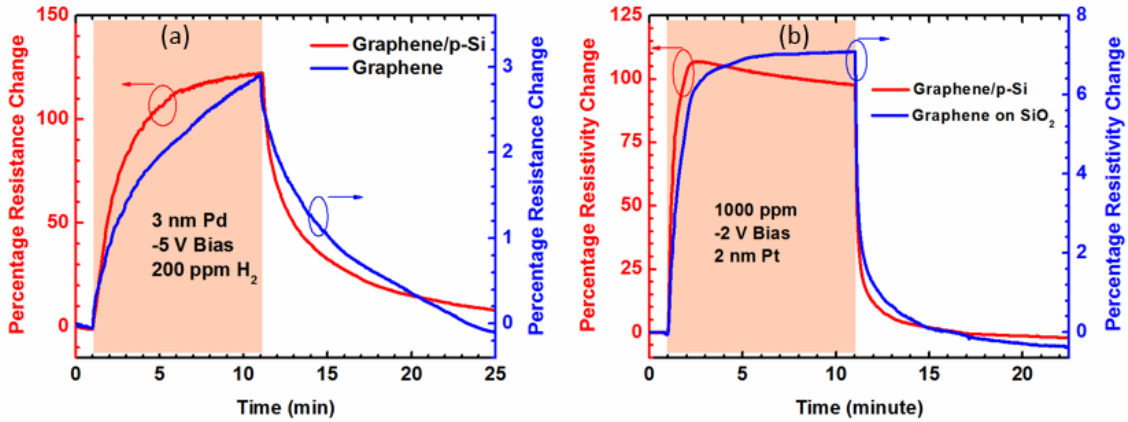
Figure 4.20 (a) Comparison between the H_2 responses for similarly functionalized graphene/p-Si chemi-diode device and graphene chemiresistor on SiO_2, fabricated on the same chip. (a) Response for 200 ppm H_2 (pink box) in case of Pd- functionalization where red one (left y-axis) is for graphene/p-Si chemi-diode and blue one (right y-axis) is for graphene chemiresistor. (b) Response for 1000 ppm H_2 (pink box) when Pt-functionalization was employed where red curve (left y-axis) is for graphene/p-Si chemi-diode and blue curve (right y-axis) is for graphene chemiresistor.

more than 40 times performance enhancement for the same exposure and bias conditions are observed for the chemi-diode sensor compared to the chemiresistor sensor. Of course, the operating power for chemiresistor is 46.425 mW, which is much higher than 64.7 μW for the diode sensor. The performance enhancement of the graphene/Si diode sensor was verified with 2 nm Pt decoration as well. The responses are shown in figure 4.20(b) for 10 minutes of 1000 ppm H_2 exposure at -2V bias condition. Once again the diode sensor showed a much higher sensitivity of 106% compared to only 7% for the chemiresistor, a 15 fold improvement.

4.6.5 *Sensitivity Tuning in Functionalized Diodes*

The performance of graphene/Si chemi-diode sensor is at least an order of magnitude improved over other graphene based H_2 sensors reported utilizing the same Pd functionalization.[126, 137] The performance is also better compared to the high-sensitivity graphene nano-ribbon based sensor,[128] which owes its high sensitivity to the porous nature and large surface area of the nanoribbons. The very high sensitivity of our sensors can be attributed to the usage of a Schottky junction to perform sensing, where the current changes exponentially with the change in SBH induced by H_2 adsorption. The Schottky diode type H_2 sensor based on Pd/semiconductor (i.e. Pd/Si[138] and Pd/InP[139]) junction has been reported earlier, utilizing various methods for depositing Pd contacts and resulting in high H_2 sensitivity. It should, however, be kept in mind that the role of the Pd layer in our sensor is that of a functionalization layer, i.e. it is not directly forming a Schottky contact with the Si, it is just allowing graphene/Si junction to respond to H_2 by facilitating its adsorption and changing the SBH. In addition, the Fermi level of the graphene layer may be altered using the reverse bias to tune the hydrogen sensitivity, a feature that is completely unique to this sensing paradigm

The response of Pt (2 nm) functionalized sensor was investigated for H_2 concentration varying from 1000 to 10 ppm at a fixed reverse bias of -4V. The sensing response illustrated in Figure 4.21(a) can be seen to vary from 103 to 5.5% as the H_2 concentration changes from 1000 to 10 ppm, for 15 minutes exposure. As mentioned earlier, an advantage of the sensor operation in reverse bias is that the bias magnitude can be varied to change the Fermi level of graphene and consequently tune the sensor response. With the higher reverse bias applied to the graphene/Si diode, the graphene Fermi level

moves further down,[119, 140] compared to the donor states induced by the metal hydride and the graphene/Si SBH will decrease. Thus, in presence of H_2, more electrons would transfer to graphene, which will in turn change the SBH by a larger amount, and the sensitivity can
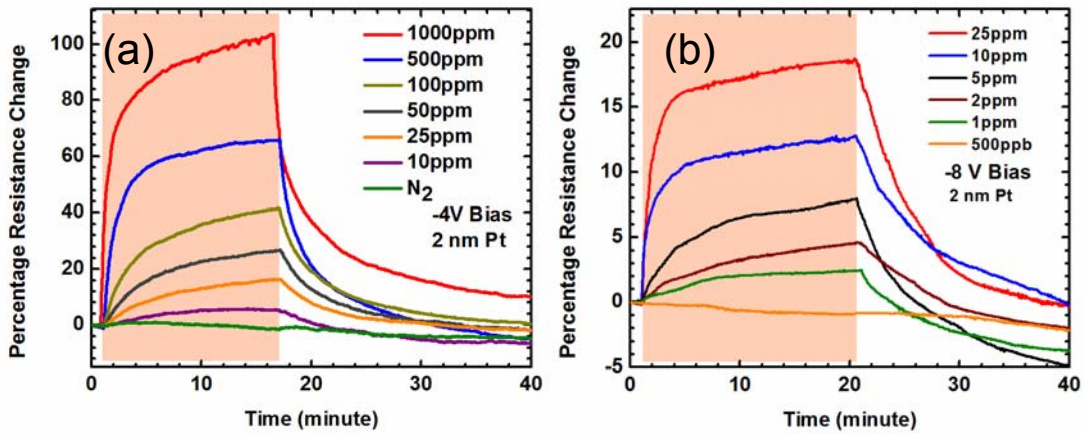
Figure 4.21 (a) Percentage resistance change of Pt-deposited graphene/p-Si device at -4 V bias for different H_2 concentration in the range of 1000-10 ppm and in N_2 environment (pink box). (b) Sensitivity enhancement at higher bias (-8V).

be expected to be higher. To substantiate the idea, the responses of were retaken at -8V bias, and shown in Figure 4.21(b). The percentage resistance change increased from 5.5% at -4V to 13% at -8V for 10 ppm H_2 exposure over the same 10 minute duration. In fact, this also enabled detection of H_2 down to 1 ppm level, which is significant, as it is close to the atmospheric background of 0.6 ppm.[132] Since, our sensing experiments were conducted in atmospheric conditions, strictly speaking the sensor response for 1 ppm H_2 exposure actually corresponds to ~0.4 ppm of H_2 concentration. Utilizing an optimized Pd coating the sensor sensitivity was significantly enhanced (explained later), which highlights the possibility of performing detection of H_2 in the ppb level in a controlled environment. These results clearly indicate that the sensitivity of the graphene/Si chemi-

diode sensor is significantly tunable with magnitude of reverse bias, which is not possible with typical metal/semiconductor diode sensors.

4.6.6   Functionalization: Pd verses Pt

To compare the performance of Pd and Pt in terms of H_2 sensitivity in functionalized chemi-diodes, 1 nm of Pt and Pd were deposited on two different diodes and the sensor responses upon exposure to 1000 ppm H_2 were recorded. For the 1 nm Pt deposited device the response varied from 27.5 to 77.5% for the aforementioned voltage
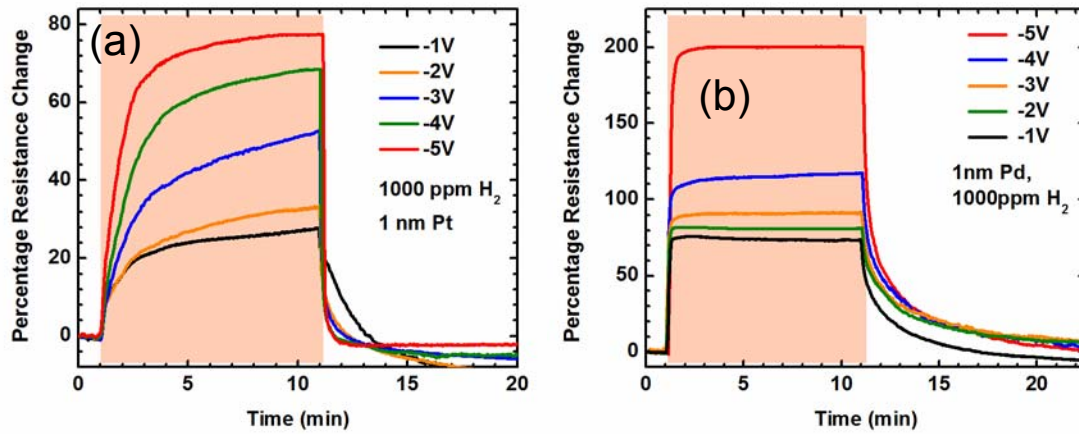
Figure 4.22 (a) Bias dependence of sensor response for 1000 ppm H_2 (pink box) as the voltage was changed from -1 to -5 V for Pt-functionalized device. (b) Sensitivity enhancement at higher bias (-8V). Bias dependence of sensor response for 1000 ppm H_2 (pink box) as the voltage was changed from -1 to -5 V for Pd-functionalized device.

range, with higher rise rate observed for the larger reverse bias voltages, which also resulted in higher peak response (Figure 4.22(a)). Since Pd has a 3 times higher H_2 solubility compared to Pt (while having same H_2 diffusion coefficient),[141] it causes a larger reduction in p-type doping upon H_2 adsorption, which can result in a larger increase in SBH, hence Pd functionalized graphene/Si chemi-diode sensors are expected to show better response than Pt functionalized ones. Indeed for the 1 nm Pd functionalized device

the response varied from 200% at -5V to 74% at -1 V (Figure 4.22(b)), which is ~2.5 times

higher compared to 1 nm Pt functionalized sensor for the same applied bias (Figure

4.22(a)). Additionally, there are significant differences between the Pt and Pd coated

devices in terms of the transient responses. For the former, the response time is much

slower than the later, while the recovery time is somewhat faster. This is however expected

due to higher H_2 solubility in Pd, which leads to higher concentration in the Pd
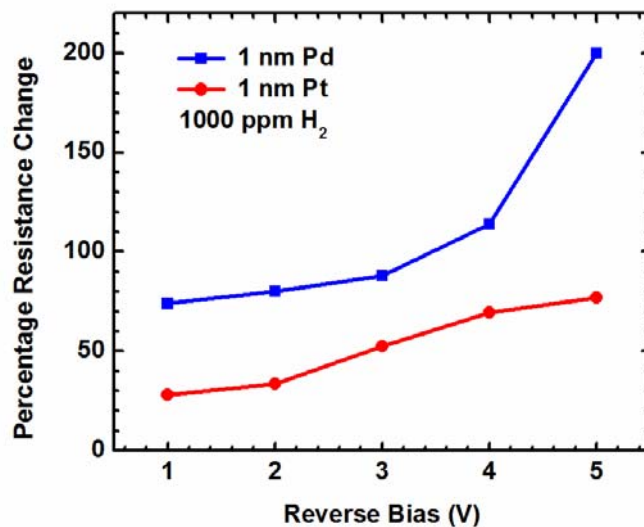
Figure 4.23 Comparison between the responses for Pt and Pd-functionalized
sensor at different reverse bias voltages.

functionalization layer, which would make the response time faster but the recovery time

a little slower. The sensitivity for Pt and Pd functionalized (1 nm thick metal coating)

devices are compared in Figure 4.23 for various reverse bias voltages from where it is

apparent that the later always show better sensitivity to H_2 irrespective of the voltage bias.

Interestingly, with increasing reverse bias, the sensitivity of the Pd–coated sensor keeps

increasing sharply, while that of the Pt-coated sensor displays a saturating trend.

4.6.7 H₂ Concentration Dependence of Pd Functionalized Chemi-Diodes

Thicker Pd layer is expected to improve the H_2 sensitivity in two ways. First, it would lower the graphene Fermi level by a larger magnitude due to higher p-type doping, which would improve sensitivity as discussed below. Second, it would adsorb higher
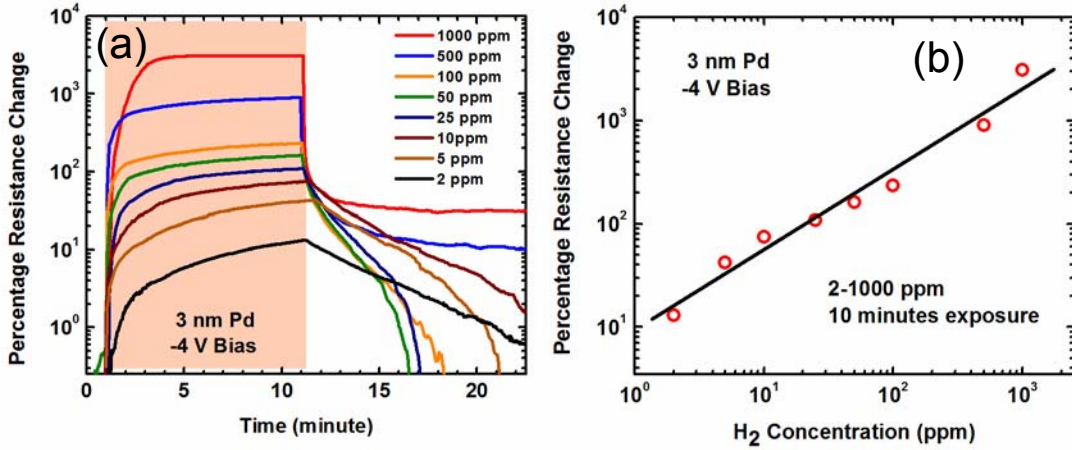
Figure 4.24 (a) Responses of 3 nm Pd functionalized graphene/p-Si device for H_2 concentration ranging from 1000 to 2 ppm (pink box) for 10 minutes exposure. (b) Sensor response as a function of H_2 concentration plotted in log-log scale. The solid straight line shows a least square fit to the data.

volume of H_2, and cause higher movement of the graphene Fermi level, thereby resulting in higher sensitivity. In fact, a previous study on graphene chemiresistor based H_2 sensor[137] indicate that 3 nm Pd functionalization layer provides maximum sensitivity to H_2. From the I-V characteristics we find that higher Pd thickness of 3 nm changes the graphene/Si SBH by 102 meV compared to 61 meV caused by 1 nm Pd deposition. This means the graphene Fermi level moves further down by 3 nm Pd deposition, which causes the SBH to be lower (lower resistance) initially, so with H_2 adsorption, the relative change in resistance becomes much larger. Sensing experiments were carried out using the 3 nm Pd functionalized chemi-diodes, with the H_2 concentration varying from 1000 to 2 ppm,

with exposure duration of 10 minutes, at a fixed reverse bias of -4 V. We find from Figure 4.24(a) that sensitivity changes from 13.55% to 3088% as the H_2 concentration increases from 2 to 1000 ppm. The response time is increased from 90 sec to 270 sec as the H_2 concentration changes from 1000 to 2 ppm. The recovery times are very fast, taking only 1 sec to recover to 50% of the maximum resistance change for 1000 ppm H_2. Interestingly, the full recovery times are faster for the smaller concentrations of H_2 as can be seen from Figure 4.24(a), with complete recovery observed within a few minutes for most concentrations other than 500 and 1000 ppm. This is probably due to the larger amount of H_2 adsorption by thicker Pd layer (3nm) functionalized chemi-diode compared to that of 1nm Pd functionalized graphene/p-Si device, which recovered completely as shown in Figure 4.22(b). The plot of sensitivity versus H_2 concentration (Figure 4.24(b)) indicates that the sensitivity in these sensors varies almost linearly with the H_2 concentration when both of them are plotted in logarithmic scale. The work function change of the Pd layer (and hence the SBH) is expected to vary linearly with log of H_2 concentration,[139] while the sensor current, which controls the sensitivity, varies exponentially with the SBH. Thus, the log-log relationship between H_2 concentration and sensitivity is expected to be linear as observed in figure 4.24(b). It is noteworthy that this exponential behavior is different from that obtained previously from graphene and graphene nanoribbon network based chemiresistive H_2 sensors, where the sensitivity got saturated at higher H_2 concentration (plotted in log scale).[126, 128, 142] This difference in the sensing response, is however expected, and follows from the difference in the detection principles of the chemiresistor and the proposed reverse biased chemi-diode sensor as discussed above.

In summary the chemical sensitivity improvements in graphene devices were obtained by use of a back-gate bias, structure defects in graphene and finally by use of thermionic transport in graphene/Si based Schottky devices or chemi-diodes. These chemi-diodes showed huge sensitivity enhancements towards polar molecules such as NO_2 and NH_3 with additional benefit of tunable sensitivity and orders of magnitude low power operation. The extent of graphene chemi-diodes towards sensing nonpolar molecules such as H_2 has been facilitated by functionalization of Pd & Pt nanoparticles. These functionalized chemi-diodes were found to offer all the same advantages of a graphene chemi-diodes and appear to outperform many of the existing graphene based H_2 sensors. In the fifth and final chapter the summary of this thesis will be presented along with some of the fascinating future directions.

CHAPTER 5

CONCLUSIONS AND FUTURE DIRECTIONS

This thesis explored the best possible process parameters to grow low defect monolayer graphene in a home-build chemical vapor deposition unit. The optimized parameters were obtained by a series of growth and characterization steps which involved learning from day to day growth, and understanding growth mechanism from most recent publications and incorporating these knowledge into improving the CVD of graphene. Graphene transfer process was developed to fabricate devices on any desired substrates. The graphene based device processing was developed and optimized. Graphene based devices such as FETs, Schottky diodes were fabricated along with various test structures such as TLM pads and Hall bars. Various characterization was performed, on graphene and devices, such as Raman spectroscopy, IV, CV, Hall to access material quality, mobility, carrier concentration, sheet resistance, specific contact resistivity, SBH etc. Graphene based chemical sensor development was pursued thereafter. Graphene chem-FETs were used to tune sensitivity and selectivity and graphene chemi-diode were utilized to enhance sensitivity by an order of magnitude for polar molecules such as NO_2 and NH_3, and noble metal functionalization was used to sense non-polar molecules such as H_2.

5.1   Summary of This Work

Amongst many amazing properties of graphene the one that makes it very promising sensing material is the ability to change the carrier concentration of graphene by electrical, chemical and optical means. Since carrier concentration is linked to Fermi level or work function of graphene, therefore new device paradigm such as barristor, and sensing paradigm such graphene Schottky diode can be realized where the working principle is modulation of carrier transport across a Schottky barrier which is alter by modulation of graphene Fermi level by electrical or chemical means. The latter device has been one of the highlight of this work. In order to realize the newer capability for practical device a reliable method of good quality, large area graphene is needed.

In chapter 2 such a reliable method of producing good quality, large area graphene for practical device application has been investigate by chemical vapor deposition technique. The CVD reactor was built by assembling different components such as quartz tube chamber, horizontal split furnace, mechanical pump, MFCs and pressure gauges. The optimized process parameter were obtained by understanding growth mechanism and by performing series of growth on different types of substrates and under different growth conditions. Cu foils were found to be ideal substrate to grow monolayer graphene. Due to very low solubility of C in Cu the graphene growth is surface mediated and essentially self-limited resulting in monolayer graphene which is also independent of the cooling rate as against Ni based growth. Therefore sophisticated hardware for controlling the cooling rate is not essential for growth on copper. The good quality, low defect, large area, monolayer graphene was successfully grown in routine basis using optimized process parameters as

suggested from low I_D/I_G (0.1-0.2) and high I_{2D}/I_G (3 to 4) and small 2D FWHM (<30 cm$^-$ ^{1}) of Raman spectrum of as-grown graphene.

In chapter 3 the graphene and graphene based device processing were successfully developed. The graphene based chemical sensor development was achieved which also led to understanding the role and physics of adsorbate induced defect level in tuning the sensitivity of graphene chem-FET by use of a back-gate bias. CVD grown graphene on Cu is needed to be transferred on a desired substrate for device fabrication. The transfer was optimized by coating layer of polymer on graphene congaing Cu foils and then dissolving the Cu in its etchant and scooping the graphene\polymer composite on a desired substrate. In sensor development work it was demonstrated that molecular doping of graphene is electrically tunable in a back-gated field effect transistor. The charge transfer doping decreased monotonically for a typical p-type gaseous dopant NO_2, as the back gate voltage was reduced from 5 to -45 V, while for an n-type dopant NH_3, the reverse was observed. A significant reduction in NO_2 adsorption induced conductivity change from 26.1% to 0 was observed over this voltage range, while for NH_3 the conductivity changed from 0 to 7.6%, which clearly demonstrates the utility of this technique in enhancing sensitivity and selectivity of molecular detection. Our proposed model for charge transfer, involving relative positions of the Fermi level and the adsorption induced defect level, yielded 320 meV as the acceptor energy level for NO_2, in agreement with earlier results.

Chapter 4 essentially deals with sensitivity enhancement of graphene based chemical sensors for practical applications and increasing the utility of graphene based sensors with use of functionalization layer to sense nonpolar molecules such as H_2. Use of defective graphene enabled sensitivity to go up from 20% to 65 % range it still remains

119

fairly low because of liner dependence of change in current on number of adsorbed molecules on graphene surface in case of both FET and highly defective graphene. However in case of graphene/p-Si heterostructure molecular adsorption on its surface to directly alter graphene/Si interface barrier height, thus can affect the junction current exponentially when operated in reverse bias which results in ultrahigh sensitivity. By operating the device in reverse bias, the work function of graphene, and hence the barrier height at the graphene/Si heterointerface, can be controlled by the bias magnitude, leading to a wide tunability of the molecular detection sensitivity. Such sensitivity control is also possible by carefully selecting the graphene/Si heterojunction Schottky barrier height. Compared to a conventional graphene amperometric sensor fabricated on the same chip, the proposed sensor demonstrated 13 times higher sensitivity for NO_2 and 3 times higher for NH_3 in ambient conditions, while consuming ~500 times less power for same magnitude of applied voltage bias. The sensing mechanism based on heterojunction Schottky barrier height change has been confirmed using capacitance-voltage measurements. The use functionalization layer such as Pt or Pd offer similar advantage in sensing non polar H_2 by graphene Schottky diodes. Pt and Pd functionalized graphene/p-Si heterojunction chemi-diode H_2 sensor demonstrated very high sensitivity, down to sub-ppm level of H_2.[143] These heterojunction diode sensors show at least an order of magnitude higher response compared to the graphene based chemiresistor type sensors for both Pd and Pt-functionalization.

5.2   Future Outlook

5.2.1   SBH Tuning for Selectivity

The graphene/Si heterostructure chemi-diodes have demonstrated impressive performance in sensing NO_2 and NH_3. The SBH of these device plays very important role in acceptor or donor type polar molecules. We also demonstrated in Figure 4.16 that large
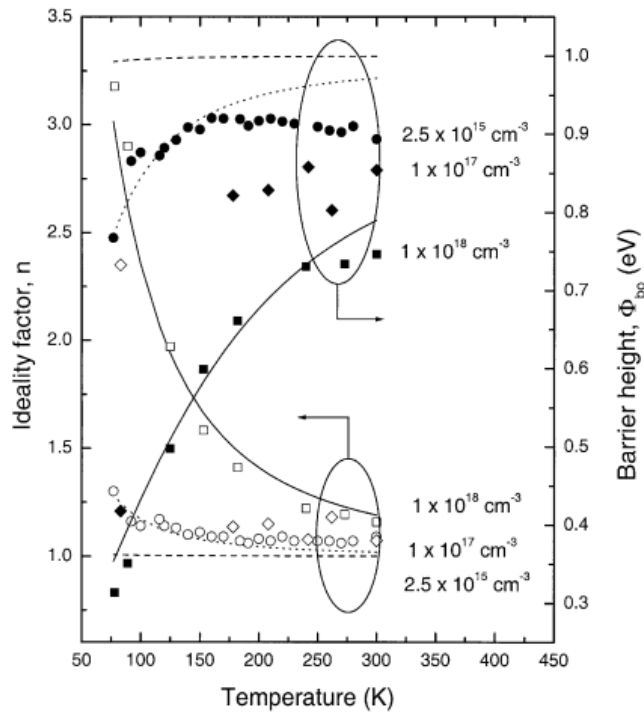
Figure 5.1 (a) Doping dependent SBH in Au/n-GaAs Schottky diodes [144].

SBH chemi-diode is better sensor for hole donating NO_2 which serves to decrease SBH whereas smaller SBH diode is better NH_3 sensor which serves to increase SBH. However we did not have much control on getting a desired SBH in graphene/p-Si chemi-diodes. The possible causes of unpredictive SBH could be non-uniform doping of p-Si, as suggested by manufacturer in resistivity range of 1-10 Ω-cm, or a possibility of native oxide growth just before graphene transfer.

In principle the SBH in a Schottky diode is determined by difference between metal work function and semiconductor electron affinity. Therefore the SBH should only be affected by choosing a different metal if the semiconductor is fixed. However it was reported that the SBH in Au/n-GaAs Schottky diodes was indeed dependent upon doping concentration of GaAs (Figure 5.1) and the effect was very pronounced upon lower temperature.[144] Therefore Schottky diode of graphene with semiconductor as GaAs or Si with different doping profile can be fabricated to get a desire SBH which many make is selective to NO_2 or NH_3 based upon a given SBH.

5.2.2 *Flexible Transparent Heterostructure*

Two dimensional (2D) materials, due to their atomically thin nature and exceptional material properties, have emerged as the ultimate building blocks for nanoelectromechanical systems (NEMS), flexible transparent electronic devices, bio-
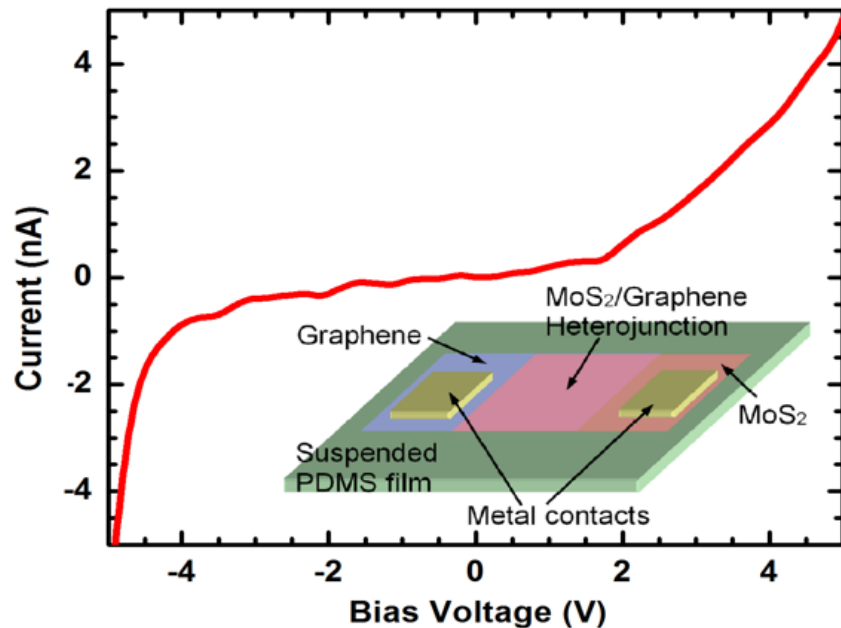
Figure 5.2 Graphene/MoS_2 heterojunction diode characteristics. Inset shows the device schematics

122

implantable devices and wearable sensors. Graphene has already established itself in different applications. A hetero structure of graphene with other 2D material can offer new properties and application which may not be obtained by the individual 2D material by itself. For instance graphene and MoS_2 heterostructure can be fabricated on a flexible substrate for chemical sensing application which may take advantage of sensing ability of graphene as in case of a chemi-diode. A flexible all 2D barristor device consisting of graphene/MoS_2 heterostructure and 2D BN as gate insulator can be fabricated on flexible substrate that can offer very high on/off current ratio. Figure 5.2 shows schematic of graphene/MoS_2 all 2D transparent Schottky diode on PDMS substrate along with preliminary IV which shows Schottky characteristics.

5.2.3 *Suspended Graphene Structures*

Suspended graphene structures takes graphene into interesting area of MEMS and NEMS devices which have applications in graphene based resonator and voltage controlled
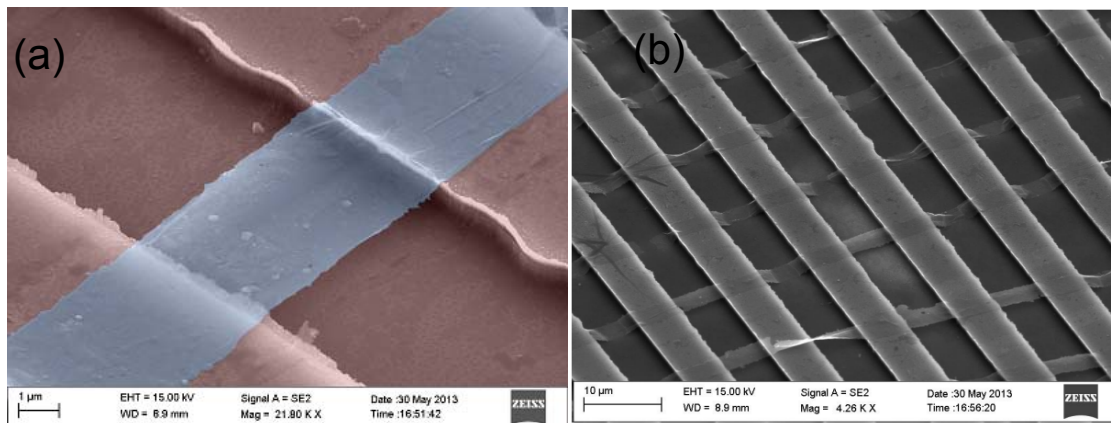
Figure 5.3 (a) Suspended CVD graphene in bridge structure on top of SiO_2/Si trench. (b) SEM image of the suspended graphene bridge array showing poor yield of the suspended structure.

oscillators have resonance frequency of oscillation in 100s of MHz range. Their electrical actuation would be ideal to replace some of the quartz based oscillators which have large

footprints in devices. Another unique application of suspended graphene based structure could be IR sensing where a pixel element would compose of suspended graphene/polymer bi-layer such as graphene/parylene. Suspended graphene structures were successfully fabricated from the CVD graphene by 4 steps that involves making a patterned trench structure on SiO_2/Si substrate, patterning of graphene on Cu foils into elongated stripes, transfer of patterned graphene on top of patterned SiO_2/Si substrate and then carefully drying the suspended graphene in a critical point dryer. Figure 5.3(a) shows SEM micrograph of a suspended graphene on top of SiO_2 graphene having Ti/Au contacts. The false coloration is used for better contrast. Figure 5.3(b) captures an array of such devices with poor yield.

Future work will involves design and fabrication of chrome mask so that individual devices can be accessed and characterized. Improving yield of such device in another area of work so that more devices are available for characterization. Most of the graphene MEMS structure are characterized in high vacuum to avoid dampening of amplitude, since these devices vibrates at very high frequency range of 100 MHz. Heterodyning is widely used characterization technique for determining resonance frequency of carbon nanotubes and also been used in suspended graphene devices. We can also characterized the resonance frequency in the same fashion in a high vacuum setup. Next the graphene\polymer suspended structures can be fabrication by similar fabrication method and can be characterized for IR sensing capability.

REFERENCES

[1]   K. S. Novoselov, A. K. Geim, S. Morozov, D. Jiang, Y. Zhang, S. Dubonos*, et al.*, "Electric field effect in atomically thin carbon films," *Science,* vol. 306, pp. 666-669, 2004.

[2]   A. K. Geim and K. S. Novoselov, "The rise of graphene," *Nat Mater,* vol. 6, pp. 183-191, 03//print 2007.

[3]   W. Andreoni, *The physics of fullerene-based and fullerene-related materials* vol. 23: Springer, 2000.

[4]   R. Saito, G. Dresselhaus, and M. S. Dresselhaus, *Physical properties of carbon nanotubes* vol. 4: World Scientific, 1998.

[5]   A. H. Castro Neto, F. Guinea, N. M. R. Peres, K. S. Novoselov, and A. K. Geim, "The electronic properties of graphene," *Reviews of Modern Physics,* vol. 81, pp. 109-162, 01/14/ 2009.

[6]   N. Peres, "The transport properties of graphene," *Journal of physics. Condensed matter: an Institute of Physics journal,* vol. 21, pp. 323201-323201, 2009.

[7]   P. R. Wallace, "The band theory of graphite," *Physical Review,* vol. 71, p. 622, 1947.

[8]   M. Freitag, "Graphene: nanoelectronics goes flat out," *Nature nanotechnology,* vol. 3, pp. 455-457, 2008.

[9]   N. Ashcroft and N. Mermin, "Solid State Physics (Brooks Cole, 1976)," *Cited on,* p. 26.

[10]   Z. Chen and J. Appenzeller, "Mobility extraction and quantum capacitance impact in high performance graphene field-effect transistor devices," in *Electron Devices Meeting, 2008. IEDM 2008. IEEE International*, 2008, pp. 1-4.

[11]   E. H. Hwang and S. Das Sarma, "Acoustic phonon scattering limited carrier mobility in two-dimensional extrinsic graphene," *Physical Review B,* vol. 77, p. 115449, 03/27/ 2008.

[12]   S. Adam, E. Hwang, V. Galitski, and S. D. Sarma, "A self-consistent theory for graphene transport," *Proceedings of the National Academy of Sciences,* vol. 104, pp. 18392-18397, 2007.

[13]   T. Stauber, N. Peres, and F. Guinea, "Electronic transport in graphene: A semiclassical approach including midgap states," *Physical Review B,* vol. 76, p. 205423, 2007.

[14]   J.-H. Chen, C. Jang, S. Xiao, M. Ishigami, and M. S. Fuhrer, "Intrinsic and extrinsic performance limits of graphene devices on SiO2," *Nature nanotechnology,* vol. 3, pp. 206-209, 2008.

[15]   X. Du, I. Skachko, F. Duerr, A. Luican, and E. Y. Andrei, "Fractional quantum Hall effect and insulating phase of Dirac electrons in graphene," *Nature,* vol. 462, pp. 192-195, 2009.

[16]   K. Bolotin, K. Sikes, J. Hone, H. Stormer, and P. Kim, "Temperature-dependent transport in suspended graphene," *Physical review letters,* vol. 101, p. 096802, 2008.

[17]   Y. Zhang, V. W. Brar, C. Girit, A. Zettl, and M. F. Crommie, "Origin of spatial charge inhomogeneity in graphene," *Nature Physics,* vol. 5, pp. 722-726, 2009.

[18]   J.-H. Chen, C. Jang, S. Adam, M. Fuhrer, E. Williams, and M. Ishigami, "Charged-impurity scattering in graphene," *Nature Physics,* vol. 4, pp. 377-381, 2008.

[19]   R. Nair, P. Blake, A. Grigorenko, K. Novoselov, T. Booth, T. Stauber*, et al.*, "Fine structure constant defines visual transparency of graphene," *Science,* vol. 320, pp. 1308-1308, 2008.

[20]   F. Bonaccorso, Z. Sun, T. Hasan, and A. Ferrari, "Graphene photonics and optoelectronics," *Nature Photonics,* vol. 4, pp. 611-622, 2010.

[21]   C. Lee, X. Wei, J. W. Kysar, and J. Hone, "Measurement of the elastic properties and intrinsic strength of monolayer graphene," *science,* vol. 321, pp. 385-388, 2008.

[22]   S. Rumyantsev, L. Guanxiong, R. A. Potyrailo, A. A. Balandin, and M. S. Shur, "Selective Sensing of Individual Gases Using Graphene Devices," *Sensors Journal, IEEE,* vol. 13, pp. 2818-2822, 2013.

[23]   S. Rumyantsev, G. Liu, W. Stillman, M. Shur, and A. A. Balandin, "Electrical and noise characteristics of graphene field-effect transistors: ambient effects, noise sources and physical mechanisms," *Journal of Physics: Condensed Matter,* vol. 22, p. 395302, 2010.

[24]   F. Schedin, A. K. Geim, S. V. Morozov, E. W. Hill, P. Blake, M. I. Katsnelson*, et al.*, "Detection of individual gas molecules adsorbed on graphene," *Nat Mater,* vol. 6, pp. 652-655, 09//print 2007.

[25]   Y. Iyechika, "Application of graphene to high-speed transistors: expectations and challenges," *Sci. Technol. Trends,* vol. 37, pp. 76-92, 2010.

[26]   (20 July 2014). *Graphene*. Available: http://www.megagraphite.com/graphene

[27]   K. Novoselov, D. Jiang, F. Schedin, T. Booth, V. Khotkevich, S. Morozov*, et al.*, "Two-dimensional atomic crystals," *Proceedings of the National Academy of Sciences of the United States of America,* vol. 102, pp. 10451-10453, 2005.

[28]   C. Soldano, A. Mahmood, and E. Dujardin, "Production, properties and potential of graphene," *Carbon,* vol. 48, pp. 2127-2150, 2010.

[29]   Y. Hernandez, V. Nicolosi, M. Lotya, F. M. Blighe, Z. Sun, S. De*, et al.*, "High-yield production of graphene by liquid-phase exfoliation of graphite," *Nature Nanotechnology,* vol. 3, pp. 563-568, 2008.

[30]   D. A. Dikin, S. Stankovich, E. J. Zimney, R. D. Piner, G. H. Dommett, G. Evmenenko, *et al.*, "Preparation and characterization of graphene oxide paper," *Nature,* vol. 448, pp. 457-460, 2007.

[31]   E. Rollings, G. H. Gweon, S. Y. Zhou, B. S. Mun, J. L. McChesney, B. S. Hussain*, et al.*, "Synthesis and characterization of atomically thin graphite films on a silicon carbide substrate," *Journal of Physics and Chemistry of Solids,* vol. 67, pp. 2172-2177, 9// 2006.

[32]   W. A. de Heer, C. Berger, M. Ruan, M. Sprinkle, X. Li, Y. Hu*, et al.*, "Large area and structured epitaxial graphene produced by confinement controlled sublimation of silicon carbide," *Proceedings of the National Academy of Sciences,* September 29, 2011 2011.

[33]   C. Berger, Z. Song, T. Li, X. Li, A. Y. Ogbazghi, R. Feng*, et al.*, "Ultrathin Epitaxial Graphite: 2D Electron Gas Properties and a Route toward Graphene-based Nanoelectronics," *The Journal of Physical Chemistry B,* vol. 108, pp. 19912-19916, 2004/12/01 2004.

[34]   S. Shivaraman, M. V. S. Chandrashekhar, J. Boeckl, and M. Spencer, "Thickness Estimation of Epitaxial Graphene on SiC Using Attenuation of Substrate Raman Intensity," *Journal of Electronic Materials,* vol. 38, pp. 725-730, 2009/06/01 2009.

[35]   Y. Wu, P. Ye, M. A. Capano, Y. Xuan, Y. Sui, M. Qi*, et al.*, "Top-gated graphene field-effect-transistors formed by decomposition of SiC," *Applied Physics Letters,* vol. 92, pp. 092102-092102-3, 2008.

[36]   K. V. Emtsev, A. Bostwick, K. Horn, J. Jobst, G. L. Kellogg, L. Ley*, et al.*, "Towards wafer-size graphene layers by atmospheric pressure graphitization of silicon carbide," *Nat Mater,* vol. 8, pp. 203-207, 03//print 2009.

[37]   S. Park and R. S. Ruoff, "Chemical methods for the production of graphenes," *Nature nanotechnology,* vol. 4, pp. 217-224, 2009.

[38]   R. Muñoz and C. Gómez-Aleixandre, "Review of CVD Synthesis of Graphene," *Chemical Vapor Deposition,* vol. 19, pp. 297-322, 2013.

[39]   D. K. Schroder, *Semiconductor material and device characterization*: John Wiley & Sons, 2006.

[40] J. W. Kuehn and S. O. Konorov, "Raman Spectroscopy – a powerful tool in gem identification," presented at the The 3rd International Gem & Jewelry Conference (GIT2012), Bangkok Thailand and Pailin Cambodia, 2012.

[41] A. Eckmann, A. Felten, A. Mishchenko, L. Britnell, R. Krupke, K. S. Novoselov, *et al.*, "Probing the Nature of Defects in Graphene by Raman Spectroscopy," *Nano Letters,* vol. 12, pp. 3925-3930, 2012/08/08 2012.

[42] L. Malard, M. Pimenta, G. Dresselhaus, and M. Dresselhaus, "Raman spectroscopy in graphene," *Physics Reports,* vol. 473, pp. 51-87, 2009.

[43] A. C. Ferrari and D. M. Basko, "Raman spectroscopy as a versatile tool for studying the properties of graphene," *Nature nanotechnology,* vol. 8, pp. 235-246, 2013.

[44] M. S. Dresselhaus, A. Jorio, M. Hofmann, G. Dresselhaus, and R. Saito, "Perspectives on carbon nanotubes and graphene Raman spectroscopy," *Nano letters,* vol. 10, pp. 751-758, 2010.

[45] A. Ferrari, J. Meyer, V. Scardaci, C. Casiraghi, M. Lazzeri, F. Mauri, *et al.*, "Raman spectrum of graphene and graphene layers," *Physical review letters,* vol. 97, p. 187401, 2006.

[46] Y. Kawashima and G. Katagiri, "Fundamentals, overtones, and combinations in the Raman spectrum of graphite," *Physical Review B,* vol. 52, p. 10053, 1995.

[47] R. Nemanich and S. Solin, "First-and second-order Raman scattering from finite-size crystals of graphite," *Physical Review B,* vol. 20, p. 392, 1979.

[48] D. R. Lenski and M. S. Fuhrer, "Raman and optical characterization of multilayer turbostratic graphene grown via chemical vapor deposition," *Journal of Applied Physics,* vol. 110, p. 013720, 2011.

[49] L. Cancado, K. Takai, T. Enoki, M. Endo, Y. Kim, H. Mizusaki, *et al.*, "General equation for the determination of the crystallite size L a of nanographite by Raman spectroscopy," *Applied Physics Letters,* vol. 88, pp. 163106-163106-3, 2006.

[50] L. G. Cançado, A. Jorio, E. M. Ferreira, F. Stavale, C. Achete, R. Capaz, *et al.*, "Quantifying defects in graphene via Raman spectroscopy at different excitation energies," *Nano letters,* vol. 11, pp. 3190-3196, 2011.

[51] C. Mattevi, H. Kim, and M. Chhowalla, "A review of chemical vapour deposition of graphene on copper," *Journal of Materials Chemistry,* vol. 21, pp. 3324-3334, 2011.

[52] X. Li, W. Cai, L. Colombo, and R. S. Ruoff, "Evolution of Graphene Growth on Ni and Cu by Carbon Isotope Labeling," *Nano Letters,* vol. 9, pp. 4268-4272, 2009/12/09 2009.

[53] A. A. Balandin, S. Ghosh, W. Bao, I. Calizo, D. Teweldebrhan, F. Miao, *et al.*, "Superior thermal conductivity of single-layer graphene," *Nano letters,* vol. 8, pp. 902-907, 2008.

[54] Y. Hao, M. Bharathi, L. Wang, Y. Liu, H. Chen, S. Nie, *et al.*, "The role of surface oxygen in the growth of large single-crystal graphene on copper," *Science,* vol. 342, pp. 720-723, 2013.

[55] J. Baringhaus, M. Ruan, F. Edler, A. Tejeda, M. Sicot, A. Taleb-Ibrahimi, *et al.*, "Exceptional ballistic transport in epitaxial graphene nanoribbons," *Nature,* vol. 506, pp. 349-354, 2014.

[56] J.-U. Lee, D. Yoon, and H. Cheong, "Estimation of Young's modulus of graphene by Raman spectroscopy," *Nano letters,* vol. 12, pp. 4444-4448, 2012.

[57] A. A. Balandin, "Low-frequency 1/f noise in graphene devices," *Nature nanotechnology,* vol. 8, pp. 549-555, 2013.

[58] C. Chen, "Graphene Nanoelectromechanical Systems," *Proceedings of the IEEE,* vol. 101, 2013.

[59] E. V. Castro, H. Ochoa, M. I. Katsnelson, R. V. Gorbachev, D. C. Elias, K. S. Novoselov, *et al.*, "Limits on Charge Carrier Mobility in Suspended Graphene due to Flexural Phonons," *Physical Review Letters,* vol. 105, p. 266601, 12/22/ 2010.

[60]   J. S. Bunch, A. M. Van Der Zande, S. S. Verbridge, I. W. Frank, D. M. Tanenbaum, J. M. Parpia*, et al.*, "Electromechanical resonators from graphene sheets," *Science,* vol. 315, pp. 490-493, 2007.

[61]   S. Shivaraman, R. A. Barton, X. Yu, J. Alden, L. Herman, M. Chandrashekhar*, et al.*, "Free-standing epitaxial graphene," *Nano letters,* vol. 9, pp. 3100-3105, 2009.

[62]   A. M. v. d. Zande, R. A. Barton, J. S. Alden, C. S. Ruiz-Vargas, W. S. Whitney, P. H. Pham*, et al.*, "Large-scale arrays of single-layer graphene resonators," *Nano letters,* vol. 10, pp. 4869-4873, 2010.

[63]   K. W. C. Lai, N. Xi, H. Chen, B. Song, and L. Chen, "The Development of an Infrared Camera Using Graphene: Achieving Efficient High-Resolution Infrared Images," *Nanotechnology Magazine, IEEE,* vol. 6, pp. 4-7, 2012.

[64]   J. Yan, M. Kim, J. Elle, A. Sushkov, G. Jenkins, H. Milchberg*, et al.*, "Dual-gated bilayer graphene hot-electron bolometer," *Nature nanotechnology,* vol. 7, pp. 472-478, 2012.

[65]   N. G. Kalugin, L. Jing, W. Bao, L. Wickey, C. Del Barga, M. Ovezmyradov*, et al.*, "Graphene-based quantum Hall effect infrared photodetector operating at liquid Nitrogen temperatures," *Applied Physics Letters,* vol. 99, pp. 013504-013504-3, 2011.

[66]   Y. Kawano, "Wide-band frequency-tunable terahertz and infrared detection with graphene," *Nanotechnology,* vol. 24, p. 214004, 2013.

[67]   C. Chen, S. Rosenblatt, K. I. Bolotin, W. Kalb, P. Kim, I. Kymissis*, et al.*, "Performance of monolayer graphene nanomechanical resonators with electrical readout," *Nature nanotechnology,* vol. 4, pp. 861-867, 2009.

[68]   C. Chen, S. Lee, V. V. Deshpande, G.-H. Lee, M. Lekas, K. Shepard*, et al.*, "Graphene mechanical oscillators with tunable frequency," *Nature nanotechnology,* vol. 8, pp. 923-927, 2013.

[69]   Y. G. Semenov, J. M. Zavada, and K. W. Kim, "Graphene spin capacitor for magnetic field sensing," *Applied Physics Letters,* vol. 97, pp. 013106-3, 07/05/ 2010.

[70]   J. Lu, H. Zhang, W. Shi, Z. Wang, Y. Zheng, T. Zhang*, et al.*, "Graphene Magnetoresistance Device in van der Pauw Geometry," *Nano Letters,* vol. 11, pp. 2973-2977, 2011/07/13 2011.

[71]   S. Pisana, P. M. Braganca, E. E. Marinero, and B. A. Gurney, "Tunable Nanoscale Graphene Magnetometers," *Nano Letters,* vol. 10, pp. 341-346, 2010/01/13 2009.

[72]   Y. Kawano, Y. Hisanaga, H. Takenouchi, and S. Komiyama, "Highly sensitive and tunable detection of far-infrared radiation by quantum Hall devices," *Journal of Applied Physics,* vol. 89, pp. 4037-4048, 2001.

[73]   J. S. Bunch, S. S. Verbridge, J. S. Alden, A. M. van der Zande, J. M. Parpia, H. G. Craighead*, et al.*, "Impermeable atomic membranes from graphene sheets," *Nano letters,* vol. 8, pp. 2458-2462, 2008.

[74]   C. Jiang, S. Markutsya, Y. Pikus, and V. V. Tsukruk, "Freely suspended nanocomposite membranes as highly sensitive sensors," *Nature materials,* vol. 3, pp. 721-728, 2004.

[75]   K. E. Mueggenburg, X.-M. Lin, R. H. Goldsmith, and H. M. Jaeger, "Elastic membranes of close-packed nanoparticle arrays," *Nature materials,* vol. 6, pp. 656-660, 2007.

[76]   G. Boero, M. Demierre, P. A. Besse, and R. S. Popovic, "Micro-Hall devices: performance, technologies and applications," *Sensors and Actuators A: Physical,* vol. 106, pp. 314-320, 9/15/ 2003.

[77]   A. Candini, S. Klyatskaya, M. Ruben, W. Wernsdorfer, and M. Affronte, "Graphene Spintronic Devices with Molecular Nanomagnets," *Nano Letters,* vol. 11, pp. 2634-2639, 2011/07/13 2011.

[78]   M. Huang, T. A. Pascal, H. Kim, W. A. Goddard, and J. R. Greer, "Electronic−Mechanical Coupling in Graphene from in situ Nanoindentation Experiments and Multiscale Atomistic Simulations," *Nano Letters,* vol. 11, pp. 1241-1246, 2011/03/09 2011.

[79]   Y. Lee, S. Bae, H. Jang, S. Jang, S.-E. Zhu, S. H. Sim, *et al.*, "Wafer-Scale Synthesis and Transfer of Graphene Films," *Nano Letters,* vol. 10, pp. 490-493, 2010/02/10 2010.

[80]   S.-E. Zhu, M. Krishna Ghatkesar, C. Zhang, and G. Janssen, "Graphene based piezoresistive pressure sensor," *Applied Physics Letters,* vol. 102, pp. 161904-161904-3, 2013.

[81]   S.-E. Zhu, R. Shabani, J. Rho, Y. Kim, B. H. Hong, J.-H. Ahn, *et al.*, "Graphene-based bimorph microactuators," *Nano letters,* vol. 11, pp. 977-981, 2011.

[82]   Y. Xu, Z. Guo, H. Chen, Y. Yuan, J. Lou, X. Lin, *et al.*, "In-plane and tunneling pressure sensors based on graphene/hexagonal boron nitride heterostructures," *Applied Physics Letters,* vol. 99, pp. 133109-133109-3, 2011.

[83]   L.-J. Wang, G. Cao, T. Tu, H.-O. Li, C. Zhou, X.-J. Hao, *et al.*, "A graphene quantum dot with a single electron transistor as an integrated charge sensor," *Applied Physics Letters,* vol. 97, pp. 262113-262113-3, 2010.

[84]   M. Funaro, M. Sarno, P. Ciambelli, C. Altavilla, and A. Proto, "Real time radiation dosimeters based on vertically aligned multiwall carbon nanotubes and graphene," *Nanotechnology,* vol. 24, p. 075704, 2013.

[85]   M. W. Nomani, R. Shishir, M. Qazi, D. Diwan, V. Shields, M. Spencer, *et al.*, "Highly sensitive and selective detection of NO< sub> 2</sub> using epitaxial graphene on 6H-SiC," *Sensors and Actuators B: Chemical,* vol. 150, pp. 301-307, 2010.

[86]   M. W. Nomani, V. Shields, G. Tompa, N. Sbrockey, M. Spencer, R. Webb, *et al.*, "Correlated conductivity and work function changes in epitaxial graphene," *Applied Physics Letters,* vol. 100, pp. 092113-092113-4, 2012.

[87]   R. A. Potyrailo, C. Surman, N. Nagraj, and A. Burns, "Materials and transducers toward selective wireless gas sensing," *Chemical reviews,* vol. 111, pp. 7315-7354, 2011.

[88]   S. Rumyantsev, G. Liu, M. S. Shur, R. A. Potyrailo, and A. A. Balandin, "Selective Gas Sensing with a Single Pristine Graphene Transistor," *Nano Letters,* vol. 12, pp. 2294-2298, 2012/05/09 2012.

[89]   M. W. K. Nomani, D. Kersey, J. James, D. Diwan, T. Vogt, R. A. Webb, *et al.*, "Highly sensitive and multidimensional detection of NO2 using In2O3 thin films," *Sensors and Actuators B: Chemical,* vol. 160, pp. 251-259, 12/15/ 2011.

[90]   W. Hong, H. Bai, Y. Xu, Z. Yao, Z. Gu, and G. Shi, "Preparation of Gold Nanoparticle/Graphene Composites with Controlled Weight Contents and Their Application in Biosensors," *The Journal of Physical Chemistry C,* vol. 114, pp. 1822-1826, 2010/02/04 2010.

[91]   P. K. Ang, W. Chen, A. T. S. Wee, and K. P. Loh, "Solution-gated epitaxial graphene as pH sensor," *Journal of the American Chemical Society,* vol. 130, pp. 14392-14393, 2008.

[92]   T. Zhang, Z. Cheng, Y. Wang, Z. Li, C. Wang, Y. Li, *et al.*, "Self-assembled 1-octadecanethiol monolayers on graphene for mercury detection," *Nano letters,* vol. 10, pp. 4738-4741, 2010.

[93]   H. Xu, H. Dai, and G. Chen, "Direct electrochemistry and electrocatalysis of hemoglobin protein entrapped in graphene and chitosan composite film," *Talanta,* vol. 81, pp. 334-338, 2010.

[94]   X. Kang, J. Wang, H. Wu, I. A. Aksay, J. Liu, and Y. Lin, "Glucose oxidase–graphene–chitosan modified electrode for direct electrochemistry and glucose sensing," *Biosensors and Bioelectronics,* vol. 25, pp. 901-905, 2009.

[95]   K.-J. Huang, D.-J. Niu, J.-Y. Sun, C.-H. Han, Z.-W. Wu, Y.-L. Li, *et al.*, "Novel electrochemical sensor based on functionalized graphene for simultaneous determination of adenine and guanine in DNA," *Colloids and Surfaces B: Biointerfaces,* vol. 82, pp. 543-549, 2011.

[96]   M. Yang, A. Javadi, H. Li, and S. Gong, "Ultrasensitive immunosensor for the detection of cancer biomarker based on graphene sheet," *Biosensors and Bioelectronics,* vol. 26, pp. 560-565, 2010.

[97]   L. Wang, K. Kalyanasundaram, M. Stanacevic, and P. Gouma, "Nanosensor device for breath acetone detection," *Sensor Letters,* vol. 8, pp. 709-712, 2010.

[98]   M. L. Simenhoff, J. F. Burke, J. J. Saukkonen, A. T. Ordinario, R. Doty, and S. Dunn, "Biochemical profile of uremic breath," *New England Journal of Medicine,* vol. 297, pp. 132-135, 1977.

[99]   R. Arsat, M. Breedon, M. Shafiei, P. Spizziri, S. Gilje, R. Kaner*, et al.*, "Graphene-like nano-sheets for surface acoustic wave gas sensor applications," *Chemical Physics Letters,* vol. 467, pp. 344-347, 2009.

[100]   A. K. Singh, M. A. Uddin, J. T. Tolson, H. Maire-Afeli, N. Sbrockey, G. S. Tompa*, et al.*, "Electrically tunable molecular doping of graphene," *Applied Physics Letters,* vol. 102, pp. 043101-5, 01/28/ 2013.

[101]   O. Leenaerts, B. Partoens, and F. Peeters, "Adsorption of H 2 O, N H 3, CO, N O 2, and NO on graphene: A first-principles study," *Physical Review B,* vol. 77, p. 125416, 2008.

[102]   K. K. Kolasinski, *Surface science: foundations of catalysis and nanoscience*: John Wiley & Sons, 2012.

[103]   C. R. Arumainayagam and R. J. Madix, "Molecular beam studies of gas-surface collision dynamics," *Progress in Surface science,* vol. 38, pp. 1-102, 1991.

[104]   A. N. Pal, A. A. Bol, and A. Ghosh, "Large low-frequency resistance noise in chemical vapor deposited graphene," *Applied Physics Letters,* vol. 97, p. 133504, 2010.

[105]   T. Oznuluer, E. Pince, E. O. Polat, O. Balci, O. Salihoglu, and C. Kocabas, "Synthesis of graphene on gold," *Applied Physics Letters,* vol. 98, p. 183101, 2011.

[106]   A. Pirkle, J. Chan, A. Venugopal, D. Hinojos, C. Magnuson, S. McDonnell*, et al.*, "The effect of chemical residues on the physical and electrical properties of chemical vapor deposited graphene transferred to SiO2," *Applied Physics Letters,* vol. 99, p. 122108, 2011.

[107]   T. O. Wehling, K. S. Novoselov, S. V. Morozov, E. E. Vdovin, M. I. Katsnelson, A. K. Geim*, et al.*, "Molecular Doping of Graphene," *Nano Letters,* vol. 8, pp. 173-177, 2008/01/01 2007.

[108]   Z. Chen, I. Santoso, R. Wang, L. F. Xie, H. Ying Mao, H. Huang*, et al.*, "Surface transfer hole doping of epitaxial graphene using MoO 3 thin film," *Applied Physics Letters,* vol. 96, pp. 213104-213104-3, 2010.

[109]   T. Wehling, K. Novoselov, S. Morozov, E. Vdovin, M. Katsnelson, A. Geim*, et al.*, "Molecular doping of graphene," *Nano letters,* vol. 8, pp. 173-177, 2008.

[110]   A. Krasheninnikov and F. Banhart, "Engineering of nanostructured carbon materials with electron or ion beams," *Nature materials,* vol. 6, pp. 723-733, 2007.

[111]   F. Banhart, J. Kotakoski, and A. V. Krasheninnikov, "Structural defects in graphene," *ACS nano,* vol. 5, pp. 26-41, 2010.

[112]   Z. Yong-Hui, C. Ya-Bin, Z. Kai-Ge, L. Cai-Hong, Z. Jing, Z. Hao-Li*, et al.*, "Improving gas sensing properties of graphene by introducing dopants and defects: a first-principles study," *Nanotechnology,* vol. 20, p. 185504, 2009.

[113]   S.-Z. Liang, G. Chen, A. R. Harutyunyan, M. W. Cole, and J. O. Sofo, "Analysis and optimization of carbon nanotubes and graphene sensors based on adsorption-desorption kinetics," *Applied Physics Letters,* vol. 103, p. 233108, 2013.

[114]   S. M. Sze and K. K. Ng, *Physics of semiconductor devices*: John Wiley & Sons, 2006.

[115]   J. Chan, A. Venugopal, A. Pirkle, S. McDonnell, D. Hinojos, C. W. Magnuson*, et al.*, "Reducing extrinsic performance-limiting factors in graphene grown by chemical vapor deposition," *ACS nano,* vol. 6, pp. 3224-3229, 2012.

[116] J. W. Suk, A. Kitt, C. W. Magnuson, Y. Hao, S. Ahmed, J. An, *et al.*, "Transfer of CVD-grown monolayer graphene onto arbitrary substrates," *ACS nano,* vol. 5, pp. 6916-6924, 2011.

[117] C.-C. Chen, M. Aykol, C.-C. Chang, A. Levi, and S. B. Cronin, "Graphene-silicon Schottky diodes," *Nano letters,* vol. 11, pp. 1863-1867, 2011.

[118] R. T. Tung, "Recent advances in Schottky barrier concepts," *Materials Science and Engineering: R: Reports,* vol. 35, pp. 1-138, 2001.

[119] S. Tongay, M. Lemaitre, X. Miao, B. Gila, B. Appleton, and A. Hebard, "Rectification at graphene-semiconductor interfaces: zero-gap semiconductor-based diodes," *Physical Review X,* vol. 2, p. 011002, 2012.

[120] U. K. Mishra and J. Singh, *Semiconductor device physics and design* vol. 189: Springer, 2008.

[121] X. Li, H. Zhu, K. Wang, A. Cao, J. Wei, C. Li, *et al.*, "Graphene-On-Silicon Schottky Junction Solar Cells," *Advanced Materials,* vol. 22, pp. 2743-2748, 2010.

[122] S. Shivaraman, L. H. Herman, F. Rana, J. Park, and M. G. Spencer, "Schottky barrier inhomogeneities at the interface of few layer epitaxial graphene and silicon carbide," *Applied Physics Letters,* vol. 100, p. 183112, 2012.

[123] R. S. Muller, T. I. Kamins, M. Chan, and P. K. Ko, "Device electronics for integrated circuits," 1986.

[124] S. Tongay, T. Schumann, X. Miao, B. Appleton, and A. Hebard, "Tuning Schottky diodes at the many-layer-graphene/semiconductor interface by doping," *Carbon,* vol. 49, pp. 2033-2038, 2011.

[125] A. Singh, M. Uddin, T. Sudarshan, and G. Koley, "Tunable Reverse-Biased Graphene/Silicon Heterojunction Schottky Diode Sensor," *Small,* vol. 10, pp. 1555-1565, 2014.

[126] W. Wu, Z. Liu, L. A. Jauregui, Q. Yu, R. Pillai, H. Cao, *et al.*, "Wafer-scale synthesis of graphene by chemical vapor deposition and its application in hydrogen sensing," *Sensors and Actuators B: Chemical,* vol. 150, pp. 296-300, 2010.

[127] B. H. Chu, C. Lo, J. Nicolosi, C. Chang, V. Chen, W. Strupinski, *et al.*, "Hydrogen detection using platinum coated graphene grown on SiC," *Sensors and Actuators B: Chemical,* vol. 157, pp. 500-503, 2011.

[128] J. L. Johnson, A. Behnam, S. Pearton, and A. Ural, "Hydrogen Sensing Using Pd-Functionalized Multi-Layer Graphene Nanoribbon Networks," *Advanced Materials,* vol. 22, pp. 4877-4880, 2010.

[129] T. Wehling, S. Yuan, A. Lichtenstein, A. Geim, and M. Katsnelson, "Resonant scattering by realistic impurities in graphene," *Physical review letters,* vol. 105, p. 056802, 2010.

[130] S. Sarkar, H. Zhang, J. W. Huang, F. Wang, E. Bekyarova, C. N. Lau, *et al.*, "Organometallic hexahapto functionalization of single layer graphene as a route to high mobility graphene devices," *Advanced Materials,* vol. 25, pp. 1131-1136, 2013.

[131] H. Zhang, E. Bekyarova, J.-W. Huang, Z. Zhao, W. Bao, F. Wang, *et al.*, "Aryl functionalization as a route to band gap engineering in single layer graphene devices," *Nano letters,* vol. 11, pp. 4047-4051, 2011.

[132] E. Glueckauf and G. Kitt, "The hydrogen content of atmospheric air at ground level," *Quarterly Journal of the Royal Meteorological Society,* vol. 83, pp. 522-528, 1957.

[133] H.-Y. Kim, K. Lee, N. McEvoy, C. Yim, and G. S. Duesberg, "Chemically Modulated Graphene Diodes," *Nano letters,* vol. 13, pp. 2182-2188, 2013.

[134] Y. Ren, S. Chen, W. Cai, Y. Zhu, C. Zhu, and R. S. Ruoff, "Controlling the electrical transport properties of graphene by in situ metal deposition," *Applied Physics Letters,* vol. 97, p. 053107, 2010.

[135] H. B. Michaelson, "The work function of the elements and its periodicity," *Journal of Applied Physics,* vol. 48, pp. 4729-4733, 1977.

[136] G. Giovannetti, P. Khomyakov, G. Brocks, V. Karpan, J. Van den Brink, and P. Kelly, "Doping graphene with metal contacts," *Physical Review Letters,* vol. 101, p. 026803, 2008.

[137] M. G. Chung, D.-H. Kim, D. K. Seo, T. Kim, H. U. Im, H. M. Lee*, et al.*, "Flexible hydrogen sensors using graphene with palladium nanoparticle decoration," *Sensors and Actuators B: Chemical,* vol. 169, pp. 387-392, 2012.

[138] K. Skucha, Z. Fan, K. Jeon, A. Javey, and B. Boser, "Palladium/silicon nanowire Schottky barrier-based hydrogen sensors," *Sensors and Actuators B: Chemical,* vol. 145, pp. 232-238, 2010.

[139] Y.-I. Chou, C.-M. Chen, W.-C. Liu, and H.-I. Chen, "A new Pd-InP Schottky hydrogen sensor fabricated by electrophoretic deposition with Pd nanoparticles," *Electron Device Letters, IEEE,* vol. 26, pp. 62-65, 2005.

[140] Y. An, A. Behnam, E. Pop, and A. Ural, "Metal-semiconductor-metal photodetectors based on graphene/p-type silicon Schottky junctions," *Applied Physics Letters,* vol. 102, p. 013110, 2013.

[141] I. Lundström and D. Söderberg, "Hydrogen sensitive mos-structures part 2: characterization," *Sensors and Actuators,* vol. 2, pp. 105-138, 1982.

[142] B. H. Chu, J. Nicolosi, C. Lo, W. Strupinski, S. Pearton, and F. Ren, "Effect of coated platinum thickness on hydrogen detection sensitivity of graphene-based sensors," *Electrochemical and Solid-State Letters,* vol. 14, pp. K43-K45, 2011.

[143] M. A. Uddin, A. K. Singh, T. S. Sudarshan, and G. Koley, "Functionalized graphene/silicon chemi-diode H2 sensor with tunable sensitivity," *Nanotechnology,* vol. 25, p. 125501, 2014.

[144] M. Hudait and S. Krupanidhi, "Doping dependence of the barrier height and ideality factor of Au/n-GaAs Schottky diodes at low temperatures," *Physica B: Condensed Matter,* vol. 307, pp. 125-137, 2001.